Sub-millimetre observations of periodic methanol maser sources

J Morgan

orcid.org 0000-0002-9486-7689

Dissertation submitted in fulfilment of the requirements for the degree *Master of Science in Astrophysical Sciences* at the North-West University

Supervisor:	Prof DJ Van der Walt
Co-supervisor:	Prof JO Chibueze

Graduation July 2019

23451149

I dedicate this dissertation to my Heavenly Father.

∼ Ephesians 2:8-9 ∼

"[8]*For you have been delivered by grace through trusting, and even this is not your accomplishment but God's gift.* [9]*You were not delivered by your own actions; therefore no one should boast. "*

Acknowledgements

I would like to express my deepest appreciation to the people that made the completion of this study possible.

- My supervisor Prof Johan van der Walt for his exceptional support.
- My co-supervisor Prof James Chibueze for his guidance.
- To Ruby van Rooyen for the skills she taught me regarding the data calibration and imaging and for all her support.
- The personnel at the Physics Department for their assistance.
- The Center for Space Research at the North-West University for the financial support.
- My profound gratitude to my mother, Maria, and my brother, JD, as well as to the rest of my family for all their love and support.
- My husband Lee-Roy for his love, support and continuous encouragement throughout my years of study and through the process of researching and writing of this dissertation.

Declaration of Authorship

I, Morgan Jean-Marié, declare that this thesis titled, SUB-MILLIMETRE OBSERVATIONS OF PERIODIC METHANOL MASERS and the work presented in it are my own. I confirm that:

- This work was done wholly or mainly while in candidature for a research degree at this University.
- Where any part of this thesis has previously been submitted for a degree or any other qualification at this University or any other institution, this has been clearly stated.
- Where I have consulted the published work of others, this is always clearly attributed.
- Where I have quoted from the work of others, the source is always given. With the exception of such quotations, this thesis is entirely my work.
- I have acknowledged all main sources of help I do.
- Where the thesis is based on work done by myself jointly with others, I have made clear exactly what was done by others and what I have contributed myself.

Signed: _____

Date: _____

NORTH-WEST UNIVERSITY, POTCHEFSTROOM-CAMPUS

Abstract

Faculty of Natural Sciences
Department of Physics

Master of Science in Astrophysical Sciences

Sub-millimetre observations of periodic methanol maser sources

by J MORGAN

One of the properties of high-mass star forming regions is that they are associated with masers. A small group of these star forming regions contain periodic methanol masers. A significant aspect of the periodic methanol masers are their variety of light curves. Two types of periodic maser light curves are well defined, namely, masers that have a light curve with a sharp rise in the maser flux density, reaching a peak, followed by a slow decay and masers that have a light curve of which the profile resembles an absolute cosine function. These differences in the light curve shapes could point to different mechanisms responsible for the periodic variability.

This study uses sub-millimetre observations of these regions, associated with periodic methanol masers with different types of light curves, to search for differences or similarities in these regions.

The Sub-Millimetre Array observations of G22.357+0.066 and G25.411+0.105 and the Atacama Large Millimetre/Sub- Millimetre Array observations of G9.62+0.20E reveal clear geometric differences between the sources. All three sources are associated with outflows. G22.357+0.066 and G9.62+0.19E have bipolar outflows almost in the plane of the sky and G25.411+0.105 has a bipolar outflow almost perpendicular to the plane of the sky. Since outflows are present in the sources it implies that they should also have disks, meaning that the disks of G22.357+0.066 and G9.62+0.19E would have similar orientations and the disk of G25.411+0.105 would have a different orientation. Thus, this suggests that the difference in the shape of the periodic methanol maser light curves might be a viewing angle effect.

Keywords: masers - stars: formation - ISM: clouds - Radio lines: ISM - sub-millimetre: ISM - techniques: interferometric - sources: G9.62+0.20E - G22.357+0.066 - G25.411+0.105

Opsomming

Een van die eienskappe van hoë-massa stervorming gebiede is dat dit met masers geassosieer word. 'n Klein groep van hierdie stervorming gebiede bevat periodiese metanol masers. 'n Belangrike aspek van periodiese metanol masers is hul verskeidenheid van ligkrommes. Twee tipes periodiese maser ligkrommes is goed gedefinieer, masers wat 'n lig kromme het wat 'n skerp styging in die maser vloeddigtheid het, 'n piek bereik en gevolg word deur 'n stadige verval en masers met 'n ligkromme waarvan die profiel lyk soos 'n absolute kosinusfunksie. Hierdie verskeidenheid van ligkrommes dui daarop dat daar heel moontlik verskillende meganismes is wat die periodiese veranderlikheid veroorsaak.

Hierdie studie gebruik submillimeter waarnemings van hierdie gebiede, wat geassosieer word met periodiese metanol masers met verskillende tipes ligkrommes, om na die verskille en ooreen komste in hierdie gebiede te soek.

Die SMA waarnemings van G22.357+0.066 en G25.411+0.105 en die ALMA waarnemings van G9.62+0.19E dui op duidelike geometriese verskille tussen die bronne. Al drie die bronne word geassosieer met gas wat uitvloei. G22.357+0.066 en G9.62+0.019E het bipolêre gas-uitvloei wat byna in die lug vlak is en G25.411 + 0.105 het 'n bipolêre gas-uitvloei wat amper loodreg is op die vlak van die lug. Aangesien die uitvloei van gas in die bronne teenwoordig is, impliseer dit dat hulle ook skywe moet hê. Dit beteken dat die skywe van G22.357+0.066 en G9.62+0.19E dieselfde oriëntasie sal hê en die skyf van G25.411+0.105 'n ander oriëntasie sal hê. Dus stel dit voor dat die verskil in die vorm van die periodiese metanol maser ligkromme 'n observasie-hoek effek kan wees.

Sleutelwoorde: masers - sterre: vorming - ISM: wolke - Radio lyne: ISM - submillimeter: ISM - tegnieke: interferometries - bronne: G9.62+0.20E - G22.357+0.066 - G25.411+0.105

Contents

List of Figures

List of Tables

Abbreviations

ALMA	Atacama Large Millimetre/Sub- Millimetre Array
ATLASGAL	APEX Telescope Large Area Survey of the GaLaxy
CWB	Colliding Wind Binary
d	days
FT	Fourier Transform
GMC	Giant Molecular Clouds
H II	Ionised hydrogen
IMF	Initial Mass Function
IRAM	Institute for Radio Astronomy in the Millimetre range
JCMT	James Clerk Maxwell Telescope
LBV	Luminous Blue Variable
LTE	Local Thermodynamic Equilibrium
MMB	Methanol Multi-Beam
PSF	Point Spread Function
rms	root-mean-square
SMA	Sub- Millimetre Array
UCH II	Ultra Compacted H II
UKIDSS	UKIRT Infrared Deep Sky Survey
VLA	Very Large Array
VLBA	Very Long Baseline Array
VLBI	Very-Long Baseline Interferometry
YMSOs	Young Massive Stellar Objects
yr	year
YSOs	Young Stellar Objects

Physical Constants

Constants	Symbol		Value (units)
Speed of light	c	$=$	$2.99792458 \times 10^{10}\ \mathrm{cm\,s^{-1}}$
Planck constant	h	$=$	$6.6260755(40) \times 10^{-27}\ \mathrm{erg\,s^{-1}}$
Gravitational constant	G	$=$	$6.67259(85) \times 10^{-8}\ \mathrm{cm^3\,g^{-1}\,s^{-2}}$
Electron charge	e	$=$	$4.8032068(14) \times 10^{-10}\ \mathrm{esu}$
Mass of electron	m_e	$=$	$9.1093897(54) \times 10^{-28}\ \mathrm{g}$
Mass of proton	m_p	$=$	$1.6726231(10) \times 10^{-24}\mathrm{g}$
Mass of neutron	m_n	$=$	$1.6749286(10) \times 10^{-24}\ \mathrm{g}$
Mass of hydrogen	m_H	$=$	$1.6733 \times 10^{-24}\ \mathrm{g}$
Atomic mass unit	amu	$=$	$1.6605402(10) \times 10^{-24}\ \mathrm{g}$
Boltzmann constant	k_B	$=$	$1.380658(12) \times 10^{-16}\ \mathrm{erg\,K^{-1}}$
Stefan-Boltzmann constant	σ	$=$	$5.67051(19) \times 10^{-5}\ \mathrm{erg\,cm^{-2}\,K^{-4}\,s^{-1}}$
Rydberg constant	R_∞	$=$	$1.0974 \times 10^{5}\ \mathrm{cm^{-3}}$

Physical Constants

NAME	SYMBOL	NUMBER IN CGS UNITS
Astronomical unit	AU	1.496×10^{13} cm
Kilo-parsec	kpc	3.086×10^{21} cm
Solar mass	$M_\odot$	1.99×10^{33} g
Solar radius	$R_\odot$	6.96×10^{10} cm

Chapter 1

INTRODUCTION

1.1 General introduction

Stars are the building blocks of the Universe and without stars the Universe would have consisted only of primordial H and He. They provide the necessary elements for life in the Universe. Since stellar evolution is the primary tracer for chemical evolution (Lada, 2005), the formation and evolution of stars are fundamental to understand the evolution of all stellar systems in the Universe. In the field of observational astronomy, substantial progress is currently being made in characterizing star formation on all scales and also in determining the properties of the medium in which stars form (McKee & Ostriker, 2007). Still several unanswered questions remain as to how stars are formed and how they evolve.

Even though high-mass stars are very luminous (Lada, 2005), only a small fraction of the stars in the Univere are massive. In addition, the actual physical and chemical formation processes of high-mass stars are still poorly understood (McKee & Ostriker, 2007). Young massive stellar objects (YMSOs) are deeply embedded in giant molecular clouds (GMC). This makes optical detection of high-mass protostars, through the intervening material, difficult (McKee & Ostriker, 2007). YMSOs are usually found in Galactic spiral arms such as the Local/Orion arm, in which our solar system is located, and the Perseus arm, which is located at a distance of 2 kpc from us. Since the high-mass star formation process takes place deeply embedded within gas and dust clouds, observing it at near-infrared wavelengths is difficult because these regions are opaque. Longer wavelengths, such as millimetre and sub-millimetre wavelengths, are required to observe these high-mass star forming regions. Using millimetre and sub-millimetre wavelengths require telescopes with high angular resolution. Thus interferometers, such as the Very Long Baseline Array (VLBA), Atacama Large Millimetre/Sub- Millimetre Array (ALMA), Sub- Millimetre Array (SMA) and Very Large Array (VLA), are suitable for the study of these regions.

The formation process time-scales of high-mass star formation are short $\sim 10^5$ yr (McKee & Ostriker, 2007) and it is obscured. This makes it difficult to explore early stages of high-mass star formation. Maser emission is a helpful tool for studying high-mass star forming regions. Class II methanol masers trace early stages of high-mass star formation (Ellingsen, 2006). Since the discovery of the strong, 5_1-6_0 A^+ transition, methanol line at 6.7 GHz by Menten (1991), more than 800 methanol masers have been detected (Green et al., 2009). The high intensities of these masers enable them to be easily monitored (Goedhart et al., 2014). Methanol masers

are sensitive to changes in their environment, thus monitoring their flux densities and interpreting their light curves, could lead to new insights into high-mass star forming regions (Goedhart et al., 2014). The variability of methanol masers was first noted by Caswell et al. (1995) and G9.62+0.19E was the first confirmed periodic methanol maser (Goedhart et al., 2003).

1.2 Motivation and problem statement

One of the most fascinating properties of a small group, more than 20, high-mass star forming regions is the periodic flaring behaviour of the associated class II methanol masers. A significant aspect of the set of periodic masers is their light curves which have quite a variety of shapes.

In order to obtain a better understanding of high-mass star forming regions associated with periodic methanol masers, an observational study should be conducted on a few of these regions. The main motivation behind this study is to compare these regions and see if there are any physical differences found that might explain the variations in the shape of light curves detected from periodic methanol masers.

Inspection of the different shapes of light curves led Maswanganye et al. (2015) to suggest at least two well defined categories for periodic methanol maser light curves: (i) a flare-like profile in the light curve shape that shows a fast increase followed by a slow decay that could resemble an exponential-like function. The sources that belong to this group are G9.62+0.19E (Goedhart et al., 2003), G22.357+0.066 (Szymczak et al., 2015), G328.24-0.55 and G331.13-0.24 (Goedhart et al., 2014). (ii) a periodic methanol maser for which the light curve resembles a $|cos(\omega t)|$ function and is referred to as a Bunny hop. The sources belonging to this group are G12.89+0.49 (Goedhart et al., 2009), G25.411+0.105 (Szymczak et al., 2015), G331.13-0.24 (Goedhart et al., 2014) and G358.460−0.391 (Maswanganye et al., 2015). For the Bunny hop light curve profile Goedhart et al. (2009) suggested a binary system as an explanation for the stability seen in the period.

There are several suggested mechanisms that have been proposed to explain the periodicity of methanol masers. van der Walt (2011) proposed a simple colliding wind binary (CWB) model that is consistent with the flare-like profile seen in G9.62+0.19E. Other mechanisms proposed are, the pulsational instabilities of very young accreting high-mass stars (Inayoshi et al., 2013) and very young binary systems orbiting within a circumbinary disk (Parfenov & Sobolev, 2014).

The variety of light curves suggest different mechanisms may likely be responsible for the different flare profiles observed (van der Walt et al., 2016). Although there are many different observed flare profiles, the fact that it is possible to identify at least two groups of periodic maser sources having similar light curves within each group, suggests that these sources might have the same underlying mechanism. It is therefore reasonable to argue that there might be other similarities in these high-mass star forming regions which contain periodic methanol masers that have the same light curve profiles.

This study investigates the possibility that the different mechanisms for the periodicity might also manifest in other properties of the star forming regions and not only in the maser emission. For example, for the CWB model to work an H II region must already be present, while the pulsation model of Inayoshi et al. (2013) implies that accretion onto the star is still ongoing. A

possible interpretation is that the masers with light curves, suggestive of the presence of a pulsating stars, are associated with an earlier evolutionary phase of high-mass stars in comparison to those that can be described with the CWB scenario, where an H II region is already present. The objective of this study is to determine if there are any indications in the dust and molecular line emission of periodic methanol maser sources that suggest differences or similarities in these regions.

1.3 Regions of study

As noted earlier, the aim of this study is to search for possible observational differences in the star forming environment of periodic masers with different shapes of maser light curves. In order to do this, four sources were selected, two from the CWB and two from the Bunny hop protostars. The sources were selected in such a way that it would be possible to observe them with the SMA. They are G9.62+0.19E and G22.357+0.066 from the CWBs and G25.411+0.105 and G358.460−0.391 from the Bunny hops. Unfortunately the data obtained for G358.460−0.391 was not usable due to technical problems during the observation and therefore the focus in this study would only be on the three remaining sources. G22.357+0.066 and G25.411+0.105 were observed with the SMA and ALMA archival data was used for G9.62+0.19E. G9.62+0.19E is an important periodic methanol maser source, since it was the first confirmed source and the brightest source with a light curve profile that can be explained by the CWB model. Compared to G9.62+0.19E, the regions G22.357+0.066 and G25.411+0.105 are not well documented in the literature. Table 1.1 gives the systemic velocities of the target sources.

TABLE 1.1: Systemic velocities of target sources

Object-name	V_{sys} (km s^{-1})
G9.62+0.19E	2.1 [1]
G22.357+0.066	84.2 [2]
G25.441+0.105	96.0 [2]

[1] Liu et al. (2017), [2] Szymczak et al. (2007).

1.3.1 G9.62+0.19E

G9.62+0.19E is located at a distance of 5.2 kpc (Sanna et al., 2009) and has a light curve with a flaring pattern which is presented in Figure 1.1. It was the first confirmed periodic maser (Goedhart et al., 2003). It is the brightest 6.7 GHz methanol maser known and has a period of 243 d (Goedhart et al., 2014). G9.62+0.19E exhibits simultaneous flares at 6.7 GHz and 12.2 GHz (van der Walt et al., 2009). G9.62+0.19E is also associated with an H II region. Garay et al. (1993) and Kurtz (2002) classified it as a hyper-compact H II region. This confirmed H II region associated with G9.62+0.19E makes the previously mentioned CWB model, proposed by van der Walt (2011), likely to explain the flare-like profile since the CWB is based on the periodic behaviour of G9.62+0.19E being associated with a binary system. This binary system then might affect the ionization level in parts of the background H II region (van der Walt, 2011). Goedhart et al. (2014) also found hydroxyl (OH) maser emission in G9.62+0.19E. There are also millimetre and sub-millimetre studies done on G9.62+0.19 i.e. Hofner et al. (1996) and Liu et al. (2017). Liu et al. (2017) detected hot molecular methyl cyanide (CH_3CN) lines and

strong methanol (CH_3OH) lines toward G9.62+0.19E, making it a hot core. They also reported that G9.62+0.19E does not drive molecular outflows and since G9.62+0.19E also shows strong centimetre continuum emission, it could indicated that the accretion in G9.62+0.19E has been halted (Liu et al., 2017). Liu et al. (2011) constructed a velocity field map (moment 1 map) for thioformaldehyde (H_2CS) in G9.62+0.19E and found evidence of rotational motion. They also determined a rotational temperature of 92K for H_2CS.

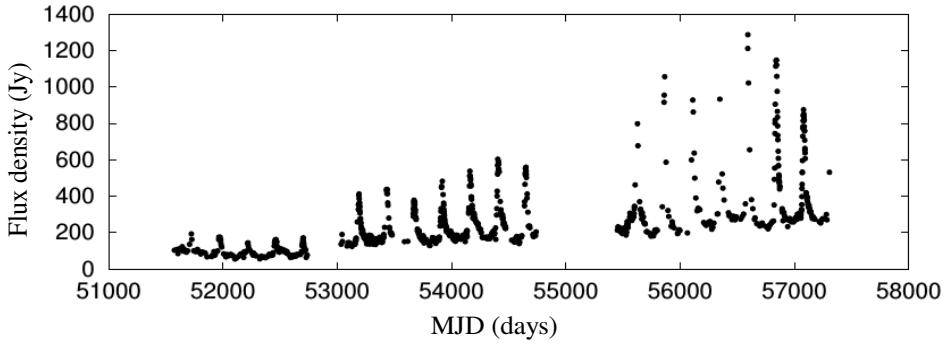

FIGURE 1.1: The light curve of G9.62+0.19E, showing a profile with a fast increase followed by a slow decrease (Goedhart et al., 2014).

1.3.2 G22.357+0.066

G22.357+0.066 is located at a distance of 4.86 kpc (Reid et al., 2009). Figure 1.2 shows the light curves of the different maser features associated with G22.357+0.066. Comparing Figure1.2 with the light curve of G9.62+0.19E a similarity is seen in the profile of the light curves in the the two sources. G22.357+0.066 has a period of 179 d (Szymczak et al., 2015). The light curve of G22.357+0.066 has seven features (Szymczak et al., 2011) at the following velocities: 78.95 km s^{-1}, 79.52 km s^{-1}, 80.09 km s^{-1}, 81.45 km s^{-1}, 83.42 km s^{-1}, 85.05 km s^{-1} and 88.47 km s^{-1}. Szymczak et al. (2011) noted that the maser emission spectrum shows that the blue-shifted emission, the velocities smaller than the systemic velocity, is significantly more variable than the red-shifted emission. They also constructed a 3D structure of G22.357+0.066 and proposed that the maser emission might originate in a circumstellar disk or torus.

1.3.3 G25.411+0.105

G25.411+0.105 has a Bunny hop light curve profile, as presented in Figure 1.3, and has a period of 245 d (Szymczak et al., 2015). It is located at a distance of 9.50 kpc (Szymczak et al., 2007). Bartkiewicz et al. (2009) found that G25.411+0.105 has a ring-like distribution of maser spots. They calculated that the ring has a major axis of 1960 AU. Bartkiewicz et al. (2011) also found no water (H_2O) emission above the 5σ level of 15 mJy to 25 mJy, but they noted that Very-Long-Baseline Interferometry (VLBI) observations are needed for confirmation.

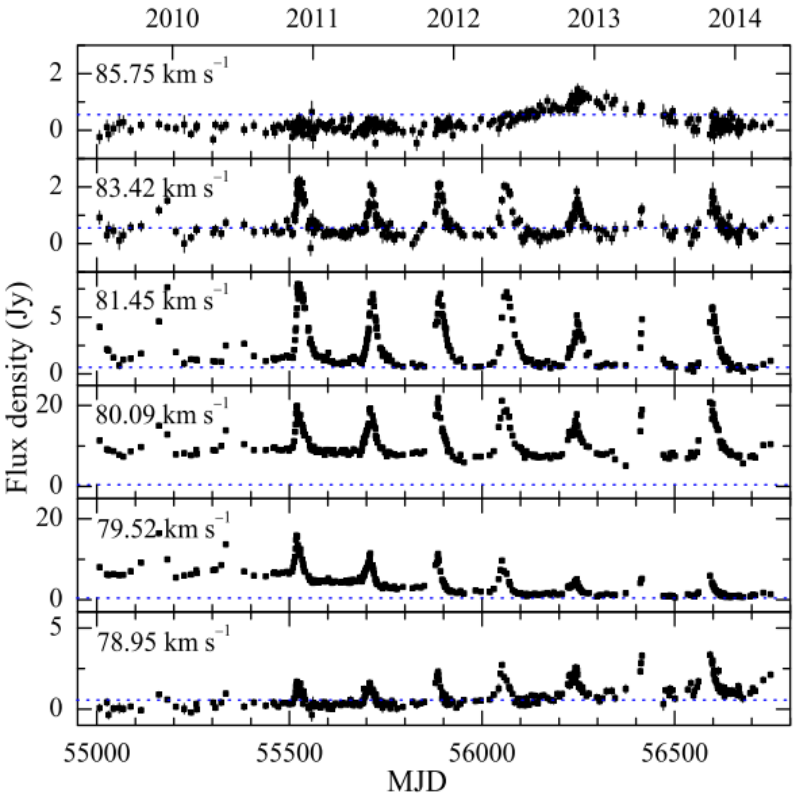

FIGURE 1.2: The light curve of G22.357+0.066, showing a profile with a fast increase followed by a slow decrease that is similar to the profile of G9.62+0.19E (Szymczak et al., 2015).

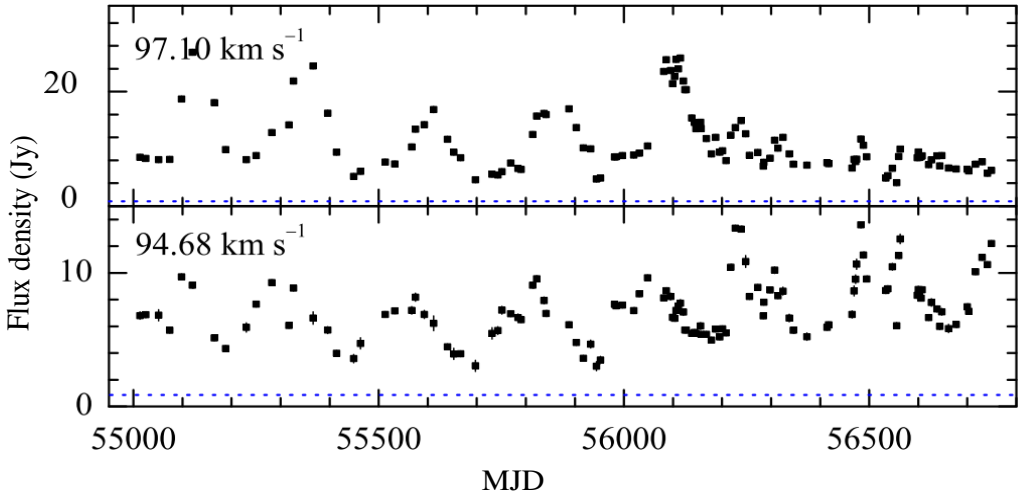

FIGURE 1.3: The light curve of G25.411+0.105, showing a profile that resembles a $|cos(\omega t)|$ function (Bunny hop)) (Szymczak et al., 2015).

1.4 Chapters to follow

This section contains a short summary of the contents of the chapters to follow:

Chapter 2 : Theoretical background

Chapter 2 presents background on the processes of massive star formation, starting with the properties of GMCs. Dynamic processes of formation of massive protostars, like bipolar outflows and keplerian disks are described. This chapter also contains an overview on radiative transfer. The CO and CH_3OH molecules are also discussed in this chapter since their line emission are the focus in this study. The last part of the chapter is a brief background of masers.

Chapter 3 : Interferometry and observations

This chapter explains the important concepts of radio interferometry and contains the details of the SMA and ALMA observations.

Chapter 4 : Results and discussion

The results of the observations are presented in this chapter as well as the analyses and discussion of the results.

Chapter 5 : Summary and conclusions

An overall summary as well as the conclusions made from the data analysis and recommendations for future work are presented in this chapter.

Chapter 2

THEORETICAL BACKGROUND

2.1 Introduction

In preparation for the analysis presented in later chapters some introduction of the study of masers in high-mass star forming regions is necessary. A broad spectrum of background knowledge is needed, however to discuss each topic in detail is beyond the scope of the study therefore this chapter presents a general background needed for conceptual understanding of the analyses presented. It includes discussion about the medium in which star formation takes place as well as the conditions required inside the medium for star formation to occur. Since the analysis focus on thermal CO and methanol emission as well as non-thermal methanol maser emission, some background knowledge of radiative transfer and methanol maser periodicity are also included.

2.2 Star formation

2.2.1 Molecular clouds

All star formation occurs in molecular clouds. In order to understand the star forming process basic knowledge of the properties of molecular clouds is needed. These clouds provide the initial conditions necessary for star formation to take place (Blitz, 1993). Molecular clouds are cold, dense condensations of molecular gas, consisting mostly of H_2 molecules, and dust (Bally, 1986), with temperatures ranging from 10 K to 50 K and densities larger than 10^3 cm^{-3} (Blitz, 1993). Molecular clouds are optically thick at short wavelengths such as near-infrared (Bally, 1986). However they do emit at longer wavelengths, such as far-infrared, millimetre and sub-millimetre wavelengths. Thus the physical parameters of molecular clouds, such as dust and gas temperature, density and mass can be studied at these long wavelengths (Kwok, 2007).

Star forming clouds have irregular boundaries (Larson, 1994) with fractal shapes (Larson, 2003). The surface of the molecular cloud resembles the surface of a medium that has a turbulent flow, thus suggesting the presence of turbulent motions within the cloud (Larson, 2003). The opacity that is needed for the survival of the cloud is due to the dust that shields the cloud from destructive ultra-violet radiation. This gives molecular clouds column densities of $\sim$ 100 to 300 particles cm^{-2} (Larson, 2003).

The formation of molecular clouds appears to be a rapid process. Elmegreen (1990) discusses three possible mechanisms for the formation of molecular clouds: (1) random collisions of smaller clouds leading to cloud growth, (2) gravitational instability, where gas is gathered gravitationally to form large cloud complexes and (3) stimulated accumulation in pressurized environments. The lifetime of a molecular cloud in which star formation takes place is determined by cloud formation, evolution and destruction, which all have approximately the same duration, making these processes inseparable in time (Larson, 1994). Thus star forming clouds are transient objects, with relatively short lifetimes of ~ 40 Myr (Elmegreen, 1990).

There are different types of molecular clouds with different densities, masses, sizes and temperatures, all leading to different rates and types of star formation. The different types of molecular clouds are summarized in Table 2.1.

TABLE 2.1: Different types of molecular clouds (Bally, 1986).

	Molecular cloud	Star formation	Mass ($M_\odot$)
(1)	Globules	Minor star formation	10
(2)	Small molecular clouds	Low-mass star formation	50
(3)	Small cloud complexes	Low to moderate -mass star formation	10^4
(4)	Giant molecular clouds	High-mass star formation	$\geq 10^5$

2.2.2 Giant molecular clouds (GMCs)

Clouds with masses $\geq 10^5 M_\odot$ and densities as high as 10^6 cm^{-3} (Lada, 2005) are classified as giant molecular clouds. GMCs are usually composed from a set of clumps (Blitz, 1993). These clumps are the precursors to stellar clusters and have masses of ~ 50 to 500 $M_\odot$. Clumps contain dense cores, which form individial stars or binaries, with masses of ~ 0.5 to 5 $M_\odot$ (Blitz, 1993). GMCs are gravitationally bound (Bally, 1986) and in galaxies with well defined spiral arms, GMCs are mostly confined to the spiral arms (Blitz & Williams, 1999).

Blitz (1990) did a study on local GMCs and concluded the following:

- GMCs are nucleation sites for almost all star formation in the Galaxy.
- GMCs are objects with well defined boundaries. These boundaries suggest a phase transition at the edges of the cloud.
- After cloud formation, star formation starts almost instantly.
- GMCs do not survive the birth of more than a few generations of massive stars.
- The formation of GMCs, with the exception of clouds with masses $\geq 10^6$ $M_\odot$, seems to be independent of the spiral-arm induced collisional process.

The formation of stars only take place in the densest regions, the cores, of GMCs (Williams et al., 2000). The conditions inside these cores define the star formation in the cloud (Bergin et al., 1997). Williams et al. (2000) defines GMCs as turbulent, magnetized, compressible fluids with gravitationally unstable cores inside. Turbulence and magnetic fields counteract gravity and hinder star formation in the cloud. The magnetic fields in massive dense cores have strengths

of $\sim$ 0.1 mG to 1.0 mG (Houde et al., 2016). In very general terms star formation involves the collapse of a cloud core under its own gravity.

Dense cores in GMCs can make up 1 % to 10 % of the total mass of the cloud, depending on how evolved the cloud is. Evolved clouds with more active star forming regions contain a higher percentage of dense core mass than young clouds with little star formation (Lada, 2005). GMCs have diameters of $\sim$ 50 pc and contain various sites for star formation (Williams et al., 2000). Active star forming regions in GMCs can be identified by the temperatures that range between 50 K and 100 K. This suggest that the cloud must have an internal heating source. These heating sources are associated with massive OB stars in their early stages of evolution (Kwok, 2007).

2.2.3 Physical conditions

Now that the natal environment of high-mass stars has been reviewed in section 2.2, the conditions leading to the formation of stars will become the focus. A more quantitative approach will be taken to find the physical conditions that lead to the collapse of molecular clouds in order to form cores , which will give rise to stars. First the Virial theorem is introduced and unless stated other wise, the derivation of the Virial theorem is taken from Stahler & Palla (2005). There is also a less complicated derivation by Tayler (1994) presented in Appendix A. The Virial theorem assesses the balance of forces within any object that is in hydrostatic equilibrium.

The equation of hydrostatic equilibrium is given by:

$$-\frac{1}{\rho_{HI}}\boldsymbol{\nabla} P_{HI} - \boldsymbol{\nabla}\Phi_g = 0 \tag{2.1}$$

where P_{HI} is the pressure of the atomic gas, ρ_{HI} the density of the atomic gas and Φ_g the gravitational potential energy. Generalizing the Hydrostatic equation to include the effect of an ambient magnetic field, yields the following:

$$\rho\frac{D\mathbf{u}}{Dt} = -\boldsymbol{\nabla} P - \rho\boldsymbol{\nabla}\Phi_g + \frac{1}{c_{motion}}\mathbf{j}\ \mathbf{x}\ \mathbf{B} \tag{2.2}$$

where **u** is the fluid velocity, with $\frac{D\mathbf{u}}{Dt}$ the convective time derivative of the fluid velocity, P is the pressure, ρ the density of the gas and c_{motion} is the velocity of the random internal motion of the medium. The last term is the magnetic force **B** per unit volume acting on a current density **j**.

If **B** and **j** are related through Ampère's law, then the Hydrostatic equation is given by:

$$\rho\frac{D\mathbf{u}}{Dt} = -\boldsymbol{\nabla} P - \rho\boldsymbol{\nabla}\Phi_g + \frac{1}{4\pi}(\boldsymbol{B}\cdot\boldsymbol{\nabla})\mathbf{B} - \frac{1}{8\pi}\boldsymbol{\nabla}|\mathbf{B}^2| \tag{2.3}$$

On the right hand side of the equation, the third term represents the tension associated with curved magnetic field lines. The last term is the gradient of a scalar magnetic pressure with magnitude $\frac{|\mathbf{B}^2|}{8\pi}$.

Equation 2.3 describes the local behaviour of the fluid. Assuming a spherical shaped molecular cloud of volume V, then to obtain the global properties, the scalar product is taken with the position vector **r** and integrated over volume. Interchanging the order of differentiation and

integration, which will not be repeated here, leads to the Virial theorem:

$$\frac{1}{2}\frac{\partial^2 I}{\partial t^2} = 2T + 2U + W + M \tag{2.4}$$

The quantity I represents the moment of inertia, T is the total kinetic energy in bulk motion, U is the energy contained in random thermal motions, W is the gravitational potential energy and M is the energy associated with the magnetic field.

For the support of giant complexes, a case where the complexes are in approximate force balance over their lifetimes can be argued. In such a case, the left hand side of Equation 2.4 is equal to zero. The Virial theorem for long term stability is then obtained:

$$2T + 2U + W + M = 0 \tag{2.5}$$

The giant molecular cloud would then be in Virial equilibrium (Stahler & Palla, 2005).

The initial conditions used, are given by Tayler (1994) in Appendix A where the total kinetic energy, T, in bulk motion and the energy, M, associated with the magnetic field, B, are not considered. Tayler (1994) only used the gravitational potential, W, and the energy contained in the random thermal motions, U. This leads to the simplest form of the Virial theorem for long term stability:

$$2U + W = 0 \tag{2.6}$$

If $2U + W > 0$, then the force due to gas pressure will dominate the gravitational potential energy ($2U > W$) and the molecular cloud will expand. The adiabatic expansion of the molecular cloud will cause the cloud to lose energy (decrease in U) and the cloud will adopt another configuration of stability (Carroll & Ostlie, 2017). If $2U + W < 0$, the molecular cloud will collapse. Since the gravitational potential energy would be to large to be supported by the thermal kinetic energy ($W > 2U$) (Stahler & Palla, 2005).

2.2.3.1 The Jeans criterion

As stated earlier, Tayler (1994) uses a less complicated version of the Virial theorem, where rotation, turbulence and magnetic fields are neglected.

$$2U + W = 0 \tag{2.7}$$

Equation 2.7 describes the physical conditions of equilibrium for GMCs. Using this the conditions for protostellar collapse can be estimated.

As noted there are two cases, $2U > W$ and $W > 2U$, that give the critical conditions for stability of a GMC. For a spherical GMC with constant density the gravitational potential energy is given by:

$$W_g \sim -\frac{3GM_r^2}{5R} \tag{2.8}$$

as derived in Appendix A (Equation A.20) (Carroll & Ostlie, 2017). M_r is the mass of the cloud and R the radius.

Using the ideal gas equation, the GMC's total thermal energy is given by:

$$U = \frac{3}{2} N k_B T \tag{2.9}$$

where N is the total number of particles and T the gas kinetic temperature. N can be written in terms of the mean molecular weight, μ, and mass, M_r (Carroll & Ostlie, 2017):

$$N = \frac{M_r}{\mu m_H} \tag{2.10}$$

Thus, the total energy in thermal motions can be written as:

$$U = \frac{3 M_r k_B T}{2 \mu m_H} \tag{2.11}$$

The conditions for gravitational collapse is given by:

$$U < |W| \tag{2.12}$$

Substituting the total thermal kinetic energy and the gravitational potential energy into Equation 2.12, gives:

$$\frac{3 M_r k_B T}{2 \mu m_H} < \frac{3 G M_r^2}{5 R} \tag{2.13}$$

The radius of the cloud in terms of mass, M_r, and density, ρ, prior to cloud collapse is:

$$R = [\frac{3 M_r}{4 \pi \rho}] \frac{1}{3} \tag{2.14}$$

Thus, Equation 2.13 becomes:

$$\frac{3 M_r k_B T}{\mu m_H} < \frac{3}{5} G M_r^2 \, [\frac{3 M_r}{4 \pi \rho}]^{-\frac{1}{3}} \tag{2.15}$$

Solving Equation 2.15 for the minimum mass of the cloud necessary for spontaneous gravitational collapse, gives the relation:

$$M_r > M_J \tag{2.16}$$

which is the Jeans criterion (Carroll & Ostlie, 2017), where M_J is the Jeans mass and is given by:

$$M_J \simeq [\frac{5 k_B T}{G \mu m_H}]^{\frac{3}{2}} \, [\frac{3}{4 \pi \rho}]^{\frac{1}{2}} \tag{2.17}$$

It is apparent that the Jeans mass depends on density and temperature. The cloud will become unstable and start collapsing when its mass exceeds the Jeans mass. Note that rotation, magnetic field and the external pressure on the cloud have been neglected.

Gravitational potential energy is released as the cloud collapses. This energy is converted to thermal energy, meaning the temperature in the cloud would rise. According to Equation 2.17 a rise in the temperature of the cloud, would increase the Jeans mass and this in turn will halt the collapse of the cloud. Thus, if it is not possible to get rid of the thermal energy in the cloud, then isothermal collapse would not take place.

2.2.3.2 Free-fall timescale

The molecular cloud is transparent to far-infrared radiation in the early stages of cloud collapse. The cloud is mainly cooled by dust, that can efficiently cool the gas, since dust grains are solids which make them thermal emitters (Kruegel, 2003). At high densities collisions between gas molecules and dust grains take place and energy is transferred from the molecules to the dust grains which will then emit long wavelength photons that can escape from the cloud, thereby cooling the cloud. The early stages of collapse are isothermal and the molecular cloud is in free-fall collapse. A complete derivation of the free-fall timescale is given in Appendix A, but an estimate of the free-fall timescale is shown here, which was taken from Carroll & Ostlie (2017).

The equation of gravitational acceleration at a distance, r, from the center of a spherical molecular cloud with a mass, M_r, is given by:

$$v\frac{dv}{dr} = -\frac{GM_r}{r^2} \tag{2.18}$$

as derived in Appendix A Equation A.22, where v is the velocity at the surface of the spherical molecular cloud.

The velocity at the surface of the cloud is given by integrating Equation 2.18 to describe the behaviour of the surface. The integral is then solved for the infall velocity as done in Appendix A Equation A.27. The infall velocity, v, is given by:

$$v = \sqrt{\frac{2GM_r}{R}}\left[\frac{R}{r} - 1\right]^{\frac{1}{2}} \tag{2.19}$$

From Appendix A, Equation 2.19 is integrated with respect to time to obtain the equation of motion for the gravitational collapse of the cloud. The equation of motion, as shown in Appendix A, is used to derive the free-fall time behaviour of a collapsing cloud:

$$t_{ff} = \sqrt{\frac{3\pi}{32G\rho}} \tag{2.20}$$

where t_{ff} is the free-fall timescale. The free-fall time is independent of the initial radius of the spherical cloud and only depends on the density, ρ. Assuming that the spherical molecular cloud has a uniform density, meaning all parts of the molecular cloud would take the same amount of time to collapse. The density within the cloud will increase at the same rate everywhere. This cloud collapse behaviour is known as a homologous collapse.

2.2.4 Cloud fragmentation

Theoretically massive star forming clouds that exceed the Jeans limit can form stars up to the initial mass of the star forming cloud. This means that the entire cloud can collapse to form a single star (Carroll & Ostlie, 2017), however observationally this is not the case.

Observations show that most stars form in clusters or in binary star systems. During the free-fall phase of collapse, the cloud density increases and the Jeans mass would decrease. Any initial inhomogeneities in the density, which may have been present within the cloud, will cause individual sections within the star forming cloud to satisfy the Jeans limit independently and to

collapse locally (Carroll & Ostlie, 2017). This is known as cloud fragmentation, a process that segments a collapsing cloud.

The simplified situation does present a challenge. The process as described in the above paragraph, implies that a large number of stars would form, however this is not the case. The process of star formation is rather inefficient, with only about 1% of cloud mass being turned into stars (Carroll & Ostlie, 2017). This means the fragmentation process must stop at some point.

The fragmentation process stops when the assumption that the cloud collapse is isothermal, breaks down. The density of the collapsing cloud fragment will increase up to a point where the gas is so opaque that not even infrared photons can escape. The energy released in the gravitational collapse process would then be trapped within the collapsing cloud, leading to a rise in temperature within. If radiation can not escape, the cloud collapse would turn from isothermal to adiabatic (Carroll & Ostlie, 2017). Cloud collapse is never totally isothermal nor adiabatic, but in reality somewhere in-between these two extremes.

2.2.5 Initial mass function (IMF)

The IMF gives the distribution of stellar masses that form in a single star forming event within a given volume of space (Kroupa, 2002). The IMF can be used in theoretical calculations to determine surface brightness, it is also used to determine chemical enrichment and the baryonic content of galaxies (Chabrier, 2003).

To determine the IMF of a stellar population consisting of stars with mixed ages is challenging, since stellar masses cannot be weighed directly using observations (Kroupa, 2002). Using the observed luminosity function or the surface brightness, makes it possible to derive an estimate for the IMF. The luminosity function is transformed into the mass function by relying on the relationships between mass, age and luminosity (Chabrier, 2003). The initial mass function only gives the distribution of stellar masses immediately after the stars are formed.

The initial mass function was originally defined by Salpeter (1955) and he estimated the IMF for stars in the solar-neighbourhood to be:

$$dN = \xi(M)d(log_{10}M)\frac{dt}{T_0} \tag{2.21}$$

where dN is the number of stars in the mass range, dM, dt is the time interval per cubic parsec in which the stars are formed and T_0 is time spent on the main sequence by bright stars. Salpeter (1955) approximated the IMF to be given by:

$$\xi(M) = 0.03\left[\frac{M}{M_0}\right]^{-2.35} \tag{2.22}$$

This simple power law is still frequently used, however other investigations into the IMF, using more extensive data, led to a power law that describes a universal IMF. Stahler & Palla (2005) used the results of one of these later studies and approximated the initial mass function as a

piecewise power law:

$$\xi(M) = \begin{cases} C_1 \left[\frac{M_*}{M_\odot}\right]^{-1.2} & 0.1 < M_*/M_\odot < 1.0 \\ C_2 \left[\frac{M_*}{M_\odot}\right]^{-2.7} & 1.0 < M_*/M_\odot < 10 \\ 0.4C_3 \left[\frac{M_*}{M_\odot}\right]^{-2.3} & 10 < M_*/M_\odot \end{cases} \tag{2.23}$$

where C is a normalization constant. Kroupa (2002) gives a more extensive sequence of power laws to approximate the IMF, which will not be shown here.

2.3 High-mass star forming regions

Young massive stellar objects are associated with protostellar disks and outflows, thus this section covers some background knowledge on keplerian disks and bipolar outflows. This section will also cover a brief overview on H II regions since they are tracers of active star formation.

2.3.1 Protostar formation

A protostar is a contracting mass of gas shielded by dust, since collapse occurs deep within the cloud (Carroll & Ostlie, 2017). Observations of a protostar will only show a small infrared source within the cloud core.

The increase in the density of a collapsing cloud fragment will make the gas opaque to infrared photons. The trapped radiation, within the central part of the core, will heat the gas within and lead to an increase in pressure. This results in the cloud core being nearly in hydrostatic equilibrium and slowing the dynamical collapse to a quasistic contraction (Carroll & Ostlie, 2017). This leads to the formation of a protostar.

The mass of a protostar is only a fraction of the mass it will have once the star reaches the Main Sequence. After the formation of the protostar the next phase is dominated by accretion onto the protostellar core. The gas continues to free-fall onto the protostar, forming an accretion disk around the protostar. These accretion disks and outflows are generally seen around very young stars (Carroll & Ostlie, 2017).

2.3.2 High-mass star formation

Unlike low-mass stars, high-mass stars are rare and located at greater distances from the Sun relative to the distances at which low-mass stars are found. High-mass stars are easily observed over large distances, because of their high luminosity (Evans, 1999). For stars with masses $\geq$ 7.0 $M_\odot$ the mass-luminosity relation is given by $L \propto M^3$ (Mihalas & Binney, 1981). The amount of fuel a star has available is determined by its mass, M, and the luminosity, L, of a star measures how rapidly the star will use its fuel supply. Therefore the lifespan of a star is proportional to the mass of fuel available divided by the luminosity. There is no firmly established evolutionary sequence on the formation of high-mass stars (Motte et al., 2017).

There are a few theories, taken from Zinnecker & Yorke (2007), that can explain the formation of massive stars. The first is monolithic collapse and disk accretion by Yorke & Sonnhalter (2002). This theory considers the collapse of an isolated massive molecular core that is non-magnetic, followed by accretion onto the core. The second theory is competitive accretion and runaway growth by Bonnell et al. (2001). This theory relies heavily on the location of the protostar and the time at which the protostar is born. For example, if a protostar is located at the center of a protostellar cluster, then it has a lager accretion domain and if a protostar is born earlier than other protostars in the cluster, then it has an advantage to end up more massive than the others. The third theory is stellar collisions and mergers which is based on the close proximity formation of massive protostars (Zinnecker & Yorke, 2007). In very dense clusters the massive stars might be packed too tightly and monolithic collapse would not be able to take place. However, for stellar collisions and mergers to take place a high density cluster of massive stars is needed. Recent observational studies, such as Ilee et al. (2018) and Hirota et al. (2017) favours the monolithic collapse and disk accretion theory.

High-mass pre-stellar cores are gravitationally bound and pre-assembled. These cores can form binaries or individual high-mass stars (Motte et al., 2017). High-mass stars in the subsequent phase are known as massive protostars and have the ability to form high-mass star binaries but not full clusters (Larson, 2003).

Rapid accreting massive protostars are considered to be precursors of ultra compact H II (UCH II) regions. Churchwell (2002a) lists five properties of these precursors to UCH II region:

- A central massive protostar serves as an internal heating source.
- Due to rapid accretion, the protostar does not produce a detectable H II region.
- Precursors of UCH II regions have short lifetimes $\sim 10^4$ yr.
- The protostar is surrounded by an equatorial accretion disk.
- Massive bipolar outflow are found along the protostar spin axis. The outflow mass, momenta and energetics are much larger than in low-mass protostars.

Massive protostars heat the gas of their surrounding envelopes and the gas will become ionized, creating an H II region. Massive young stellar objects (MYSO) that have developed an H II region are strong emitters of free-free emission in the centimetre wavelength (Motte et al., 2017).

2.3.3 Keplerian disks

Disk formation is common during the collapse of a protostellar cloud and are often observed around young stellar objects (Carroll & Ostlie, 2017). Diffuse matter caught by a MYSOs gravitational pull, does not fall into the object directly, but trough the disk it can move to the object. The diffuse matter has angular momentum which it must loose in order for it to fall further inward. Collapsing matter will spin into a centrifugally supported keplerian disk that surrounds a protostar (Carroll & Ostlie, 2017). Keplerian disks are expected to grow in size as the collapse proceeds. First the mass acquired by the forming star settles into a centrifugal supported disk. Then the matter must be transported inward through the disk, losing its angular momentum, to be accreted by the protostar (Larson, 2003). Thus for the conservation of angular momentum to hold, the angular momentum must be transported outward through the disk via a tail of matter

(Yen et al., 2017). This means that all the matter will eventually end up at the origin of the disk and the angular momentum will move outward in an infinite rotating disk.

The magnitude of the Keplerian disk depends on the mass of the protostar (Yen et al., 2017). However, it is not clear if these circumstellar disks are found surrounding all masses and evolutionary stages of MYSOs (Ilee et al., 2018). Keplerian disks are perpendicular to the outflow axis (Hirota et al., 2017).

2.3.4 Bipolar outflows

Bipolar outflows are an essential part of star formation and in many cases it is the first clear indicator of the formation of a new star (Bachiller, 1996b). They contain ionized, atomic and molecular gas that is excited (Hirota et al., 2017). Molecular outflows, originating from a central protostar, that have been observed toward massive YSOs are known to be rather common (Shepherd & Churchwell, 1996). Bipolar outflows can provide useful information, such as the underlying formation process of stars with different masses, since bipolar outflows provide a record of the mass-loss history in a system (Arce et al., 2007). These outflows also play an important role in the transfer of momentum of the protostar (Hirota et al., 2017). Bipolar outflows seen toward high-mass protostars have mass outflow rates of 10^{-5} $M_\odot$ yr^{-1} to 10^{-3} $M_\odot$ yr^{-1}, luminosities of 10^{-1} $L_\odot$ to 10^{2} $L_\odot$ and momentum rates of 10^{-4} $M_\odot$ km s^{-1} yr^{-1} to 10^{-2} $M_\odot$km s^{-1} yr^{-1} (Arce et al., 2007).

Massive YSOs undergo stages of mass loss in which outflows take part (Bachiller, 1996a). The excess of angular momentum from the contracting protostellar cloud can be carried away by outflows, limiting the mass of the in-falling protostellar cloud (Bachiller, 1996b). No generally accepted theory exists to describe how large amounts of molecular gas is accelerated and collimated on short time scales, while matter is simultaneously accreted onto the protostar (Churchwell, 2002a). Evidence have been seen of rotational outflows, driven by a magneto-centrifugal disk (Hirota et al., 2017).

Churchwell (2002a) summarized the properties of massive outflows:

- Relative to outflows in low-mass stars, massive outflows are not well collimated.
- Their velocities are a few tens of km s^{-1} and not hundreds, meaning massive outflows have large masses but low velocities.
- The outflow material is accelerated outward at large distances from the protostar, where the escape velocity and the flow velocity are of the same size.

2.3.5 P Cygni Line Profiles

Line profiles showing a mixture of absorption and emission are known as P Cygni profiles, named after the first observed Luminous Blue Variable (LBV) star that contained this type of profile. Figure 2.1 presents the classic P Cygni line profile, showing a broad intense emission line with a less intense and narrower absorption line on the blue-shifted side of the emission line (Robinson, 2007). If the spectrum of a star contains a P Cygni profile, it is evidence of the star experiencing a significant loss in mass (Carroll & Ostlie, 2017).

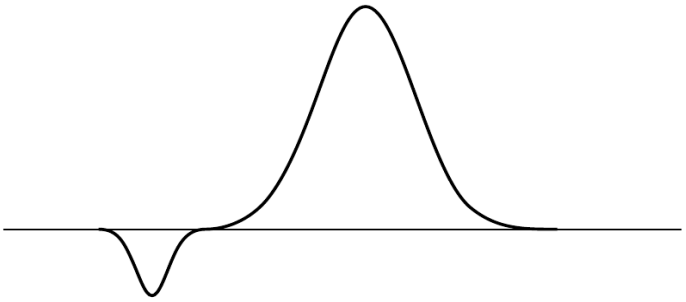

FIGURE 2.1: The classic P Cygni line profile (Robinson, 2007). This is only a representation of the P Cygni line profile.

Light passing through a cooler diffuse gas, found in the fast outflowing stellar wind, absorbs the photons emitted by the star behind the gas (Carroll & Ostlie, 2017). The absorption in the wind region leads to the observed absorption lines (Robinson, 2007). Since the cooler gas is moving toward the observer, the absorption lines are blue-shifted relative to the emission line (Carroll & Ostlie, 2017).

In some cases the P Cygni profile can go to an inverse P Cygni profile. Inverse P Cygni profiles are absorption lines on the the red-shifted side of the emission line. The red-shifted absorption indicates mass accretion rather than mass loss (Carroll & Ostlie, 2017).

2.3.6 H II regions

H II regions consist of ionized hydrogen atoms. These regions are in ionization equilibrium, the rate of ionization of the ground-state hydrogen equals the rate of recombination (Carroll & Ostlie, 2017). This means in order to form hydrogen atoms, the free electrons and protons must recombine at the same rate as the photon absorption and the ion production (Carroll & Ostlie, 2017).

Churchwell (2002b) proposed an evolutionary sequence for the formation of massive stars, based on ionization expansion. He proposed that massive protostars produce an ultra compact H II region near the end of their rapid accretion stages. From this a compact H II region is produced and then the classical H II region develops (Motte et al., 2017).

Churchwell (2002a) based his argument, that the accretion phases has ended when a H II region is detected, on the following 3 points:

- The H II region would be optically too thick to detect if accretion was occurring.
- The H II morphologies do not show evidence of an outflow bursting through the H II region.
- The outflows in massive star formation regions do not appear to be centred on the UCH II regions.

2.4 Radiative transfer

In order to understand most astronomical objects in the universe a quantitative analysis of the objects' spectrum is necessary. For this study the focus is on high-mass star forming regions and the observations are done in the radio wave range of the electromagnetic spectrum. High-mass stars have high luminosities, which means there is a large amount of energy in the radiation field. Thus to properly interpret the observations, knowledge of the generation and transport of radiation are required. The following overview on *Radiative Transfer* was taken from Rybicki & Lightman (1986).

2.4.1 Definitions

2.4.1.1 Specific intensity

For molecular line emission, the energy, dE, carried by sets of rays, passing through a given area, dA, is defined as follow:

$$dE = I_\nu \, dA \, dt \, d\Omega \, d\nu \tag{2.24}$$

where $d\Omega$ is the solid angle, dt is the time interval and $d\nu$ is the frequency range. $I_\nu \equiv erg\ s^{-1}cm^{-2}sr^{-1}Hz^{-1}$ is the monochromatic intensity of the line frequency, ν. Rays passing through matter can gain energy from molecular emission or lose energy via absorption, hence the intensity will not remain constant.

2.4.1.2 Net flux

Consider a radiation field and a small element of area, dA, in some arbitrary direction **n**. The flux through the solid angle, $d\Omega$, is given by:

$$dF_\nu = I_\nu cos\theta d\Omega \tag{2.25}$$

where θ is the angle of incidence. The net flux is given by the integral of dF_ν over all solid angles:

$$F_\nu(erg^{-1}s^{-1}cm^{-2}Hz^{-1}) = \int I_\nu cos\theta d\Omega \tag{2.26}$$

The net flux would be zero when I_ν is an isotropic radiation field.

2.4.1.3 Emission

The spontaneous emission coefficient j_ν is defined by:

$$dE_\nu = j_\nu dV d\Omega dt \tag{2.27}$$

where j_ν has the units $erg\ cm^{-3}s^{-1}sr^{-1}Hz^{-1}$. dE is the energy emitted per unit time, dt, per unit volume, dV, per unit solid angle, $d\Omega$.

The isotropic emission, j_ν, can be written in terms of the emissivity, ε_ν, and the density, ρ:

$$j_\nu = \frac{\varepsilon_\nu \rho}{4\pi} \tag{2.28}$$

Consider radiation travelling through an emitting medium with infinitesimal thickness, ds. The intensity added to the beam due to emission is given by:

$$dI_\nu = j_\nu ds \tag{2.29}$$

2.4.1.4 Absorption

The equation of radiative transfer for a purely absorbing medium is given by:

$$dI_\nu = -\alpha_\nu I_\nu ds \tag{2.30}$$

Equation 2.30 represents the loss of intensity in a beam as it travels a distance, ds, with α_ν (cm^{-1}) as the absorption coefficient.

The coefficient α_ν can be written in terms of the monochromatic mass absorption coefficient or sometimes the opacity coefficient, κ_ν ($cm^2 g^{-1}$), and the density, ρ:

$$\alpha_\nu = \kappa_\nu \rho \tag{2.31}$$

The absorption term is considered to include both true absorption as well as stimulated emission. Thus the net absorption can be either negative or positive depending on which of the two processes, true absorption or stimulated emission, dominates.

2.4.2 The radiative transfer equation

The equation of radiative transfer is obtained by combining the effects of absorption (Equation 2.30) and emission (Equation 2.29):

$$dI_\nu = j_\nu ds - \alpha_\nu I_\nu ds \tag{2.32}$$

$$\Rightarrow \frac{dI_\nu}{ds} = -\alpha_\nu I_\nu + j_\nu \tag{2.33}$$

Equation 2.33 provides a useful formalism for the loss in energy due to absorption, the gain in energy by emission and stimulated emission.

2.4.3 Solutions to the equation of radiative transfer

2.4.3.1 Emission only: $\alpha_\nu = 0$

The transfer equation becomes:

$$\frac{dI_\nu}{ds} = j_\nu \tag{2.34}$$

The solution is given by:

$$I_\nu(s) = I_\nu(s_0) + \int_{s_0}^{s} j_\nu(s^{'}) ds^{'} \tag{2.35}$$

2.4.3.2 Absorption only: $j_\nu = 0$

The transfer equation can be written as:

$$\frac{dI_\nu}{ds} = -\alpha_\nu I_\nu \tag{2.36}$$

with a solution:

$$I_\nu(s) = I_\nu(s_0) \exp\left[- \int_{s_0}^{s} \alpha_\nu(s^{'}) ds^{'} \right] \tag{2.37}$$

2.4.3.3 Optical depth and the source function

Introducing the optical depth, $d\tau$, simplifies the radiative transfer equation. Optical depth describes the opacity of the medium and is defined as:

$$d\tau = \alpha_\nu ds \tag{2.38}$$

where α_ν is the absorption coefficient and ds the travel distance. The optical depth measured along the path of a travelling ray is given by:

$$\tau_\upsilon(s) = \int_{s_0}^{s} \alpha_\nu(s^{'}) ds^{'} \tag{2.39}$$

A medium is optically thick when τ_ν satisfies the condition $\tau_\nu > 1$ while for $\tau_\nu < 1$ the medium is optically thin. A photon travelling through an optically thick medium cannot travel the entirety of medium without being absorbed. In the case of a optically thin medium, there is still a chance for the photon to be absorbed, but the photon can also traverse the medium without being absorbed.

Dividing the equation of radiative transfer by α_ν and rewriting it in terms of the optical depth, gives:

$$\frac{dI_\nu}{d\tau_\nu} = -I_\nu + S_\nu \tag{2.40}$$

where S_ν is known as the ***Source function*** and is defined by:

$$S_\nu = \frac{j_\nu}{\alpha_\nu} \tag{2.41}$$

The equation of radiative transfer can now be formally solved by multiplying both sides of Equation 2.40 with e^{τ_ν} and defining the quantities $\tilde{I_\nu} \equiv I_\nu e^{-\tau_\nu}$ and $\tilde{S_\nu} \equiv S_\nu e^{\tau_\nu}$. The equation obtained is given by:

$$\frac{d\tilde{I_\nu}}{d\tau_\nu} = -\tilde{S_\nu} \tag{2.42}$$

The differential equation above can be rewritten as:

$$\int_{\tilde{I_\nu}}^{I_\nu} d\tilde{I_\nu} = \int_0^{\tau_\nu} \tilde{S_\nu} d\tau_\nu \tag{2.43}$$

with the solution:

$$I_\nu(\tau_\nu) = \tilde{I_\nu}(0) + \int_0^{\tau_\nu} \tilde{S_\nu}(\tau_\nu^{'}) d\tau_\nu^{'} \tag{2.44}$$

The formal solution of the radiative transfer equation in terms of I_ν and S_ν is given by:

$$I_\nu(\tau_\nu) = I_\nu(0)e^{-\tau_\nu} + \int_0^{\tau_\nu} S_\nu(\tau_\nu^{'})e^{-(\tau_\nu - \tau_\nu^{'})}d\tau_\nu^{'} \tag{2.45}$$

2.4.4 The Einstein coefficients

The Einstein coefficients define the transition energy from one energy level to another of a molecule. There are three processes occurring in the formation of a molecular spectral line i.e. spontaneous emission, stimulated emission and absorption. Einstein considered a system with two discrete energy levels. The first level has an energy, E, and a statistical weight, g_1. The second level has an energy, $E + h\nu_0$, and a statistical weight, g_2. Consider the case when the system is in the upper level. A photon will be emitted when the system makes a transition form level 2 to level 1. For the case when the system is in the lower level, a photon will be absorbed when the system makes a transition from level 1 to level 2. Figure 2.2 demonstrates the above scenario.

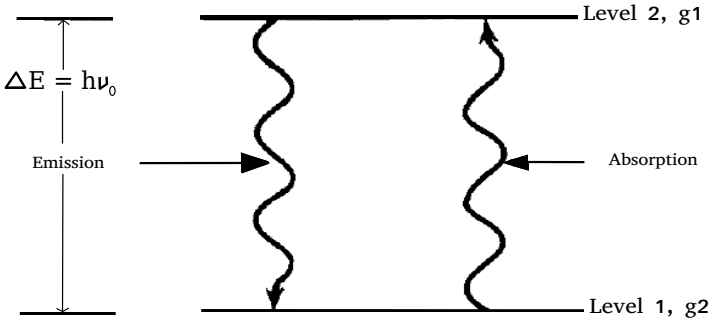

FIGURE 2.2: Emission and absorption from an atom with two energy levels (Rybicki & Lightman, 1986).

2.4.4.1 Spontaneous emission

Spontaneous emission occurs when the system is in the upper level and a photon is spontaneously emitted then the system will drop from the upper level, j, to the lower level, i . Spontaneous emission can also take place in the absence of a radiation field meaning it is independent of a radiation field. The Einstein A - coefficient is defined by: $A_{ji}(sec^{-1}) =$ *transition probability per unit time for spontaneous emission.*

2.4.4.2 Absorption

Absorption occurs when a photon of energy, $h\nu_0$, is absorbed and the system makes a transition from the lower level, i, to the upper level, j. For absorption to occur a radiation filed must be present. The Einstein B - coefficient is defined as: $B_{ij}\tilde{J}(sec^{-1}) =$ *transition probability per unit time for absorption.* Where the mean intensity $\tilde{J}$ is defined by:

$$\tilde{J} = \int_0^{\infty} J_\nu \phi(\nu) d\nu \tag{2.46}$$

with $\phi(\nu)$ the line profile function and ν the transition frequency range.

2.4.4.3 Stimulated emission

Stimulated emission occurs when the system makes a transition from the upper level, j, to the lower level, i, and since this process is also proportional to $\tilde{J}$, another Einstein B - coefficient can be defined as: $B_{ji}(sec^{-1})\tilde{J} =$ *transition probability per unit time for stimulated emission.* Stimulated emission can only take place in the presence of a radiation field.

2.4.5 Relations between the Einstein coefficients

In thermodynamic equilibrium, the transition rate per unit time per unit volume from level, i, to level, j, must be equal to the transition rate per unit time per unit volume from level, j, to level, i. The population density of the atoms in level i is given by n_i and in level j by n_j. Using the above, the following equation can be constructed:

$$n_i B_{ij}\tilde{J} = n_j A_{ji} + n_j B_{ji}\tilde{J} \tag{2.47}$$

Using Boltzmann's law for thermodynamic equilibrium, the ratio of n_i to n_j is given by:

$$\frac{n_i}{n_j} = \frac{g_i \exp(\frac{-E}{kT})}{g_j \exp[-(\frac{E+h\nu_0}{kT})]} \tag{2.48}$$

$$\Rightarrow \frac{n_i}{n_j} = \frac{g_i}{g_j}\exp(\frac{h\nu_0}{kT}) \tag{2.49}$$

Substituting Equation 2.49 into Equation 2.47 gives:

$$\tilde{J} = \frac{A_{ji}/B_{ji}}{(g_i B_{ij}/g_2 B_{ji})\exp(h\nu_0/kT) - 1} \tag{2.50}$$

In thermodynamic equilibrium Equation 2.50 is equal the Planck function, B_ν, for all temperatures from which the Einstein relations follow:

$$g_i B_{12} = g_j B_{ji} \tag{2.51}$$

$$A_{ji} = \frac{2h\nu^3}{c^2} B_{ji} \tag{2.52}$$

Equations 2.51 and 2.52 have no reference to temperature and therefore must hold whether or not the atoms are in thermodynamic equilibrium. Absorption and emission are connected through the Einstein relations. If one coefficient is known, these balanced relations allow the other coefficients to be determined.

2.4.6 The emission and absorptions coefficients in terms of the Einstein coefficients

2.4.6.1 Emission coefficient

Assuming the emission and absorption line profile functions are the same, $\phi(\nu)$. Then the emission coefficient, j_ν, can be defined in terms of the energy emitted from the volume, dV, into a solid angel, $d\Omega$, within a frequency range, $d\nu$, during time, dt, given as: $j_\nu dV d\Omega d\nu dt$. Since each transition gives a photon of energy, $h\nu_0$, distributed over 4π solid angel, this can be expressed as: $\frac{h\nu}{4\pi} n_j A_{ji} \phi(\nu) dV d\Omega d\nu dt$. Equating the two expressions gives:

$$j_\nu = \frac{h\nu}{4\pi} n_j A_{ji} \phi(\nu) \tag{2.53}$$

which is the *emission coefficient* in terms of the Einstein A coefficients.

2.4.6.2 Absorption coefficient

Using Equations 2.4.4.2 and 2.46 the total energy absorbed from a volume, dV, into a solid angel, $d\Omega$, within a frequency range, $d\nu$, during a time, dt, is expressed as: $dV d\Omega d\nu dt \frac{h\nu_0}{4\pi} n_i B_{ij} \phi(\nu) I_\nu$.

Using $dV = dAds$ and noting that $dE = I_\nu dA d\Omega d\nu dt$ and $dI_\nu = -\alpha_\nu I_\nu ds$, then the absorption coefficient is given by:

$$\alpha_\nu = \frac{h\nu}{4\pi} n_i B_{ij} \phi(\nu) \tag{2.54}$$

Equation 2.54 is uncorrected for stimulated emission. Treating stimulated emission as negative absorption, the absorption coefficient can be written as:

$$\alpha_\nu = \frac{h\nu}{4\pi} \phi(\nu)(n_i B_{ij} - n_2 B_{ji}) \tag{2.55}$$

Equation 2.55 is the stimulated-emission-corrected absorption coefficient.

2.4.6.3 Radiative transfer equation

Substituting Equations 2.53 2.55 into Equation 2.33, gives the radiative transfer equation in terms of the Einstein coefficients:

$$\frac{dI_\nu}{ds} = -\frac{h\nu}{4\pi}(n_i B_{ij} - n_j B_{ji})\phi(\nu) I_\nu + \frac{h\nu}{4\pi} n_j A_{ji} \phi(\nu) \tag{2.56}$$

2.5 Molecules

The line emission covered in the observations of this study are that of CO and methanol. Line emission occurs when the molecules are in an excited state and returns to a configuration of lower energy. Thus to best interpret the observed CO and methanol line emission, this section discuses some basic properties of the CO and methanol molecules. Since the main focus in this study is on the CO line emission a broader overview will be taken on the CO.

2.5.1 Carbon monoxide (CO)

Molecular hydrogen (H_2) is the most abundant molecule found in star forming regions. However these regions are shielded by gas and dust from destructive ultra-violet radiation and therefore these regions are cold. Thus cold H_2 has no emission line spectrum and therefore less abundant species such as CO are used for observations. CO, which has an abundance of 10^{-4} with respect to H_2, is the primary tracer of molecular gas (Emerson, 1996). CO is an abundant and relatively stable molecule, forming only through gas-phase reactions (Stahler & Palla, 2005). The molecule has a small dipole moment, making its transitions electric-dipole allowed (Ward-Thompson & Whitworth, 2011). This small dipole moment together with the small A-coefficients that CO has for rotational transitions, allows CO to thermalize quite easily (Elitzur, 1992). This makes CO a good tracer of temperature changes.

CO is a relatively massive molecule with a large moment of inertia, giving it closely spaced energy levels. Since CO has closely spaced rotational energy levels, it can be easily excited at low temperatures (Ward-Thompson & Whitworth, 2011). ^{12}CO is the most abundant isotope, but can be optically thick. Therefore other isotopes like ^{13}CO, with an abundance of 10^{-6} with respect to H_2, and C^{18}O , with an abundance of 10^{-7} with respect to H_2, which have optically thinner lines, can also provide useful information (Stahler & Palla, 2005).

2.5.1.1 Rotational energy levels

CO consist of a Carbon atom and an Oxygen atom, separated by a distance, d, making CO a linear rotator. The rotational energy, E, for a linear rotator is given by:

$$E = \frac{1}{2} I \omega^2 \tag{2.57}$$

where $I = \mu r^2$, for reduced mass, μ, is the moment of inertia (Emerson, 1996) and $\omega = 2\pi\nu_{rot}$, for rotation frequency ν_{rot} (Herzberg, 1950), is the angular frequency of rotation.

In classical mechanics the rotational energy is given by:

$$E_{rot} = \frac{1}{2I} P^2 \tag{2.58}$$

where P is the angular momentum (Herzberg, 1950). The angular momentum eigenvalues in quantum mechanics is given by:

$$J(J+1)(\frac{h}{2\pi})^2 \tag{2.59}$$

where J is the quantum number for the angular momentum, which has integer values $J = 1, 2, 3, ...$ (Emerson, 1996). Thus the rotational energy can be written as:

$$E_{rot} = J(J+1)(\frac{h}{2\pi})^2 \frac{1}{2I} \tag{2.60}$$

Introducing the rotational constant B as:

$$B = \frac{h}{8\pi I} \tag{2.61}$$

Then the rotational energy is given by:

$$E_{rot}(J) = hBJ(J+1) \tag{2.62}$$

Equation 2.62 only describes a completely rigid molecule (Emerson, 1996). The rotational energy will increase due to centrifugal stretching for even a slightly elastic molecule (Wilson et al., 2013). The rotational energy, corrected to the first order for centrifugal stretching, is given by:

$$E_{rot}(J) = hBJ(J+1) - hD[J(J+1)]^2 \tag{2.63}$$

where the constant D is given by:

$$D = \frac{4B^3}{\nu_{osc}^2} \tag{2.64}$$

with ν_{osc} as the oscillating frequency (Emerson, 1996). CO has no nuclear spin as well as no electronic angular momentum in the ground state (Emerson, 1996), making CO a simple case. Emerson (1996) gives the values of B and D in Equation 2.63 for CO, as follows

$$B \sim 5.76 \times 10^{10} s^{-1} \tag{2.65}$$

$$D \sim 1.8 \times 10^{5} s^{-1} \tag{2.66}$$

Substituting these values into Equation 2.63, the transitions for CO, ($v = 0$) $J = 1$ to $J = 0$ and $J = 2$ to $J = 1$, can be calculated. The transitions are illustrated in Figure 2.3.

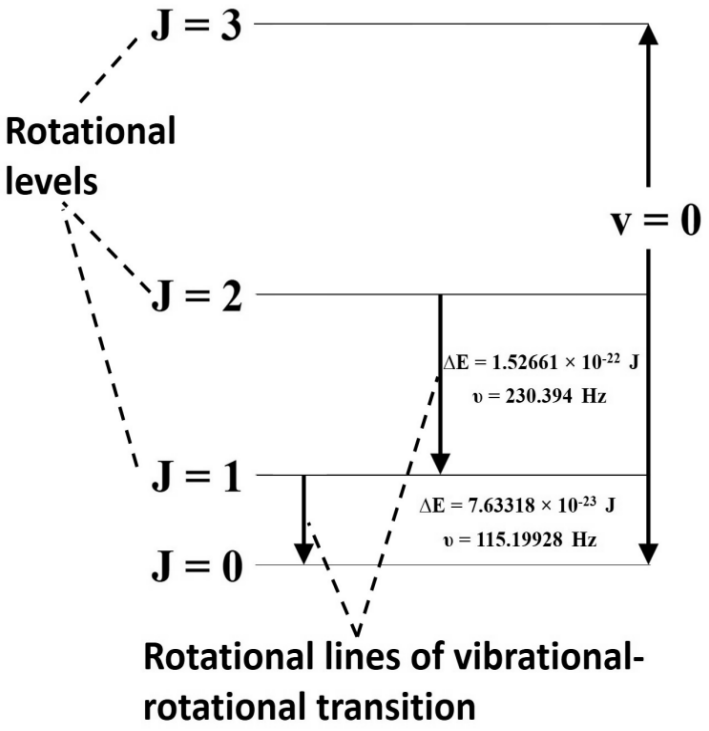

FIGURE 2.3: Rotational energy levels of CO within the ground vibrational state

2.5.1.2 Interpreting molecular line intensities

In this section the CO molecular lines will be used to determine temperatures and column densities.

Temperatures

The excitation temperature, T_{ex}, describes the population of excited energy levels by means of the Boltzmann distribution (Emerson, 1996). The extinction coefficient, κ_ν, is needed to obtain the excitation temperature, and is given by:

$$\kappa_\nu = \frac{h\nu_0}{c} n_i B_{ij} (1 - \frac{g_i n_2}{g_j n_i}) \phi(\nu) \tag{2.67}$$

rearranging Equation 2.49 gives:

$$\frac{g_i n_j}{g_j n_i} = \exp(-\frac{h\nu_0}{kT}) \tag{2.68}$$

which can be substituted into Equation 2.67, giving:

$$\kappa_\nu = \frac{h\nu_0}{c} n_i B_{ij} [1 - \exp(-\frac{h\nu_0}{kT})] \phi(\nu) \tag{2.69}$$

The coefficient B_{ij} in Equation 2.52 is given by:

$$B_{ij} = \frac{g_j}{g_i} A_{ji} \frac{c^3}{8\pi h\nu^3} \tag{2.70}$$

then κ_ν is defined as:

$$\kappa_\nu = \frac{c^2}{8\pi\nu_0^2} \frac{g_j}{g_i} N_i A_{ji} [1 - \exp(-\frac{h\nu}{kT_{ex}})] \phi(\nu) \tag{2.71}$$

where N_1 represents the lower level population and T_{ex} is the ***excitation temperature*** (Wilson et al., 2013). Thus T_{ex} is the temperature that when substituted into the Boltzmann distribution (Equation 2.68) gives the observed ratio of two energy states.

The ***brightness temperature*** ,T_B, is the temperature of a blackbody that reproduces a given flux density at a specific frequency. For a homogeneous source with optical depth, τ_ν, the intensity, I_ν, in Equation 2.45, can be replaced with the brightness temperature, T_B, (Emerson, 1996) giving:

$$T_B = T_{ex}[1 - e^{-\tau_\nu}] \tag{2.72}$$

Thus the brightness temperature is given by:

$$T_B = \frac{h\nu}{k} \frac{1 - e^{-\tau_\nu}}{e^{\frac{h\nu}{kT_{ex}}} - 1} \tag{2.73}$$

The brightness temperature for an optical thin source ($\tau_\nu \ll 1$) is given by:

$$T_B = T_{ex}\tau_\nu \tag{2.74}$$

Column density

For the optical thin case, integrating the brightness temperature, T_B, over the line profile, $\phi(\nu)$, gives:

$$\int T_B d\nu = T_{ex}\rho R \int \kappa_\nu \tag{2.75}$$

Substituting κ_ν (Equation 2.71) into Equation 2.75, gives:

$$\int T_B d\nu = T_{ex}\rho R A_{ji} \frac{g_j}{g_i} \frac{c^2 h}{8\pi k} \frac{N_i}{T_{ex}\nu} \int \phi(\nu) d\nu \tag{2.76}$$

for $\frac{h\nu}{kT_{ex}} \ll 1$ (Emerson, 1996). Simplifying Equation 2.76 gives:

$$\int T_B d\nu = \frac{c^2 h}{8\pi k} \frac{g_j A_{ji}}{g_i} \frac{1}{\nu} \frac{N_i}{N_{TOT}} (N_{TOT}\rho R) \tag{2.77}$$

where N_{TOT} is the total level population and $N_{TOT}\rho R$ is the *column density* (Emerson, 1996).

Temperatures and column density of CO

In particular reference to CO the following substitutions can be made in Equation 2.77. The frequency, ν, for a transition from an upper level $2J+1$ to a lower $J+1$ is $2B(J+1)$ (Emerson, 1996). The statistical weights g_i and g_j are given by $2J+1$ and $2J+3$ respectively. The ratio $\frac{N_i}{N_{TOT}}$ is characterized by the partition function, U ,and the excitation temperature, T_{ex} (Emerson, 1996). The partition function, U, is given by:

$$U = (2J+1)\exp[-\frac{hBJ(J+1)}{kT_{ex}}] \tag{2.78}$$

Thus for an optically thin homogeneous cloud, the brightness temperature is given by:

$$\int T_B d\nu = \frac{c^2 h}{8\pi k} \frac{g_j A_{ji}}{g_i} \frac{1}{\nu} \frac{g_i}{U} \exp[-\frac{E}{kT_{ex}}](N_{TOT}\rho R) \tag{2.79}$$

$$\Rightarrow \int T_B d\nu = \frac{c^2 h}{8\pi k} A_{ji} \frac{(2J+3)}{(2J+1)} \frac{1}{2B(J+1)} \frac{hB}{kT_{ex}} (2J+1)\exp[-\frac{hBJ(J+1)}{kT_{ex}}](N_{TOT}\rho R) \tag{2.80}$$

$$\Rightarrow \int T_B d\nu = \frac{c^2 h^2}{16\pi k h^2} A_{ji} \frac{(2J+3)}{(J+1)} \frac{1}{T_{ex}} \exp[-\frac{hBJ(J+1)}{kT_{ex}}](N_{TOT}\rho R) \tag{2.81}$$

where i and j represent the lower and upper energy levels respectively (Emerson, 1996). Substituting the emission coefficient $A_{ji} = 1.046 \times 10^{21} \nu^3 d_p^2 \frac{J+1}{2J+3}$, where d_p is the permanent dipole moment and the frequency $\nu^3 = 8B^3(J+1)^3$, into Equation 2.81:

$$\int T_B d\nu = \frac{32\pi^3 h}{3ck^2(4\pi\epsilon_0)} \frac{B^3(J+1)^3}{T_{ex}} d_p^2 \exp[-\frac{hBJ(J+1)}{kT_{ex}}](N_{TOT}\rho R) \tag{2.82}$$

^{12}CO in general is optically thick, leading to saturated ^{12}CO lines (Emerson, 1996). Therefore to estimate a more accurate total column density, CO isotopes such as ^{13}CO and C^{18}O are used. Assuming that ^{12}CO is in local thermodynamic equilibrium (LTE) and optically thick, the excitation temperature is given by the brightness temperature at the ^{12}CO line center (Emerson, 1996). Assuming ^{13}CO has the same excitation temperature as ^{12}CO and considering that the

^{13}CO lines are more or less optically thin, Equation 2.82 needs to be multiplied by the $\frac{^{12}CO}{^{13}CO}$ isotope ratio in order to obtain the total column density.

Since the brightness temperature $T_B = T_{ex}(1 - e^{-\tau})$ and the excitation temperature, T_{ex}, are the same for ^{12}CO and ^{13}CO, the following ratio can be given:

$$\frac{T_B(^{12}CO)}{T_B(^{13}CO)} = \frac{(1 - e^{-\tau(^{12}CO)})}{(1 - e^{-\tau(^{13}CO)})} \tag{2.83}$$

The isotopic abundance ratio is given by:

$$\frac{N(^{12}CO)}{N(^{13}CO)} = R \tag{2.84}$$

then

$$\tau(^{12}CO) = R\tau(^{13}CO) \tag{2.85}$$

and equation 2.83 can be solved, at each frequency in the line, for $\tau_\nu(^{13}CO)$ (Emerson, 1996).

Rewriting the integral (Equation 2.82) in terms of velocity V, where $d\nu = \frac{v}{c}dV$ and $\tau_\nu = \frac{T_B}{T_{ex}}$ gives:

$$\int \tau_\nu dV = \frac{16\pi^3 h}{3k^2 4\pi\epsilon_0} \frac{B^2(J+1)^2}{T_{ex}^2} d_p^2 exp[-\frac{hBJ(J+1)}{kT_{ex}}](N_{TOT}\rho R) \tag{2.86}$$

Equation 2.86 only holds for long wavelength approximations and does not hold for CO at low temperatures (Emerson, 1996). Without this approximation Equation 2.86 becomes:

$$\int \tau_\nu dV = \frac{c^2}{8\pi\nu^3} \frac{A_{ji} g_i}{U} exp(\frac{-E_i}{kT_{ex}}) N_{TOT}\rho R(1 - e^{-h\nu/kT_{ex}}) \tag{2.87}$$

For diatomic molecules a different approximation for the partition function is used and Equation 2.87 becomes:

$$\int \tau_\nu dV = \frac{8\pi^3 B d_p^2}{3k4\pi\epsilon_0} \frac{N_{TOT}\rho R(J+1) exp[-hBJ(J+1)/kT_{ex}]}{T_{ex} + hB/3k}(1 - e^{h\nu/kT_{ex}}) \tag{2.88}$$

Emerson (1996) lists the following values for the constant $\frac{hB}{3k}$:

$$^{12}CO : \frac{hB}{3k} = 0.93 \tag{2.89}$$

$$^{13}CO : \frac{hB}{3k} = 0.89 \tag{2.90}$$

The column densities for ^{12}CO and ^{13}CO is then given by:

$$N_{TOT}\rho R(^{12}CO) = 2.39 \times 10^{15} \frac{exp[hBJ(J+1)/kT_{ex}]}{J+1} \frac{T_{ex} + 0.93}{1 - exp[-h\nu/kT_{ex}]} \int \tau dV m^{-2} \tag{2.91}$$

$$N_{TOT}\rho R(^{12}CO) = 2.49 \times 10^{15} \frac{exp[hBJ(J+1)/kT_{ex}]}{J+1} \frac{T_{ex} + 0.89}{1 - exp[-h\nu/kT_{ex}]} \int \tau dV m^{-2} \tag{2.92}$$

The column density is the amount of intervening matter between the observer and the object that is begin observed. Column densities play an important role in the chemical compositions of

star forming regions since they can be used to determine the column densities of H_2, molecular volume densities, etc. However for this study the main focus will be on the density of the gas, n_{H_2}, and the critical densities, n_{crit}, of the CO(2-1) transitions.

2.5.1.3 Mass of the dust and molecular gas

Following Hildebrand (1983), it is possible to estimate the dust mass and the molecular gas mass from the dust emission. The integrated flux density, S_ν, of the emission can be expressed as:

$$S_\nu = \frac{\kappa_\nu \, B_\nu(T_d) \, M_d}{D^2} \tag{2.93}$$

where $B_\nu(T_d)$ is the Planck function, κ_ν the dust opacity per unit mass, D the distance at which the source is located and M_d is the mass of the dust.

The value of κ_ν can be obtained from Weingartner & Draine (2001). The observation in this study are sub-millimetre observations $\sim$ 230 GHz, thus the value of κ_ν is 0.19 cm^2 g^{-1}. Since M_d is only the mass of the dust, from literature (Kruegel, 2003) and (Liu et al., 2017), a gas to dust mass ratio of 100 is assumed to obtain the mass of the molecular gas. Knowing the mass of the molecular gas also leads to determining the density of the molecular gas.

2.5.2 Methanol (CH_3OH)

Methanol is the simplest organic compound containing a hydroxyl group (OH), detected in the interstellar medium. CH_3OH is an asymmetric top molecule and was first discovered by Ball et al. (1970) in Sagittarius. The observed methanol lines arise from internal rotation of the OH bond about the axis of the CH_3 tetrahedron (Stahler & Palla, 2005), but the rotation is hindered by mutual interaction between the two groups (Elitzur, 1992). The combination of the hindered rotation as well as the asymmetry of the molecule lead to a complex energy spectrum for methanol. Figure 2.4 is a schematic structure of CH_3OH. The dashed line represents the symmetry axis of the CH_3 group and the CO bond is tilted with respect to the symmetry axis.

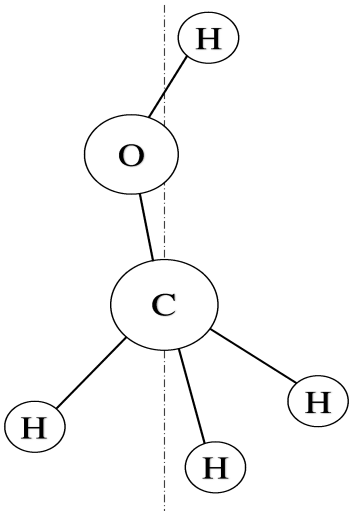

FIGURE 2.4: Schematic structure of the methanol molecule.

Methanol has two types of configurations, E-type and A-type. The way in which the OH tunnels through the complex potential barrier, created by the CH_3, distinguishes these two types of transitions (Stahler & Palla, 2005). Thus E- and A-methanol can be considered as two distinct molecules. Figure 2.5 shows the rotational energy levels of both E- and A-methanol types. J_K characterizes the rotational states in the two types of methanol, where J is the angular momentum and K the component on the molecular symmetry axis (Elitzur, 1992). The quantum number k is used for E species and for species A, the levels are designated by $K = |k|$.

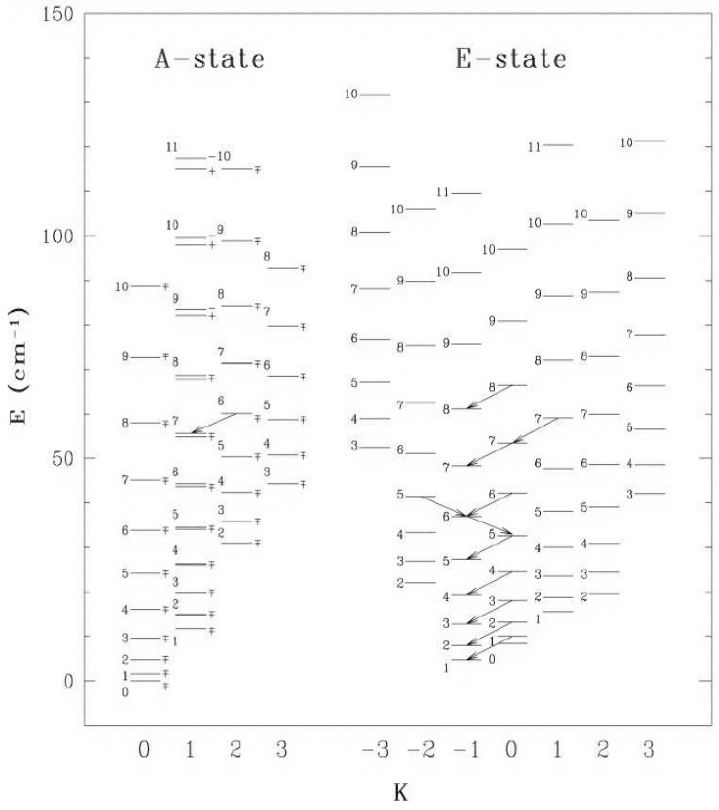

FIGURE 2.5: The rotational energy levels for E and A methanol (Mahmoud, 2006).

2.6 Microwave amplification by stimulated emission of radiation (Masers)

This brief discussion on periodic methanol masers is due to the target regions association with periodic methanol masers, which was also the main reason these regions were chosen for this study. A maser is a source of stimulated spectral line emission (Humphreys, 2011). They are observed from various objects in the sky, however methanol masers observed from star forming regions will be the main focus. Masers arise from molecules such as methanol (CH_3OH), water (H_2O) and hydroxyl radicals. Masers have high brightness temperatures and are usually compact. The maser emission may be polarized and variable, they also display narrow spectral line widths (Humphreys, 2011).

Masers originate in regions of gas in which the amplification of microwave and radio wavelength radiation takes place (Humphreys, 2011). The energy difference between two energy levels of the masing molecule in the gas, corresponds to the specific frequency at which maser amplification occurs. Masers are generated by stimulated emission, which occur when the population of a meta-stable higher energy level is larger than the population of a lower energy level. This creates a population inversion (Humphreys, 2011). To maintain the population inversion an energy source/maser pump is needed. This energy source can be collisional, radiative or chemical in nature (Humphreys, 2011).

2.6.1 Methanol masers

Methanol masers are excellent indicators of the early stages of star formation. Menten (1991) divided them into two classes, Class I and Class II methanol masers. Class I methanol maser transitions show activity in the 25 GHz J_2 - J_1 E lines. These masers are found offset from infrared sources and other masers transitions (Menten, 1991). Class II methanol masers are closely associated with infrared sources, UCH II regions and OH or H_2O masers. Class II methanol masers show activity in the 6.7, 12, 19 and 23 GHz lines (Menten, 1991), from these the 6.7 GHz methanol masers are the most well known.

2.6.1.1 6.7 GHz methanol masers

A number of 6.7GHz methanol masers have been found to show variability. This variability was established by Caswell et al. (1995). Goedhart et al. (2004) characterized the variability behaviour as monotonic, quasi-periodic and periodic variations. The cause of variability is unclear. It could be due to amplified changes in the background radiation field or it might be due to changes in the physical conditions in the masing region that affects the population inversion (van der Walt, 2011). The periodic variations of methanol masers are mainly characterized by two types of light curves: a light curve showing a flare-like pattern or a Bunny hop pattern (Szymczak et al., 2015).

Araya et al. (2010) suggests that periodic accretion of circumbinary disk material is responsible for the flare pattern light curve. They proposed this mechanism specifically for IRAS 18566+0408. Material accretes onto the accretion disk or protostar from the circumbinary disk. This accretion heats the dust and increases the infrared radiation field, that results in higher microwave amplification due to greater maser gain (Araya et al., 2010). van der Walt (2011)

suggested a colliding-wind binary (CWB) scenario to explain the flare-like profile in the light curve shape. The CWB model is specifically based on the light curve of G9.62+0.0.19E. Ionized radiation passing through a volume of partially ionized gas causes changes in the electron density, which in turn cause changes in the background free-free emission (van der Walt, 2011). Along with these mechanisms several other mechanisms have been suggested by others, like (Inayoshi et al., 2013), but still no clear cause of periodicity exist.

Chapter 3

INTERFEROMETRY, OBSERVATIONS AND DATA REDUCTION

3.1 Introduction

This chapter will be used to give a very brief overview on interferometry. The advantage of this observational technique is that when separate telescopes are combined, they can be used to obtain images with the same angular resolution as that produced by a large single-dish telescope. The interferometry section in this chapter contains a number of points that are only mentioned but not discussed. This chapter also contains the details of the ALMA and SMA observations of the target sources G9.62+0.19E, G22.357+0.066 and G25.411+0.105.

3.2 Radio interferometry

A radio interferometer is an array of radio telescope antennas, working together as a single radio telescope. The main purpose of combining radio telescopes is to obtain higher resolution images. The overview on interferometry is taken from both Wilson et al. (2013) and Thompson et al. (2017).

The sizes of single dish telescopes are limited by materials, giving them limited angular resolution $\theta \sim \frac{\lambda}{D}$, where λ is the wavelength of the radiation received and D is the diameter of the dish. In order to obtain better angular resolution, the diameter must be increased for a fixed wavelength, λ. This can be done by coherently combining the output of two dishes (Wilson et al., 2013). The two dishes of diameter, d, each are separated by a distance D where $d < D$.

The challenges of the observational study of high-mass star forming regions are gradually being tackled with improved resolutions and sensitivities offered by new and recently upgraded instruments around the globe.

3.2.1 Angular resolution

The resolving power of a radio telescope is the ability to distinguish between two separate objects, located at a small angular distance. The angular resolution of an interferometric array is given by:

$$\theta \sim \frac{\lambda}{B} \tag{3.1}$$

where B is the largest separation between any two dishes in the array, also called the maximum baseline.

As explained above, the reason behind the development of interferometers is to obtain better angular resolution. For a more practical explanation consider the examples presented in Table 3.1. Moving from top to bottom the angular resolution calculations illustrate the improvement in the telescopes ability to differentiate between closely located objects. By simply increasing the diameter of a single dish from 15 m, of the JCMT telescope, to 30 m of the IRAM single dish telescope gives an approximate of $4''$ improvement in angular resolution. These angular resolutions are however extremely coarse when compared to the resolution obtained by interferometer arrays, which can have kilometre baselines between the furthest dishes. These long maximum baselines can provide sub-arcsecond angular resolution which single dish telescopes cannot.

TABLE 3.1: The angular resolutions of two single dish telescopes and two interferometers.

Telescope	Diameter/Baseline m	Frequency GHz	Angular resolution $''$
JCMT	15	345	14.59
IRAM	30	230	10.94
SMA	500	345	0.44
ALMA	8500	230	0.05

From Table 3.1 it is clear that a larger diameter/baseline is needed in order to obtain a better angular resolution. The question could be asked, why is improved angular resolution important? The angular resolution determines the observational area distance. Assume a high-mass star forming is observed at a distance of 2 kpc. Apply the calculation $s = r\theta$, the observational area distance, s, is obtained. For the single dish telescope, IRAM, s is 2.11×10^4 AU compared to ALMAs observational area distance, s, that is 74.6 AU. Thus the better the angular resolution, the smaller the observational area distance and the more detail can be obtained from an image.

3.2.2 Sensitivity

The sensitivity of a telescope can be defined as the minimum signal brightness that it can detect. If the sensitivity is the smallest signal that a telescope can detect from a source then a telescope with a very high sensitivity will be be able to detect very weak objects. Since high-mass star forming regions are located at large distances, the telescope used to observe these regions must have the greatest sensitivity possible.

The sensitivity for a radio telescope is measured by:

$$S_{\nu,rms} = 2k\frac{T_{sys}\exp(\tau)}{A_e\sqrt{2t \triangle \nu}} \tag{3.2}$$

where T_{sys} is the system temperature, τ the optical depth, A_e the effective area, t the integration time in seconds and $\triangle\ \nu$ the observational bandwidth (Wilson et al., 2013). Referring to Equation 3.2, to minimize $S_{\nu,rms}$, the system temperature, T_{sys}, will need to be at its minimum. Reducing the system temperature of a telescope can be achieved by cooling the receiver of the telescope and also by observing during optimal weather conditions, meaning no clouds or rain. However, sensitivity is inversely proportional to the effective collecting area, the integration time on the source and the bandwidth. Thus the sensitivity will be improved by adding another dish to the interferometer or by upgrading the efficiency of the existing dishes. The sensitivity will also improve by increasing the integration time and the bandwidth.

3.2.3 Basic terms and definitions

This section is used to define some of the terms that are used in radio interferometry.

Amplitude: The amplitude of a complex signal is the total amount of power of a certain spatial frequency received by each telescope.

Phase: The phase identifies the location of the spatial frequency component. The phase between the signal received at each telescope is dependent on the observing wavelength and the geometric delay.

The Fourier transform (FT): The Fourier transform approximates any signal as a sum of periodic signals, decomposing the signal into cosine and sine components.

Interferometer: Young's double slit experiment is used to explain the basic concept of an interferometer. When the path difference in the double slit experiment is an integer of wavelengths λ, then constructive interference "fringes" occurs. Maximum interference occur when signals from the two slits arrive in phase, $B\sin(\theta) = m\lambda$ and $m\epsilon Z$. While incoherence occur when the signals arrive out of phase and cancel each other out, $B\sin(\theta) = (m + \frac{1}{2})\lambda$. Let B define the double slit separation and m is any positive or negative integer.

An interferometer, like a double slit experiment, measures the interference pattern produced by multiple antennas. The antennas in the interferometer are like the slits, meaning more slits, or rather more antennas, will produces more information which leads to more detailed images. A source is resolved when its angular size is larger than the distance between adjacent positive and negative fringes. The size of small unresolved sources is measured by long baselines, where as short baselines are used to image large sources that are resolved by longer baselines.

3.2.4 Two element interferometer

Some basic understanding of a single-dish telescope is needed since an interferometer acts as a very large single-dish. This will only be a very brief overview on single-dish telescopes. A single-dish has a primary beam, sidelobes and backlobes which are shown in Figure 3.1. It images the sky by letting the target source drift across the beam and measures the power received as a function of time. The sensitivity of a single-dish depends on the effective area A_e, meaning the larger the effective area, the greater the sensitivity, Equation 3.2.

There are advantages to using a single-dish telescope. Firstly single-dish telescopes are more available to use than arrays. Secondly a single-dish does not have the problem of coordinating between many antennas. The biggest drawback with single dish telescopes is that only the signal power can be measured, no phase information is available.

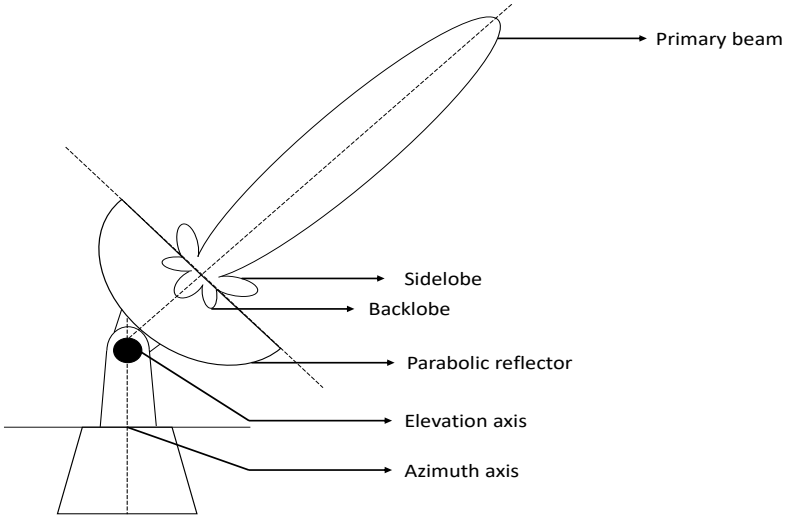

FIGURE 3.1: Single-dish radio telescope

Since interferometric telescope arrays can be divided into a number of two-element baselines, analysing a single baseline component provides the foundation to analyse more advanced radio telescope arrays. For simplicity, consider a monochromatic interferometer pair with a path difference described by a single phase difference as shown in Figure 3.2. The interferometer has two antennas A_1 and A_2 that are separated by a distance B. Because of the separation of the antennas and the direction of the incident signal, the signal will reach antenna 2 a small time ahead of the wave front reaching antenna 1. This means a small geometric delay has to be applied to the signal measured at antenna 1 to ensure when the signals from the two antennas are combined, they are in phase. These are the antenna output voltages V_1 and V_2 with τ_i the instrumental delay and τ_g the geometric delay. The geometric delay (seconds) is given by:

$$\tau_g = \mathbf{B} \cdot \hat{s}/c \tag{3.3}$$

where $\hat{s}$ is the unit vector in the direction of the source and $\mathbf{B}$ is the baseline vector. The difference between τ_g and τ_i is the delay tracking error $\tau = \tau_g - \tau_i$.

The antennas receive a signal which is amplified by each antenna before being converted into voltages:

$$\begin{aligned} V_1 &= E\cos(\omega t) + N(t) \\ V_2 &= E\cos[\omega(t-\tau_g)] + N(t) \end{aligned} \tag{3.4}$$

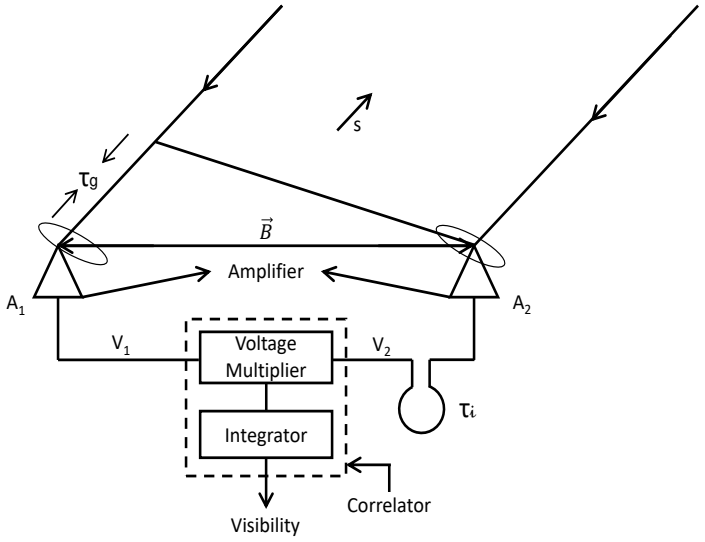

FIGURE 3.2: Two element interferometer

with E the signal electric field, $\omega = 2\pi\nu$ the angular frequency and N the additive noise. The voltages are combined in a correlator, where they are cross multiplied to obtain the response R_c:

$$\begin{aligned} R_c &\equiv (V_1 + V_2)^2 \\ &= V_1^2 + V_2^2 + 2(V_1 \times V_2) \end{aligned} \tag{3.5}$$

The voltages and the response are averaged over a time interval $t \gg \frac{1}{\omega}$. V_1^2 and V_2^2 will average to zero since they include the noise N_1^2 and N_2^2, that contains uncorrelated fluctuations. The response will then be:

$$R_c \equiv V_1 \times V_2 \tag{3.6}$$

A correlator produces a real response, R_c, and an imaginary response, R_s, both are needed for the fringe pattern to remain stationary with respect to the source. Correlators with these outputs are known as complex correlators, since their outputs are manipulated as complex numbers combing the amplitude and phase of the signal. To account for the imaginary part, the voltages are rewritten, making use of complex numbers:

$$\begin{aligned} V_1 &= E\cos(\omega t) = Re\{Ae^{-i\omega t}\} \\ V_2 &= E\cos[\omega(t - \mathbf{B}\cdot\hat{s}/c)] = Re\{Ae^{-i\omega(t-\mathbf{B}\cdot\hat{s}/c)}\} \end{aligned} \tag{3.7}$$

The correlated power P would then be:

$$P_{corr} = < V_1 V_2^* >= A^2 e^{-i\omega\mathbf{B}\cdot\hat{s}/c} \tag{3.8}$$

where V_1 is time averaged and V_2 is the complex conjugate.

Consider a two-element interferometer observing a source with a brightness distribution $I_\nu(s)$, then the output of the complex correlator is the power received per unit bandwidth, $d\nu$, from an element of the source ds:

$$R_{12} = I_\nu(s)\cos(2\pi\nu\tau_g)dsd\nu \tag{3.9}$$

The total response is obtained by integrating over the solid angle, $d\Omega$, subtended by the source:

$$R_c = \int\int I_\nu(s)\cos(2\pi\nu\mathbf{B}\cdot\hat{s}/c)d\Omega \tag{3.10}$$

R_c samples the even part of $I_\nu(s)$. To recover the full source brightness distribution the odd part of $I_\nu(s)$ is also needed and is given by:

$$R_s = \int\int I_\nu(s)\sin(2\pi\nu\mathbf{B}\cdot\hat{s}/c)d\Omega \tag{3.11}$$

The complex visibility describes the response of an interferometer with a complex correlator to an extended source:

$$V(\mathbf{b}) = R_c - iR_s = \int\int I_\nu(s)e^{-2\pi i\nu\mathbf{B}\cdot\hat{s}/c}d\Omega \tag{3.12}$$

The visibility function is the FT of the source brightness distribution (van Cittert-Zernike Theorem).

3.2.4.1 Coordinate system

To synthesize a map of the sky, a (u, v, w) coordinate system is introduced and shown in Figure 3.3 . The frame is oriented so that the plane containing the antennas lies on a plane with $w = 0$. Since w is towards the source, u will be towards the east and v towards north which is known as the uv-plane. The baseline vector **b** is specified by (u, v, w) and measured in terms of wavelengths, λ, thus $\mathbf{b} = (\lambda u, \lambda v, 0)$. The arbitrary unit vector **s** is defined by the components (l, m, n). The components (l, m, n) are known as direction cosines and they are projections of **s** onto the uv-plane (Thompson et al., 2017). The direction cosines are given by $l = cos(\alpha), m = cos(\beta)$ and $n = cos(\theta)$.

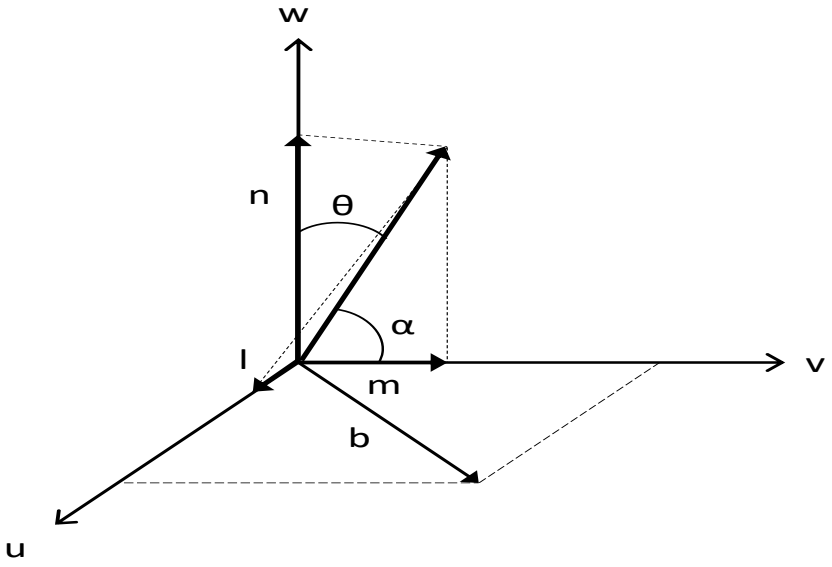

FIGURE 3.3: (u, v, w) coordinate system

Using the introduced coordinate system, the visibility can be rewritten as:

$$V(u,v,w) = \int\int \frac{I_v(l,m)}{\sqrt{1-l^2-m^2}} \exp[2\pi i(ul+vm+w\sqrt{1-l^2-m^2-1})]dldm \quad (3.13)$$

Since $w = 0$ the two dimensional form of the visibility is given by:

$$V(u,v,w) = \int\int I_v(l,m) \exp[2\pi i(ul+vm)]dldm \quad (3.14)$$

This equation is known as the van *Cittert-Zernike* relation and its Fourier inversion leads to:

$$I_v(l,m) = \int\int V(u,v,w) \exp[2\pi i(ul+vm)]dudv \quad (3.15)$$

Thus

$$I_v(l,m) \Leftrightarrow V(u,v,w) \quad (3.16)$$

is the two dimensional Fourier relation between the projected brightness $I(l,m)$ and the visibility $V(u,v,w)$.

3.2.5 Calibration

The goal of calibration is to correct the phase and amplitude for instrumental and atmospheric effects. This is a very basic summary of the types of calibrators and their functions.

Gain calibrator: Solves atmospheric and instrumental variations with time - corrects the phase as a function of time.

Bandpass calibrator: Solves instrumental variations with frequency - corrects the phase as a function of frequency.

Flux calibrator: Sets absolute flux of all sources observed by applying an amplitude scale factor.

3.2.6 Classic CLEAN algorithm

Sampling of the uv-plane is often incomplete, therefore image reconstruction algorithms (which will not be discussed) are needed to produce images of a source. The FT of a sampling function is called the point spread function (PSF). The PSF is referred to as the *Dirty Beam*, since it contains side-lobes. The Fourier inversion $I(l,m)$ of the visibility function produces a *Dirty Map*. The CLEAN algorithm attempts to deconvolve the *Dirty Beam* from the *Dirty Ma*p. The basic steps of a CLEAN algorithm are summarized here.

- Make the dirty map, then find the position and the intensity of the strongest point source on the map.
- Subtract some scaled fraction of the dirty beam response at this position from the dirty map. Store the position and intensity as a 'CLEAN component' of the dirty map.
- Find the strongest point source in the new dirty map and add it to the 'CLEAN component' of the dirty map. Repeat this process until only noise is left in the dirty map.

- To produce the final clean map, the residual noise left in the dirty images is added to all the 'CLEAN components'. The image is then convolved with a Gaussian fit that was fitted to the central lobe of the dirty beam.

3.3 Observations

This section contains the details on the SMA and ALMA observations.

3.3.1 Sub-Millimetre Array (SMA) observations

The target sources G22.357+0.066 and G25.411+0.105 were observed on June 27, 2016 during a 5-hour track with the SMA in a compact array configuration. The SMA $\sim$ 230 GHz broad band covered the dust continuum and the spectral lines, ^{12}CO, ^{13}CO and C^{18}O for the transition J = 2-1, using 7 of its 8 antennas.

The 8 GHz bandwidth is divided into two side-bands, lower side-band and upper side-band. Each side-band consists of 128 channels, with a channel spacing of 1.1 km s^{-1}. The lower side-band covered the frequency range of 212.9 GHz to 220.6 GHz and the upper side-band covered a frequency range of 228.7 GHz to 236.6 GHz. The calibrators and the two target sources were observed in turn, leading to a total observation time of 80 minutes for each target source.

The full data calibration and imaging were done in CASA **4.7.0**. 3C279 was used as the bandpass calibrator and Titan as the flux calibrator. The antenna gain correction was done using J1733−130 and J1743−038 as the calibrators. Some bad data points were flagged, but there were only a few line-free channels used to produce the dust continuum image. The CASA clean task was used to produce the molecular line emission spectra of ^{12}CO, ^{13}CO and C^{18}O with their rest frequencies as 230.53800000 GHz, 220.39868420 GHz and 219.56035410 GHz respectively. The rest frequencies was obtained from the Splatalogue catalogue. The channel width for all the line emission spectra is 1.2 km s^{-1}.

The root-mean-square (rms) noise level in the continuum and line images was $\sim$ 1 mJy beam^{-1} and $\sim$ 47 mJy beam^{-1} respectively. The primary beam size was calculated to be $\sim 54''$. The synthesized beam size for the continuum is $2''.26 \times 5\,''.63$ and $1''\,.41 \times 5''\,.82$ for the spectral line images.

3.3.2 ALMA Archival Data

For G9.62+0.19E, ALMA band 6 archival data on G9.62+0.19 (Project ID: 2013.1.00957.S) was used. The overview on the ALMA observations was taken from Liu et al. (2017). The observations were done on April 27, 2015 using 39 antennas and on May 24 using 34 antennas in the compact and extended configurations, respectively. G9.62+0.19 was also observed with the ALMA Compact Array (ACA: 7-m array) on May 04, 2015 with 10 antennas. J1733−1304 and J1517−2422 were used as the bandpass calibrator and the phase calibrator, respectively. Neptune, Titan and J1733−130 were used as flux calibrators.

The Band 6 (230 GHz) receivers were used for the observations in dual-polarization mode. To cover the molecular lines such as ^{12}CO (2-1) and CH_3OH $v_t = 1$ ($6_{1,5}$-$7_{2,6}$), five spectral windows with a bandwidth of 117 MHz in each window, as well as another spectral window with a bandwidth of 234 MHz, was used. The channel width in all the spectra windows is 0.08 km s^{-1}. The ALMA data was also calibrated in CASA. They combined data from three configurations in CASA, that included single dish data.

The continuum image has a rms noise of 0.8 mJy and a synthesized beam of $0''.94 \times 0\,''.71$. For the molecular lines the rms noise $\sim$ 10 mJy beam^{-1} per 0.16 km s^{-1} channel. The lines CO (2-1) and CH_3OH $v_t = 1$ ($6_{1,5}$-$7_{2,6}$) has synthesized beam sizes of $0''.94 \times 0\,''.73$ and $0''.99 \times 0\,''.72$ receptively. The rest frequency used for CH_3OH $v_t = 1$ ($6_{1,5}$-$7_{2,6}$) was 217.29920 GHz and was also obtained from the Splatalogue catalogue.

Chapter 4

RESULTS AND DISCUSSION

4.1 Introduction

In this chapter the results of this study are presented and discussed with reference to the aim of the study, which was to determine if there is any indication in the dust or molecular line emission that suggest differences or similarities between these regions. The continuum images, molecular line emission images and the line spectra of G22.357+0.066, G25.411+0.105 and G9.62+0.19E are presented in this chapter. All the images were analysed, discussed and compared. For the reader to follow a comfortable flow of text it was decided to present the channel maps (Figure 4.22 $\sim$ 4.30) at the back of this chapter.

4.2 Results

4.2.1 G22.357+0.066

4.2.1.1 1.3 mm continuum emission

Figure 4.1 shows the millimetre continuum of G22.357+0.066. Seven millimetre continuum cores (MM1 to MM7) were detected from the SMA observations. Table 4.1 presents the peak positions (RA and Dec), the peak and integrated flux densities for each detected continuum object. MM1 is the only resolved core with a root-mean-square (rms) noise of 0.74 mJy beam^{-1}. MM2 is marginally resolved with an angular size of $6''.41 \times 2''.29$. MM2 and MM3 are located $\leq 16''$ and $\leq 27''$, south-west of MM1 respectively. MM4, MM5 and MM7 are $\leq 5''$, $\leq 8''$ and $\leq 25''$, south of MM1 respectively while MM6 is located just west of MM1. The periodic methanol masers are associated with MM1 (circle in Figure 4.1) and using the methanol multi-beam (MMB) survey maser positions (Breen et al., 2015), the masers are located $\sim 0''.2$ from the peak continuum emission of MM1. The star symbols indicate the near-infrared (NIR) counterparts, that were obtained from the database of the UKIRT Infrared Deep Sky Survey (UKIDSS).

Assuming that the dust emission is optically thin and using the integrated flux density $S_\nu = 10.7$ mJy in Table 4.1 along with the distance $D = 4.86$ kpc (Reid et al., 2009) at which G22.357+0.066 is located, as given in Chapter 1, then Equation 2.93 in Chapter 2 gives the mass of the

dust, M_d, of G22.357+0.066 - MM1. The value $\kappa_\nu = 0.19$ cm^2 g^{-1} is used as given in Chapter 2 and a gas to dust mass ratio of 100 is assumed to obtain the molecular gas mass. Liu et al. (2017) classified G9.62+0.19E as a hot core due to the hot CH_3OH emission they detected and since hot cores have gas temperature exceeding 100 K (Beuther, 2007), a dust temperature of 100 K was used for all three target sources. The main uncertainty regarding this estimate for the mass of all three sources comes from the assumed T_d. The mass of G22.357+0.066 - MM1 was estimated to be ~ 4 M$_\odot$.

TABLE 4.1: Continuum position parameters.

Object-name	R.A. (h m s)	Dec. (° ′ ″)	Peak flux (mJy beam^{-1})	Integrated flux (mJy)
G22.357+0.066 - MM1	18 31 44.1	-09 22 12.2	11.6	10.6
G22.357+0.066 - MM2	18 31 43.2	-09 22 25.5	3.3	4.2
G22.357+0.066 - MM3	18 31 43.7	-09 22 37.8	3.1	4.9
G22.357+0.066 - MM4	18 31 44.2	-09 22 16.3	1.0	1.4
G22.357+0.066 - MM5	18 31 44.2	-09 22 19.7	3.0	5.5
G22.357+0.066 - MM6	18 31 43.5	-09 22 11.1	2.5	3.9
G22.357+0.066 - MM7	18 31 44.2	-09 22 36.8	2.6	2.4
G25.441+0.105	18 37 17.0	-06 38 30.3	7.6	9.9
G9.62+0.19E (MM4)	18 06 14.7	-20 31 31.6	119.1	136.5

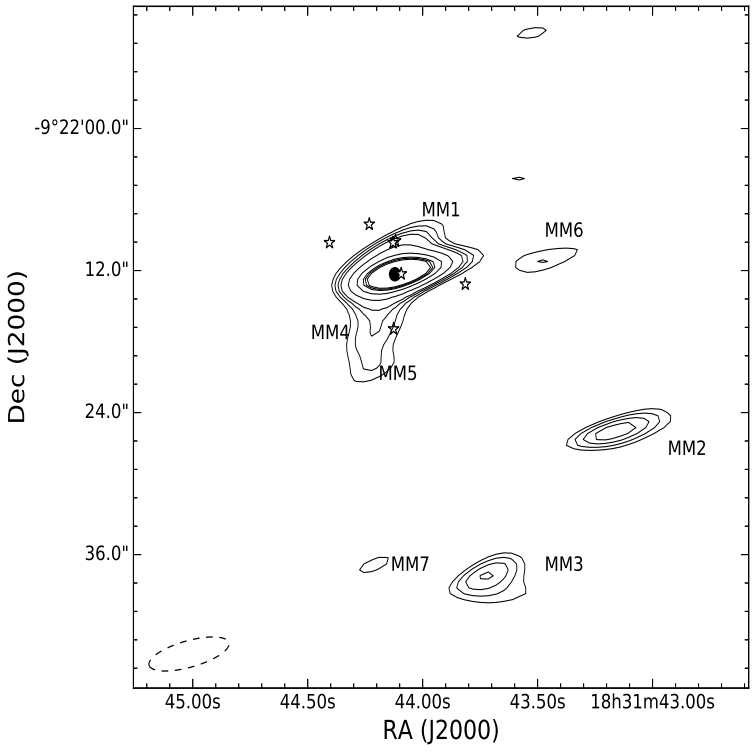

FIGURE 4.1: G22.357+0.066: 1.3 mm continuum emission with the NIR counterparts (star symbol) obtained from UKIDSS Consortium (2012) within a radius of 5 ″ from the maser. MM1 to MM7 indicates each millimetre object detected in the SMA observation. The circle shows the position of the periodic methanol maser.

4.2.1.2 Carbon-monoxide (CO) emission

Three molecular lines, ^{12}CO (2-1), ^{13}CO (2-1) and C^{18}O (2-1), were detected in G22.357+0.066. Figure 4.22 presents the velocity channel maps from 81.6 km s^{-1} to 91.2 km s^{-1} for ^{12}CO. Figure 4.23 presents the ^{13}CO velocity channel maps from 81.6 km s^{-1} to 87.6 km s^{-1} and Figure 4.24 is the velocity channel maps from 81.6 km s^{-1} to 87.6 km s^{-1} for C^{18}O. The dust continuum (white contours) and the NIR counterparts are superimposed on all the channel maps. The position of the periodic 6.7 GHz methanol maser is indicated by a circle. The systemic velocity for G22.357+0.066 is 84.2 km s^{-1} as presented in Table 1.1 Chapter 1. Thus, the emission in channels with velocities smaller than 84.2 km s^{-1} are blue-shifted and channels with velocities greater than 84.2 km s^{-1} are red-shifted.

The most distinctive feature of the CO emission in all three detected CO lines is the clockwise shift in emission around the dust continuum of MM1 in the successive channels. In all three lines the emission first appears south-east of the dust continuum (MM1) at 81.6 km s^{-1}. The C^{18}O at 81.6 km s^{-1} is very faint, but still visible. The ^{12}CO, ^{13}CO and C^{18}O emission in the channel maps all move north as the velocity increases. The emission north of MM1 for the ^{12}CO is observed at 87.6 km s^{-1} and for the ^{13}CO at 85.2 km s^{-1}. For C^{18}O the emission observed north of the dust continuum is at 84.0 km s^{-1}. Unlike the ^{12}CO and ^{13}CO emission, the position of the emission for C^{18}O stays north of the dust continuum for the successive channels. In these channels (Figure 4.24) the intensity decreases until it fades out at 87.6 km s^{-1}. For ^{12}CO and ^{13}CO the emission moves north-west. After 86.4 km s^{-1} in the ^{12}CO channel maps (Figure 4.22), the emission decreases and for the ^{13}CO emission (Figure 4.23), the last velocity channel to contain any emission is at 87.6 km s^{-1}.

Blue-shifted emission is seen south-east of MM1 at 81.6 km s^{-1} for ^{12}CO and ^{13}CO. The red-shifted emission is seen north-west of MM1 at 87.6 km s^{-1} and 88.8 km s^{-1} for ^{12}CO and at 87.6 km s^{-1} for ^{13}CO. This almost symmetric distribution of emission (south-east - north-west), with regards to the dust continuum-MM1, as seen in Figures 4.22 and 4.23, have been interpreted to be tracing a bipolar outflow and will be discussed in section 4.2.5.

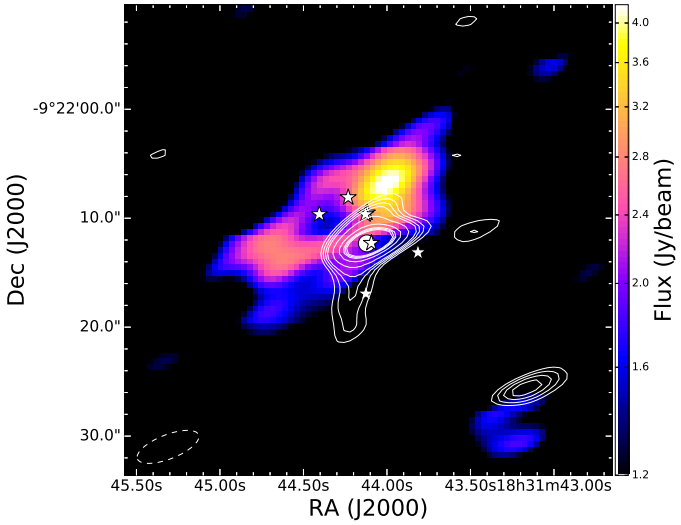

FIGURE 4.2: G22.357+0.066: integrated intensity map from 81.6 km s^{-1} to 87.6 km s^{-1} for ^{13}CO with the NIR counterparts (star symbol) from UKIDSS. The circle shows the position of the periodic methanol maser.

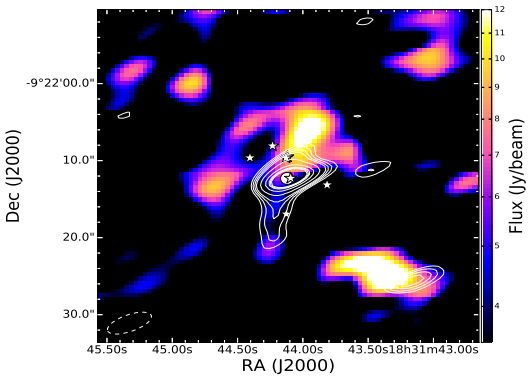

FIGURE 4.3: G22.357+0.066: integrated intensity map from 81.6 km s^{-1} to 91.2 km s^{-1} for ^{12}CO with the NIR counterparts (star symbol) from UKIDSS. The circle shows the position of the periodic methanol maser.

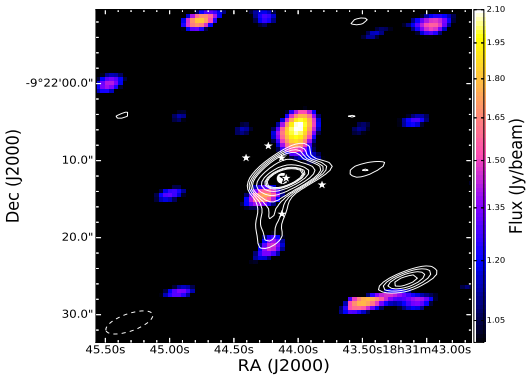

FIGURE 4.4: G22.357+0.066: integrated intensity map from 81.6 km s^{-1} to 87.6 km s^{-1} for C^{18}O with the NIR counterparts (star symbol) from UKIDSS. The circle shows the position of the periodic methanol maser.

Figures 4.2, 4.3 and 4.4 present the integrated intensity maps of ^{13}CO, ^{12}CO and C^{18}O respectively. Most of the CO emission in the integrated intensity maps do not seem to be associated with MM1. The ^{13}CO and ^{12}CO integrated intensity maps show strong emission north-west and south-east of MM1, especially the northern emission is quite intense with a flux density of 0.14 Jy compared to the south-eastern emission that has a flux density of 0.07 Jy which is half of the northern emission in intensity for the ^{13}CO. The C^{18}O integrated intensity map also shows strong emission north of MM1.

All three integrated intensity maps show CO emission that appear to be associated with MM2, especially the ^{12}CO emission is quite strong at MM2 $\sim$ 0.8 Jy whereas the flux density for the ^{13}CO at MM2 is $\sim$ 0.07 Jy. The ^{12}CO (Figure 4.3) and C^{18}O (Figure 4.4), show weak emission that could be associated with MM4 and MM5.

Figure 4.5 presents the line spectra of G22.357+0.066. The integrated intensity maps were used to define the areas over which the line spectra were taken. The black spectrum in Figure 4.5 is the 6.7 GHz periodic methanol maser spectrum of G22.357+0.066 (Szymczak et al., 2015). A Gaussian fit was done on all three line spectra using only the four or five highest flux density points. The peak positions of the line spectra are 85.9 km s^{-1} for ^{12}CO, 85.1 km s^{-1} for ^{13}C and 84.5 km s^{-1} for C^{18}O. The systemic velocity is also indicated in Figure 4.5 at 84.2 km s^{-1}.

The flux density of the 6.7 GHz periodic methanol maser spectrum is in Jy whereas the CO line spectra are in Jy beam^{-1}. The maser spectrum was also divided by a constant to fit the graph. The maser spectrum has three large features at, 79.52 km s^{-1}, 80.09 km s^{-1} and 81.45 km s^{-1} (Szymczak et al., 2007).

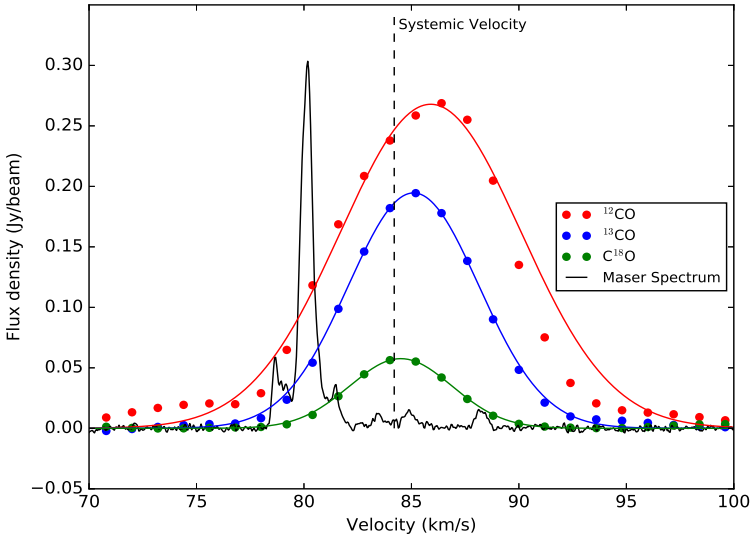

FIGURE 4.5: G22.357+0.066: CO line spectra with Gaussian fits. The ^{12}CO is indicated in red, the ^{13}CO in blue and C^{18}O is indicated in green. The line through each CO spectrum represents the Gaussian fit done on each spectrum. The 6.7 GHz periodic methanol maser spectrum is indicated in black.

4.2.1.3 CO emission morphology

When comparing the velocity channel maps with the integrated intensity maps, in the case of ^{12}CO and ^{13}CO, the north-west (red-shifted) and south-east (blue-shifted) emission seen in the ^{13}CO (Figure 4.2) and ^{12}CO (Figure 4.3) integrated intensity maps are to be expected from the shift in emission seen in the ^{12}CO (Figure 4.22) and ^{13}CO (Figure 4.23) velocity channel maps, which contain strong emission south-east and north-west of MM1. The north-west emission is brighter in intensity than the south-east emission in the integrated intensity maps of ^{13}CO and ^{12}CO. The difference in the intensity brightness in the ^{12}CO integrated intensity map is because more channels in the ^{12}CO channel maps contain red-shifted emission than channels containing blue-shifted emission. For the ^{13}CO, there are three channels that contribute to the red-shifted emission and only two channels that contribute to the blue-shifted emission since the emission at 81.6 km s^{-1} is more south and does not really contribute to the blue-shifted emission. The same symmetry (south-east - north-west) with regards to the dust continuum is seen in both the ^{13}CO and ^{12}CO integrated intensity maps and the ^{12}CO and ^{13}CO channels maps. This blue-shifted and red-shifted emission was interpreted to be tracing a bipolar outflow as discussed in section 4.2.5.

The C^{18}O integrated intensity map (Figure 4.4) has a bright northern emission core that the velocities 84.0 km s^{-1}, 85.2 km s^{-1} and 86.4 km s^{-1}, in the channel maps (Figure 4.24), contribute too. The C^{18}O integrated intensity map also has a fainter emission core south-east of the dust continuum and a very faint core south of the continuum that is associated with MM4 and MM5 respectively. The velocity channels of 81.6 km s^{-1} and 82.8 km s^{-1} contribute to the two fainter cores. The ^{12}CO (Figure 4.3) integrated intensity map also contains faint emission associated with MM5. However, the ^{12}CO (Figure 4.3) channel maps do not contain any visible emission that can be associated with MM5.

The only emission that was not expected in the integrated intensity maps, is the emission associated with MM2. The ^{12}CO integrated intensity map contains a bright emission associated with MM2. The integrated intensity maps of ^{13}CO and C^{18}O also contain CO emission at MM2, but not as intense as the emission seen in the ^{12}CO integrated intensity map. Velocity channels at 87.6 km s^{-1} and 88.8 km s^{-1} in the ^{12}CO and velocity channel 82.8 km s^{-1} in the ^{13}CO as well as velocity channel 85.2 km s^{-1} in the C^{18}O, contain very faint emission that could be associated with MM2. However none of the ^{12}CO, ^{13}CO or C^{18}O channel maps contain clearly visible emission associated with MM2 that could explain the bright emission seen in the integrated intensity maps.

4.2.2 G25.411+0.105

4.2.2.1 1.3 mm continuum emission

Figure 4.6 shows a single millimetre continuum object detected in the SMA observations of G25.411+0.105. The core has a peak flux of 7.75 mJy beam^{-1} and an integrated flux of 9.86 mJy, with an rms noise level of 0.73 mJy beam^{-1}. The remaining continuum parameters are summarized in Table 4.1. The periodic 6.7 GHz methanol masers are projected on the dust continuum. Making use of the MMB survey maser positions (Breen et al., 2015), the masers are located $\sim 0''.22$ from the peak continuum emission of G25.411+0.105. The methanol maser is marked with a circle and the star symbols indicate the NIR counterparts, obtained from the database of the UKIRT Infrared Deep Sky Survey (UKIDSS).

The mass estimate for G25.411+0.105 was calculated in the same way as the mass estimate for G22.357+0.066. The integrated flux density, $S_\nu = 9.9$ mJy, was obtained from Table 4.1 and the distance $D = 9.50$ kpc was used as given in Chapter 1. The mass of G25.411+0.105 was estimated to be ~ 14 M$_\odot$.

4.2.2.2 Carbon-monoxide (CO) emission

Three molecular lines, ^{12}CO (2-1), ^{13}CO (2-1) and C^{18}O (2-1) were detected towards G25.411+0.105. Figure 4.25 shows the velocity channel maps from 91.6 km s^{-1} to 104.8 km s^{-1} for ^{12}CO, Figure 4.26 shows the ^{13}CO velocity channel maps from 90.4 km s^{-1} to 100.0 km s^{-1} and Figure 4.27 shows the velocity channel maps of C^{18}O from 94.0 km s^{-1} to 97.6 km s^{-1}. The dust continuum (white contours) and the NIR counterparts are superimposed on all the channel maps. The position of the periodic 6.7 GHz methanol maser is indicated by a circle. The systemic velocity of G25.411+0.105 is at 96.0 km s^{-1} as given in Table1.1 in Chapter 1. Thus emission at velocities greater than 96.0 km s^{-1} are red-shifted and velocities smaller than 96.0 km s^{-1} are blue-shifted.

The emission in the ^{12}CO velocity channel maps (Figure 4.25) first appears at 91.6 km s^{-1} north-west of the dust continuum and becomes stronger at 92.8 km s^{-1}. At 94.0 km s^{-1} and 95.2 km s^{-1} no emission is seen in the ^{12}CO. From 96.4 km s^{-1} to 104.8 km s^{-1} most of the emission is projected onto the dust continuum. At 97.6 km s^{-1} the emission north-west of the dust continuum observed in the blue-shifted channels (91.6 km s^{-1} and 92.8 km s^{-1}) re-appears and for velocities 97.6 km s^{-1} to 102.4 km s^{-1} it seems that the ^{12}CO has two cores. A fainter emission core is also found from 97.6 km s^{-1} to 100.0 km s^{-1}, south-east of the dust continuum.

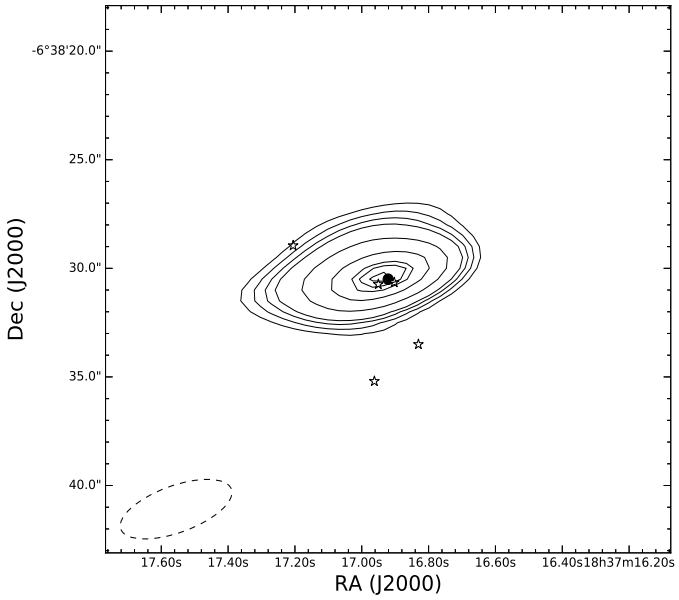

FIGURE 4.6: G25.411+0.105: 1.3 mm continuum emission with the NIR counterparts (star symbol) obtained from UKIDSS Consortium (2012) within a radius of 5 $''$ from the maser. The circle shows the position of the periodic 6.7 GHz methanol maser.

The emission in the ^{13}CO velocity channel maps (Figure 4.26) is mostly located on the dust continuum. Faint emission first appears at 90.4 km s^{-1} on the continuum, but shifts south-east in the next channel. At 92.8 km s^{-1} the emission is clearly visible north-west and south-east of the dust continuum. As also seen in the ^{12}CO channel map, the emission at 94.0 km s^{-1} and 95.2 km s^{-1} decreases significantly, especially at 94.0 km s^{-1} where the emission almost vanishes completely in the ^{13}CO. Bright emission appears at 96.4 km s^{-1} on the dust continuum and gradually decreases in intensity in the successive channels $\sim$ 96.4 km s^{-1} to 100.0 km s^{-1}. For the velocities 97.6 km s^{-1} to 100.0 km s^{-1}, two cores north-west and south-east of the dust continuum are seen. This emission north-west and south-east of the dust continuum is also seen in the ^{12}CO channel maps.

The C^{18}O velocity channel maps (Figure 4.27) also show emission that is mostly located on the dust continuum. For the C^{18}O only four channels, 94.0 km s^{-1} to 97.2 km s^{-1}, contain emission. A strong C^{18}O condensation is seen south - south-west of the dust continuum and is clearly visible at 95.2 km s^{-1}. Velocities 94.0 km s^{-1} and 96.4 km s^{-1} also show the C^{18}O condensation, although the emission is weaker. This reconfirms that the emission seen is not an artefact or the effect of the beam sidelobes. At 96.4 km s^{-1} there is also emission north-east of the dust continuum. However the emission is only seen in this channel, the ^{12}CO and ^{13}CO channel maps also do not contain any emission located north-east of the dust continuum.

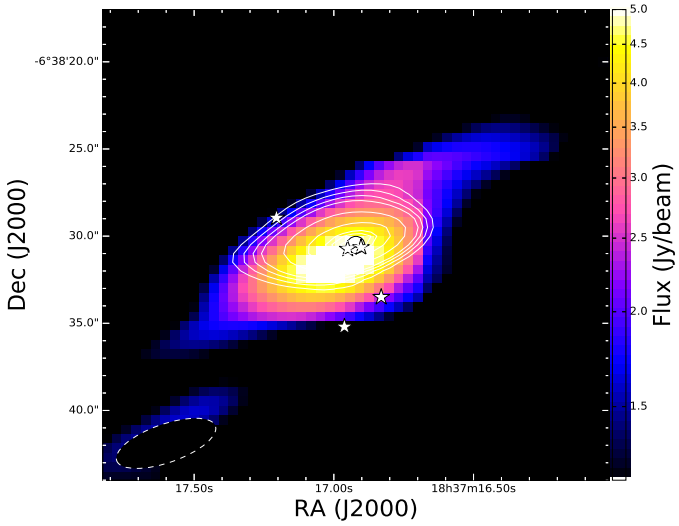

FIGURE 4.7: G25.411+0.105: integrated intensity map of ^{13}CO from 90.4 km s^{-1} to 100.0 km s^{-1}. The NIR counterparts (star symbol) are from UKIDSS. The circle shows the position of the periodic methanol maser.

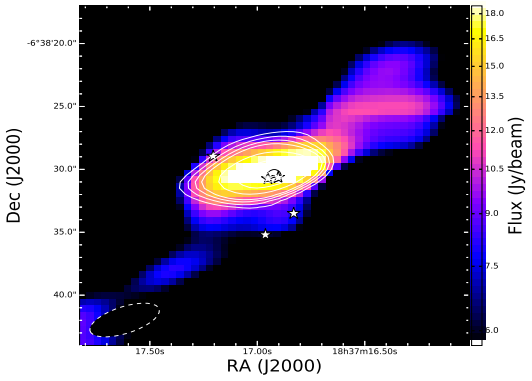

FIGURE 4.8: G25.411+0.105: integrated intensity map of ^{12}CO form 91.6 km s^{-1} to 104.8 km s^{-1}. The NIR counterparts (star symbol) are from UKIDSS. The circle shows the position of the periodic methanol maser.

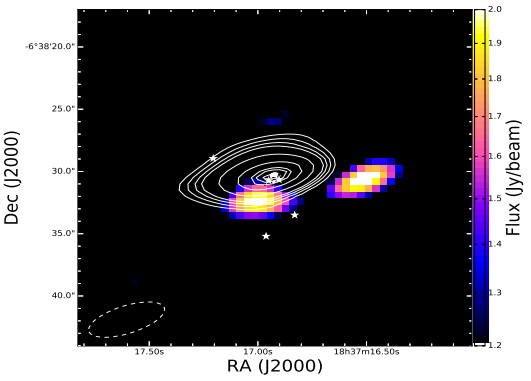

FIGURE 4.9: G25.411+0.105: integrated intensity map of C^{18}O form 90.4 km s^{-1} to 97.6 km s^{-1}. The NIR counterparts (star symbol) are from UKIDSS. The circle shows the position of the periodic methanol maser.

Figures 4.7, 4.8 and 4.9 present the integrated intensity maps of ^{13}CO, ^{12}CO and C^{18}O respectively. The majority of the CO emission is in a compact morphology projected on the dust continuum. The ^{12}CO integrated intensity map shows CO emission north-west of the dust continuum. The ^{13}CO map also suggests CO emission in that direction. Very faint emission is visible south-east of the continuum in the ^{13}CO and ^{12}CO integrated intensity maps. The integrated intensity map of C^{18}O shows two emission cores, one that is located on the dust continuum and the other located east of the dust continuum.

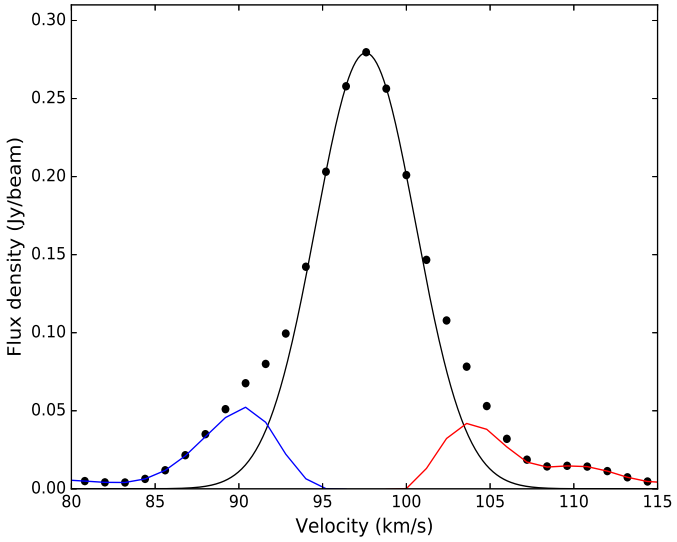

FIGURE 4.10: G25.411+0.105: ^{13}CO line spectrum with the Gaussian fit. The line through the spectrum represents the Gaussian fit. The blue and red lines indicate the blue-shifted and red-shifted emission

Figure 4.10 presents the ^{13}CO line spectrum. The ^{13}CO spectrum shows 'wing' channels and was fitted with a Gaussian fit. The Gaussian fit as well as the blue-shifted (85.0 km s^{-1} $\sim$ 95.0 km s^{-1}) and red-shifted (100.0 km s^{-1} $\sim$ 107.0 km s^{-1}) components are indicated on the spectrum. The Gaussian peak is at 97.58 km s^{-1}. Szymczak et al. (2007) also found 'wings' in the ^{13}CO spectrum of G25.411+0.105 and they estimated a velocity range of 11 km s^{-1} for the ^{13}CO wings. The wing channels were extracted as emission associated with out-flowing gas and will be discussed in section 4.2.5.

Figure 4.11 presents the line spectra of the ^{12}CO (red spectrum) and C^{18}O (green spectrum) in G25.411+0.105. The integrated intensity maps were used to define the areas over which the line spectra were taken. The black spectrum shown in Figure 4.11 is the 6.7 GHz periodic methanol maser (Szymczak et al., 2015). A Gaussian fit was done on the C^{18}O line spectrum. The peak position of the C^{18}O is at 95.9 km s^{-1}. The systemic velocity is also indicated in Figure 4.11 at 96.0 km s^{-1}. The ^{12}CO line spectrum without a Gaussian fit is shown in Figure 4.11. The line spectrum of ^{12}CO has a double peak profile, with an absorption at 94.0 km s^{-1}. The double peaks are located at 91.6 km s^{-1} and 100.0 km s^{-1}. The flux density of the 6.7 GHz periodic methanol maser spectrum is in Jy whereas the CO line spectra are in Jy beam^{-1}. The maser spectrum was also divided by a constant to fit the graph. The maser spectrum has two large features, 94.78 km s^{-1} that is the blue-shifted emission and 97.78 km s^{-1} that is red shifted emission (Szymczak et al., 2015).

Since the ^{12}CO line spectrum contains a double peak profile, there are two possibilities to explain the observed profile. The first possibility is that the ^{12}CO has a P Cygni profile, presented in Figure 4.12, and the second possibility is that the ^{12}CO contains two cores, presented in Figure 4.13. Thus to investigated the two possibilities the ^{12}CO spectrum was taken at different locations of the ^{12}CO emission, using the ^{12}CO integrated intensity map (Figure 4.8) to define the two areas.

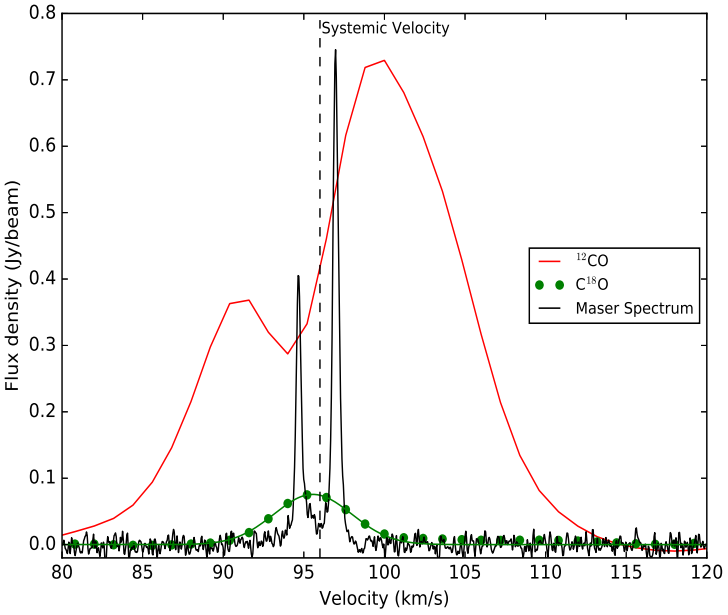

FIGURE 4.11: G25.411+0.105:CO line spectra. The ^{12}CO is indicated in red with a peak position at 100.0 km s^{-1} and the C^{18}O is indicated in green with a peak position at 95.9 km s^{-1}. The line through the C^{18}O spectrum represents the Gaussian fit. The 6.7 GHz periodic methanol maser spectrum is indicated in black.

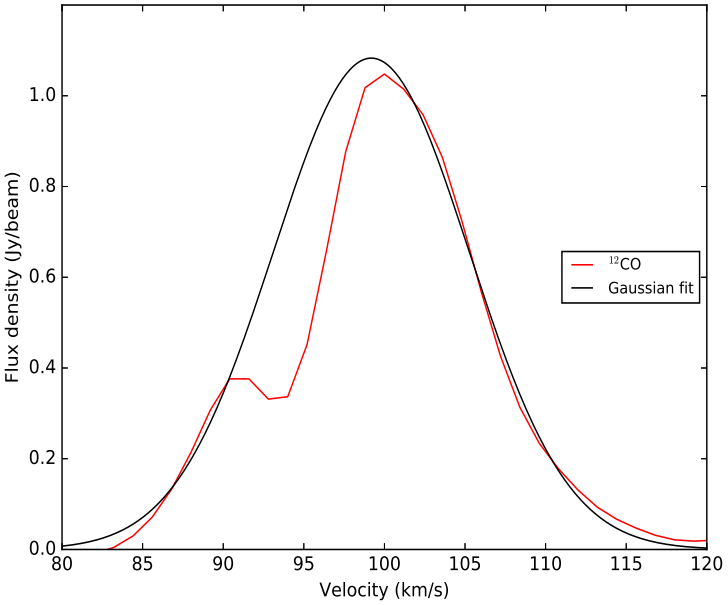

FIGURE 4.12: G25.411+0.105: ^{12}CO line spectrum with a P Cygni profile. The red spectrum is the ^{12}CO line spectrum and the black spectrum is the Gaussian fit.

For Figure 4.12 the ^{12}CO spectrum was taken over the continuum part of the ^{12}CO emission in the ^{12}CO integrated intensity map. A single Gaussian was fitted over both peaks, showing a P Cygni profile. The absorption is at 94.0 km s^{-1}, which is on the blue-shifted side of the spectrum and is then followed by the large emission peak on the red-shifted side. The absorption at 94.0 km s^{-1} is consistent with what is seen in the ^{12}CO channel maps (Figure 4.26) where at 94.0 km s^{-1} and at 95.2 km s^{-1} no ^{12}CO emission is observed.

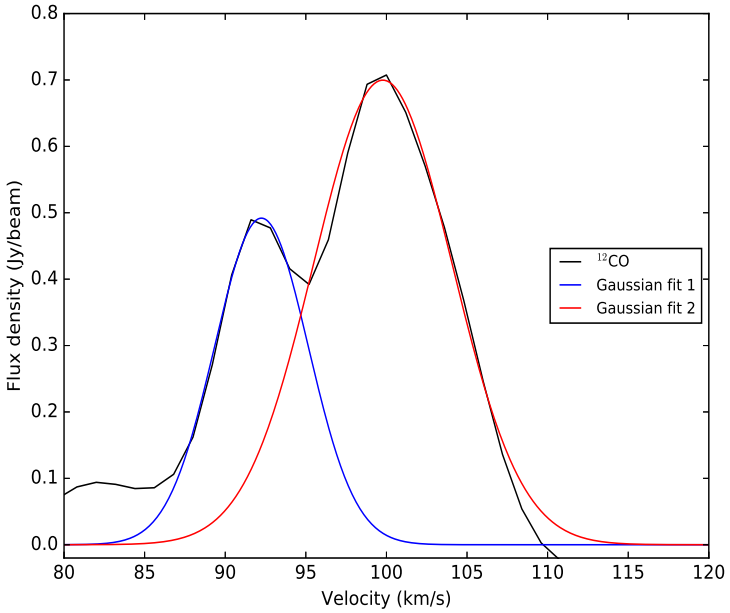

FIGURE 4.13: G25.411+0.105: ^{12}CO line spectrum with Gaussian fits. The black spectrum is the ^{12}CO line spectrum and the blue and red spectra are the Gaussian fits.

For Figure 4.13 the ^{12}CO spectrum was taken over the ^{12}CO emission located north-west of the dust continuum in the ^{12}CO integrated intensity map. The first peak has a higher flux density and the second peak has a smaller flux density with regards to Figure 4.12. Both peaks were fitted with a Gaussian fit. The Gaussian fit for the first peak is in blue and the Gaussian fit for the second peak is in red. To investigate the shape of the ^{12}CO spectrum further, higher resolution observations with better sensitivity is needed.

4.2.2.3 CO emission morphology

Comparing the velocity channel maps and the integrated intensity maps, for ^{13}CO and ^{12}CO the majority of the CO emission is in a compact morphology on the dust continuum which is to be expected considering that most of the CO emission in the channel maps are located on the dust continuum. Although the integrated intensity map of ^{13}CO (Figure 4.7) does show some faint emission north-west and south-east of the dust continuum, the emission does not show the expected intensity from the velocity channels 97.6 km s^{-1} and 98.8 km s^{-1} in the channel maps of ^{13}CO (Figure 4.26). The ^{12}CO integrated intensity map (Figure 4.8) contains two emission cores, one on the dust continuum and one north-west of the dust continuum. This emission north-west of the contiuum is to be expected since most of the ^{12}CO channel maps (Figure 4.25)

contain emission north-west of the dust continuum (channels: 91.6 km s^{-1} to 92.8 km s^{-1} and 97.6 km s^{-1} to 102.4 km s^{-1}). The faint emission south-east of the dust continuum in the ^{12}CO integrated intensity map, originates from channels 97.6 to 100.0 in the ^{12}CO channel maps.

The ^{12}CO velocity channel maps contain no emission at 94.0 km s^{-1} and 95.2 km s^{-1}. This corresponds to the absorption seen in the ^{12}CO line spectrum (Figure 4.11) which is also at 94.0 km s^{-1}. The ^{13}CO velocity channel maps also contain very little emission at 94.0 km s^{-1} and 95.2 km s^{-1}.

The integrated intensity map of C^{18}O (Figure 4.9) shows two emission cores, that is some what unexpected when taking into consideration the velocity channel maps of C^{18}O (Figure 4.27). The cores in the integrated intensity maps are located south and west of the dust continuum. The emission of the southern core in the integrated intensity map could be from channels 94.0 km s^{-1} and 96.4 km s^{-1}. However, some emission is expected to be located in the center of the dust continuum in the integrated intensity map, considering channels 94.0 km s^{-1} to 96.4 km s^{-1} in the C^{18}O channel maps. Channels 94.0 km s^{-1} and 95.2 km s^{-1} could contribute to the western emission core, however the channel maps do not contain the bright emission expected to contribute to the western core in the integrated intensity map. Considering the bright south - south-west emission in the C^{18}O channel maps, the expectancy would be to see some of this emission in the C^{18}O integrated intensity map which does not contain any emission at that location. The integrated intensity map also does not contain any of the emission seen north-east at 96.4 km s^{-1} in the channel maps.

4.2.3 G9.62+0.19E

4.2.3.1 1.3 mm continuum emission

Liu et al. (2017) reported twelve millimetre continuum objects (MM1 to MM12) associated with G9.62+0.19. The focus here will be the MM4 core (G9.62+0.19E), located at $(\alpha, \delta)_{J2000} = (18^h06^m14^s.658, -20°31'31''.570)$, that the 6.7 GHz methanol maser is associated with. Figure 4.14 presents the millimetre continuum emission of G9.62+0.19E. The methanol maser is marked with a circle and the star symbol indicates the NIR counterpart obtained from the database of the UKIRT Infrared Deep Sky Survey (UKIDSS). Testi et al. (2000) reported centimetre and millimetre dust continuum towards G9.62+0.19.

For component E of G9.62+0.19, Liu et al. (2017) found the peak intensity of the Gaussian component of the dust emission to be 0.26±0.01 mJy beam^{-1} and the peak intensity for the residual point-like component was found to be 0.93±0.03 mJy. They also calculated the mass by assuming a dust temperature of 100 K and using a density of (4.2 ± 1.3)×10^6 cm^{-3}. The mass of G9.62+0.19E was estimated to be 74.0±23.4 M$_\odot$. Liu et al. (2017) also derived a effective diameter of 1$''$.65 for the dust continuum of G9.62+0.19E and using a distance of 5.2 kpc (Sanna et al., 2009), the radius would correspond to approximately 8600 AU.

Table 4.1 presents the peak position (RA and Dec), the peak and integrated intensity of the emission for MM4. A mass estimate was done for G9.62+0.19E using Equation 2.93. The mass estimate was done similar to the mass estimates for the previous two sources. An integrated flux density of 136.5 mJy, obtained from Table 4.1, and a distance of 5.2 kpc were used to calculate the dust mass. The value for κ_ν is 0.19 cm^2 g^{-1} and a dust temperature of 100 K

was used, as given by Liu et al. (2017). The mass of G9.62+0.19E was estimated to be 58 $M_{\odot}$.

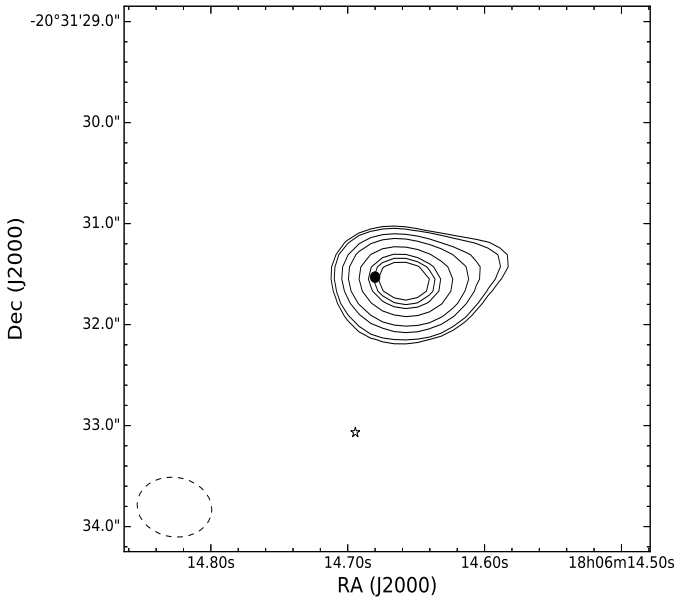

FIGURE 4.14: G9.62+0.19E: 1.3 mm continuum emission with the NIR counterpart (star symbol) obtained from UKIDSS Consortium (2012) within a radius of 2 $''$ from the maser. The circle shows the position of the periodic 6.7 GHz methanol maser. The synthesised beam is shown in the left bottom as an ellipse.

4.2.3.2 Carbon-monoxide (CO) emission

Unlike the SMA data, which covers three CO isotopes, the ALMA archival data of G9.62+0.19E covered only the ^{12}CO(2-1) transition. Figure 4.15 is the ^{12}CO line spectrum. The dust continuum (MM4) was used to define the area over which the line spectrum was taken. A Gaussian fit was not suitable for the spectrum since the line profile has a P Cygni profile. The systemic velocity is also indicated in Figure 4.15 at $\sim$ 2.0 km s^{-1}. The black spectrum is the the 6.7 GHz periodic methanol maser. The flux density of the 6.7 GHz periodic methanol maser spectrum is in Jy where as the ^{12}CO line spectrum is in Jy beam^{-1}. The maser spectrum was also divided by a constant to fit the graph. The periodic maser has major features at -1.0 km s^{-1}, 0.0 km s^{-1}, 1.2 km s^{-1}, 3.1 km s^{-1} and 3.8 km s^{-1} (Goedhart et al., 2003).

The classic P Cygni profile contains the absorption on the blue-shifted side of the spectrum and is followed by an emission peak, but in the case of G9.62+0.19E the ^{12}CO spectrum contains two absorptions, one that is blue-shifted and one that is red-shifted, as indicated on the spectrum. The absorption is followed by the smaller red-shifted emission peak. The larger emission peak is blue-shifted and followed by the larger absorption. The blue-shifted (-2.7 km s^{-1} to 1.0 km s^{-1}) and red-shifted (8.0 km s^{-1} to 10.7 km s^{-1}) emission peaks presented in the ^{12}CO line spectrum suggest that there is outflow present in G9.62+0.19E, which will be discussed in section 4.2.5.

The systemic velocity of G9.62+0.19E is given by Table 1.1 in Chapter 1 as 2.1 km s^{-1}, thus emission at velocities smaller than 2.1 km s^{-1} are blue-shifted and emission at velocities greater

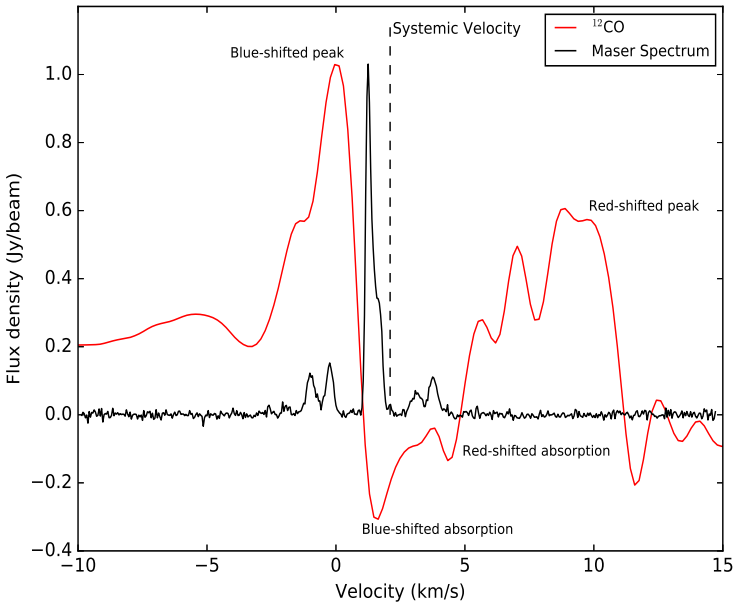

FIGURE 4.15: G9.62+0.19E: ^{12}CO line spectrum that is indicated in red and in black is the 6.7 GHz periodic methanol maser spectrum.

than 2.1 km s^{-1} are red-shifted. Since the ^{12}CO emission stretches over a large number of channels, the blue-shifted and red-shifted emission peaks in Figure 4.15 were used to obtain the velocity ranges over which to image the velocity channel maps. Figures 4.28 and 4.29 present the blue- and red-shifted velocity channel maps for ^{12}CO. The blue-shifted channel maps are from -2.7 km s^{-1} to 1.0 km s^{-1} and the red-shifted channel maps are from 8.0 km s^{-1} to 10.7 km s^{-1}. Originally there were 42 velocity channel maps, but to create Figures 4.28 and 4.29 two successive channels were added to obtain the 12 blue-shifted channel maps and the 9 red-shifted channel maps with a channel width of $\sim$ 0.33 km s^{-1}. The velocity channels from 1.3 km s^{-1} to 7.7 km s^{-1} contained very little to no emission. The dust continuum (white contours) and the NIR counterpart are superimposed on all the channels maps and the position of the periodic 6.7 GHz methanol maser is indicated by a circle.

The emission first appears at -2.7 km s^{-1} north-west of the dust continuum in Figure 4.28 and increases in intensity in the successive channels up until -1.1 km s^{-1}. At -0.7 km s^{-1} bright emission is seen north-west of the dust continuum and weak emission is present on the dust continuum. The emission north-west and on the dust continuum become brighter in intensity in the next two channels. However the emission on the dust continuum shows expansion to the south-east. At 0.3 km s^{-1} the north-west emission has decreased in intensity, but the emission south-east and on the dust continuum increased in intensity. Channel 0.6 km s^{-1} is the last to contain blue-shifted emission. The only emission present at 0.6 km s^{-1} is the south-eastern emission.

At 8.0 km s^{-1} the red-shifted emission appears north-west and south-east of the dust continuum in Figure 4.29, although it is very faint. At 8.4 km s^{-1} the emission significantly increases in intensity. However the south-eastern emission is brighter in intensity than the north-western emission. From 8.7 km s^{-1} to 10.1 km s^{-1} the north-western emission increases in intensity, while the south-eastern emission decreases significantly from channel 8.7 km s^{-1}. The last

south-eastern emission is visible at 9.7 km s^{-1}. At 10.4 km s^{-1} the north-western emission decreases in intensity and faint emission is seen at 10.7 km s^{-1}.

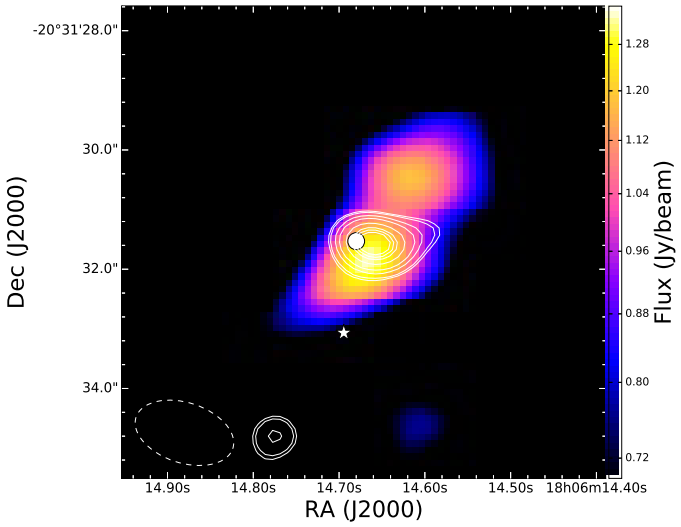

FIGURE 4.16: G9.62+0.19E: integrated intensity map from -2.7 km s^{-1} to 10.7 km s^{-1} for ^{12}CO with the NIR counterpart (star symbol) from UKIDSS. The circle shows the position of the periodic methanol maser.

Figure 4.16 presents the integrated intensity map of ^{12}CO. The integrated intensity map shows two cores of emission, one bright core north-west of the dust continuum and one fainter core south-east of the dust continuum. Both cores have a part of their emission that is on the dust continuum. The north-western emission has a flux density of 2.8 Jy and the south-eastern emission has a flux density of 0.7 Jy.

4.2.3.3 CO emission morphology

The channel maps were imaged using only the velocity ranges of the blue-shifted and red-shifted peak emission in the ^{12}CO spectrum (Figure 4.15). The velocity range were the absorption is seen in the ^{12}CO spectrum contains no emission as channel 1.0 km s^{-1} demonstrates and therefore these channel were not imaged.

Comparing the blue-shifted (Figure 4.28) and red-shifted (Figure 4.29) emission, a north-west - south-east symmetry with regards to the dust continuum is seen. This symmetry is also seen in the intensity integrated map (Figure 4.16). The north-western core in the intensity integrated map is brighter than the south-eastern core, since all of the channel maps, except for channel 0.6 km s^{-1}, contain emission north-west of the dust continuum. Only 10 of the 21 channel maps have emission south-east of the dust continuum at velocities -0.4 km s^{-1} to 0.6 km s^{-1} and 8.0 km s^{-1} to 9.7 km s^{-1}, therefore the south-eastern core in the intensity integrated map is fainter. The blue-shifted and red-shifted channel maps for ^{12}CO was interpreted to be tracing multiple outflow system.

At 8.4 km s^{-1} to 9.7 km s^{-1} there is some emission, originating from a different source, that crosses with the emission seen from the south-east (Figure 4.29). For 8.4 km s^{-1} to 9.1 km s^{-1} it is possible to separate the emission south-east of the dust continuum with the emission

originating from a different source. However at 9.4 km s^{-1} and 9.7 km s^{-1} separating these two emissions become difficult, especially at 9.4 km s^{-1} where it seems that the emission originating from the other source expanded into the emission of the south-eastern core.

4.2.3.4 Methanol (CH_3OH) emission

The ALMA archival data also covered the CH_3OH ν_t ($6_{1,5}$-$7_{2,6}$) line. Figure 4.30 presents the CH_3OH velocity channel maps form 0.8 km s^{-1} to 2.7 km s^{-1} with a channel width of $\sim$ 0.2 km s^{-1}. The dust continuum (white contours) and the NIR counterpart are superimposed on all the channels maps. The position of the periodic 6.7 GHz methanol maser is indicated by a circle.

The velocity channel maps of CH_3OH ν_t ($6_{1,5}$-$7_{2,6}$) all show compact emission on the dust continuum. The channel maps in Figure 4.30 do not cover all the CH_3OH ν_t ($6_{1,5}$-$7_{2,6}$) channels. At -1.0 km s^{-1} the first faint CH_3OH is seen and at 5.1 km s^{-1} the last CH_3OH is visible. However the morphology of the CH_3OH ν_t ($6_{1,5}$-$7_{2,6}$) stays the same in all the velocity channel maps.

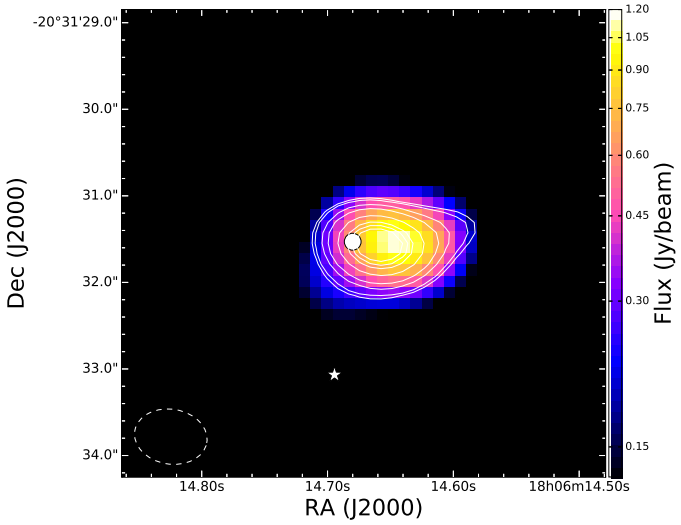

FIGURE 4.17: G9.62+0.19E: integrated intensity map of $CH_3OH\nu_t$ ($6_{1,5}$-$7_{2,6}$) from -1.0 km s^{-1} to 5.1 km s^{-1} with the NIR counterpart (star symbol) from UKIDSS. The circle shows the position of the periodic methanol maser.

Figure 4.17 presents the integrated intensity map of CH_3OH ν_t ($6_{1,5}$-$7_{2,6}$). The CH_3OH ν_t ($6_{1,5}$-$7_{2,6}$) integrated intensity map shows that the emission has a compact morphology on the dust continuum. Considering the velocity channel maps of CH_3OH ν_t ($6_{1,5}$-$7_{2,6}$) (Figure 4.30) this compact morphology of emission, on the dust continuum, seen in the integrated intensity maps is to be expected since all the channel maps have the same disk-like morphology of emission that is located on the dust continuum. Liu et al. (2017) fitted the CH_3OH spectrum with a Gaussian profile and obtained a FWHM of 4.70 $\pm$ 0.02 km s^{-1}. The data was explored further to search for evidence of rotation, which will be discussed in the next section.

4.2.4 Rotating disk-outflow system in G9.62+0.19E

The methanol data was explored further in search for rotation, since it might lead to a better understanding of the disk-outflow system observed in the ^{12}CO velocity channel maps. Figure 4.18 is the velocity field map (moment 1 map) of CH_3OH $v_t = 1$ ($6_{1,5}$-$7_{2,6}$) obtained from Liu et al. (2017) and shows a spatial distinctiveness of the red- and blue-shifted emission, indicating evidence of rotational motion. Liu et al. (2017) also reported these velocity gradients in the methanol moment 1 map that suggests rotation. Liu et al. (2011) also found rotation in the H_2CS ($10_{2,8}$ - $9_{2,7}$).

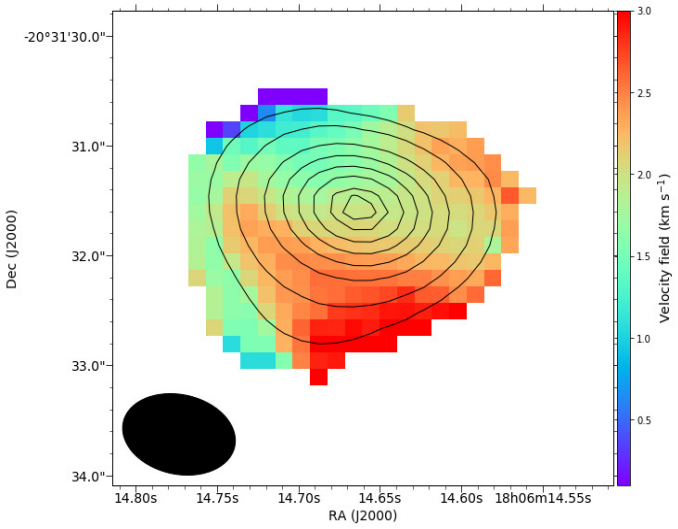

FIGURE 4.18: Moment 1 map of CH_3OH $v_t = 1$ ($6_{1,5}$-$7_{2,6}$) emission of G9.62+0.19E obtained from Liu et al. (2017). The contour levels are 0.5, 1.0, 2.0, 3.0, 4.0, 5.0, 6.0 and 6.5 Jy beam^{-1} of the moment 0 map (Figure 4.17) with a rms level of 0.06 Jy beam^{-1}.

To reconfirm this a CH_3OH $v_t = 1$ ($6_{1,5}$-$7_{2,6}$) line spectrum was extracted over two regions. Region 1 (upper panel) covers a small area around the continuum peak and region 2 (lower panel) is a larger area within the CH_3OH $v_t = 1$ ($6_{1,5}$-$7_{2,6}$) emission. If no rotation was present in the structure traced by CH_3OH $v_t = 1$ ($6_{1,5}$-$7_{2,6}$) emission, then the same Gaussian fit will be suitable for both spectra. Figure 4.19 shows the results of the Gaussian fit to the CH_3OH $v_t = 1$ ($6_{1,5}$-$7_{2,6}$) spectra from the two regions. The excess red- and blue-shifted emission observed in the spectrum of region 2 confirms rotational motion of the structure traced by the CH_3OH $v_t = 1$ ($6_{1,5}$-$7_{2,6}$) emission.

The detection of the CH_3OH $v_t = 1$ ($6_{1,5}$-$7_{2,6}$) line, which has an upper energy level of 374 K, as well as the detection of CH_3OCHO $v_t = 1$ ($17_{4,13}$-$16_{4,12}$) by Liu et al. (2017) towards G9.62+0.19E, suggest that the YSO has heated its surroundings significantly. Since the warm-up phase of a protostar sublimates the ice on the grain mantels and then complex molecules are formed through gas-phase chemistry in the hot-core phase (Herbst & van Dishoeck, 2009), G9.62+0.19E is most probably a hot core as discussed in detail by Liu et al. (2017).

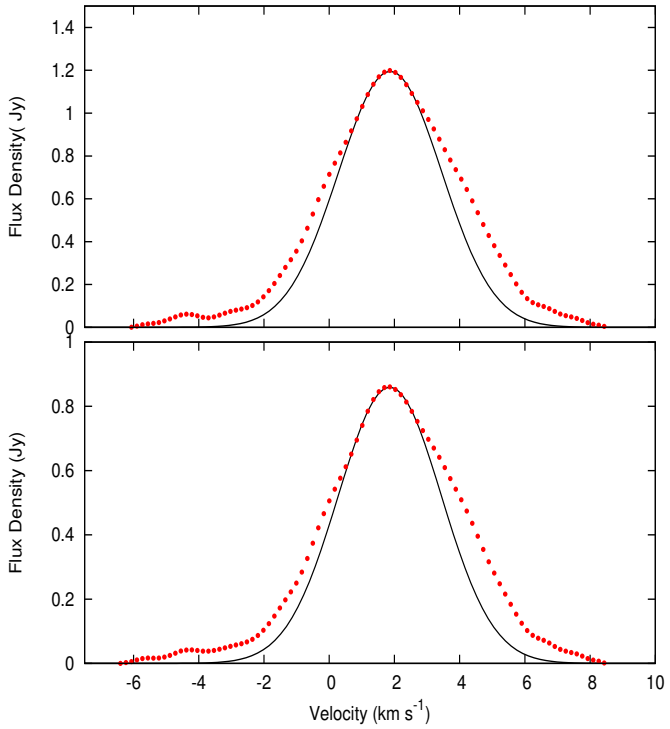

FIGURE 4.19: The CH_3OH $v_t = 1$ ($6_{1,5}$-$7_{2,6}$) emission spectra of G9.62+0.19E. The spectra extracted, is from region 1 (upper panel) which is around the peak of the dust continuum emission and from region 2 (lower panel) that covers a wider area over the distribution of the CH_3OH $v_t = 1$ ($6_{1,5}$-$7_{2,6}$) emission. When fitted with a Gaussian fit, the excess blue- and red-shifted emission can be seen from region 2.

4.2.5 Bipolar outflow

All three target sources, G22.357+0.066, G25.411+0.105 and G9.62+0.19E, show evidence of bipolar outflow from a central core. Figure 4.21 shows the bipolar outflow of G25.411+0.105. The ^{13}CO spectrum (Figure 4.10) showed wing structures and the emission on both sides of the spectrum was extracted from the channel maps in order to obtain Figure 4.21. The red- and blue-shifted components of the outflow are spatially coincident. This indicates that the outflow direction is along the line of sight. Assuming a disk-outflow system, then the rotating structure around G25.411+0.105 must be face-on towards the line of sight of the observer.

The CO emission in G22.357+0.066 is extremely complicated, but channels 81.6 km s^{-1} and 87.6 km s^{-1}, of the ^{12}CO (Figure 4.22) and ^{13}CO (Figure 4.25) emission, indicate bipolarity in their symmetry which cut through the peak position of G22.357+0.066 - MM1. Figure 4.20 shows the bipolar outflow of G22.357+0.066. However, unlike G25.411+0.105 the bipolar structure of the outflows in G22.357+0.066 is not that clear.

The velocity channel maps of G9.62+0.19E (Figures 4.28 and 4.29) show a clear north-west - south-east outflow structure. The bipolar outflow structure has a different orientation as the wings in G25.411+0.105. Since G9.62+0.19E shows a multiple outflow system, it was not possible to extract clear blue- and red-shifted emission as in the case of G22.357+0.066 and G25.411+0.105.

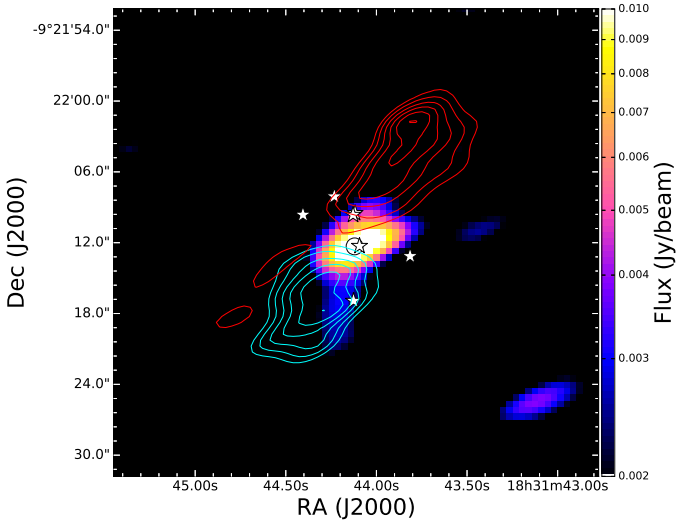

FIGURE 4.20: Bipolar outflow of G22.357+0.066 traced by the ^{13}CO emission. The red contours and blue contours that indicate the blue-shifted and red-shifted emission respectively are superimposed on the dust continuum.

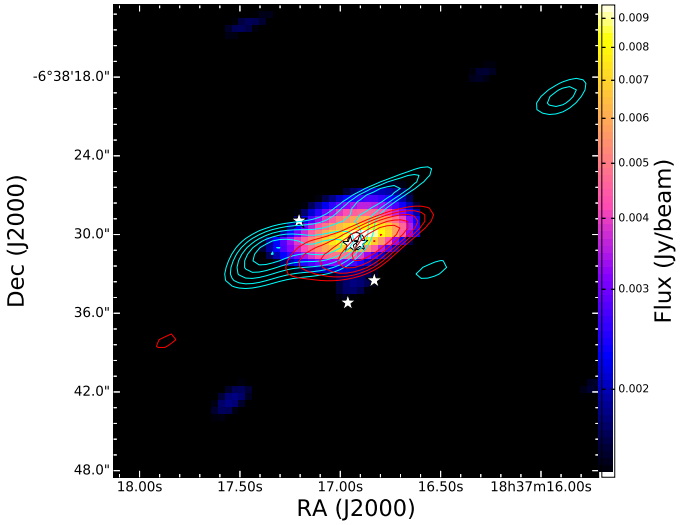

FIGURE 4.21: Bipolar outflow of G25.411+0.105 traced by the ^{13}CO emission. The red contours and blue contours that indicate the blue-shifted and red-shifted emission respectively are superimoped on the dust continuum.

The orientation of the bipolar outflow in G9.62+0.19E and G22.357+0.066 is different in direction from that of G25.411+0.105. The periodic 6.7 GHz methanol masers of G9.62+0.19E and G22.357+ 0.066 have similar light curves. Based on the presence of an H II region in G9.62+0.19E and the non-detection thereof in G22.357+0.066 by (Bartkiewicz et al., 2011), G9.62+0.19E is likely to be more evolved than G22.357+0.066. G25.411+0.105 with a different bipolar outflow orientation also has a different periodic 6.7 GHz methanol maser light curve from that of G9.62+0.19E and G22.357+0.066. This may point to inclination and/or orientation effect as the cause of variation in the periodic methanol maser flare pattern.

4.3 Discussion

4.3.1 Disk-outflow system

From Figure 4.20, it is most likely MM1 that harbours the driving source of the bipolar outflow in G22.357+0.066. MM4 and MM5 are significantly weaker than MM1 implying that their mass also has to be considerably smaller than the mass of MM1. Since MM1 is also located closer to the geometric center of the bipolar outflow, it becomes evident that MM1 has to contain the driving source. For both G25.411+0.105 and G9.62+0.19E, only one dust continuum core was detected for each source. From Figure 4.21 it is seen that the bipolar outflow is situated on the dust continuum of G25.411+0.105 and therefore has to contain the driving source. In the case of G9.62+0.19E it was not possible to extract the bipolar outflow, but the channel maps (Figures 4.28 and 4.29) indicate the existence of a bipolar outflow with MM4 containing the driving source. Figures 4.28 and 4.29 show the presence of a NIR counterpart located $\sim$ 1".5 south of MM4. The complexity of the gas kinematics around MM4 may have been affected by an outflow driven by the NIR counterpart.

In all three sources, evidence of a bipolar outflow was found, which is a fairly common phenomena towards MYSO (Zhang et al., 2001). As earlier discussed in section 4.2.5, the orientation of the bipolar outflow of G9.62+0.19E and G22.357+0.066 are similar to one another, but different from the outflow orientation of G25.411+0.105. G22.357+0.066 and G9.62+0.19E have bipolar outflows which are almost in the plane of the sky and G25.411+0.105 has an outflow that is almost perpendicular to the plane of the sky. The presence of bipolar outflows also imply the existence of disks (Cesaroni et al., 2007). Thus, since the outflows of G9.62+0.19E and G22.357+0.066 are in the plane of the sky, then their disks would be viewed edge-on and in the case of G25.411+0.105 the disk would be viewed face-on since the outflow is perpendicular to the plane of the sky. Considering the velocity field map (Figure 4.18) of G9.62+0.19E, the velocity gradient seen in the CH_3OH $v_t = 1$ ($6_{1,5}$-$7_{2,6}$) also points to a disk with an inclination along the line of sight. Since G25.411+0.105 most likely has a face-on disk, a ring-like spatial distribution for the masers would be expected. This is indeed the case, as (Bartkiewicz et al., 2009) found a ring-like VLBI maser distribution for G25.411+0.105.

As mentioned a few times, the channel maps (Figures 4.28 and 4.29) of G9.62+0.19E show evidence of multiple outflows that made it difficult to obtain a clear positional separation between the blue-shifted and red-shifted emission. One of the possibilities as to why multiple outflows are seen in G9.62+0.19E is that component E contains two sub-components i.e. E1 and E2 (Sanna et al., 2015). E1 is the south-western core and E2 the north-eastern core. Sanna et al. (2015) observed that E1 is significantly stronger than E2 and has an offset of 1300 AU from E2. Thus it might be that the multiple outflows, seen in the channel maps of G9.62+0.19E, originate from both cores, E1 and E2. The other possibility, which was first introduced by Shepherd et al. (2000), is that the outflows might be precessing since there is a slight change in the orientation axis of the bipolar outflow between the blue-shifted and the red-shifted channel maps. Higher resolution observations are needed to obtain a better understanding of where these outflows originate from.

4.3.2 Core properties

Although it appears that none of the CO emission is associated with MM1 in G22.357+0.066 there are indications at 87.6 km s^{-1} in the ^{12}CO channel maps and at 86.4 km s^{-1} in the ^{13}CO channel maps that some of the CO emission coincides with the dust continuum. In the case of G9.62+0.19E only a few channels (-0.4 km s^{-1} to 0.3 km s^{-1}) have CO emission that can be clearly associated with the dust continuum. Whereas for G25.411+0.105 most of the CO emission is found on the dust continuum. This leads to the question of why in the cases of G9.62+0.19E and G22.357+0.066 little to no CO emission is observed on the dust continuum. One possibility is that the gas is so dense that the CO (2-1) transition might not be visible. To test this possibility the density, n_{H_2}, of the H_2 molecular gas can be estimated and compared to the critical density, n_{crit}, of the CO (2-1) transitions for all three target sources.

In order to calculate the densities for all three target sources, the area is assumed to be that of an ellipse and the volume V of the gas is given by $V = \frac{4}{3}\pi ab^2$, where a and b are the linear sizes of the major and minor axes of the source. The density calculations for all three source were done exactly the same way, thus the detailed calculations would only be described for the first source's density, n_{H_2}.

The major (4.″8) and minor (2.″5) axes of MM1 in G22.357+0.066 where converted to distances to obtain a and b, thus $a = 1.7 \times 10^{17}$ cm and $b = 9.1 \times 10^{16}$ cm. The volume, V, is then 6.0×10^{51} cm^3. Using the mass of G22.357+0.066 that was calculated in section 4.2.1.1 as 4 M$_\odot$ and the mass, m_{H_2}, of a hydrogen molecule, the number of H_2 molecules can be determined. Thus 4 M$_\odot \equiv 2.1 \times 10^{57}$ H_2. The density, n_{H_2}, is then obtained by dividing the number of H_2 molecules with the volume V, thus the density, n_{H_2}, would be 3.9×10^5 cm^{-3}.

G9.62+0.19E has a major axis of 0.″9 and a minor axis of 0.″6. Thus a and b would be 3.3×10^{16} cm and 2.3×10^{16} cm respectively. The volume, V, of G9.62+0.19E is then 7.3×10^{49} cm^3. Using the mass of G9.62+0.19E calculated in section 4.2.3.1 as 58 M$_\odot$, the density, n_{H_2}, would then be 4.7×10^8 cm^{-3}.

As for G25.411+0.105 where most of the CO emission is found on the dust continuum, the major axis is 5.″9 and a minor axis is 2.″9. Thus a and b would be 4.2×10^{17} cm and 2.0×10^{17} cm respectively. The volume, V, of G25.411+0.105 would then be 7.2×10^{52} cm^3. Using the mass of G25.411+0.105 calculated in section 4.2.2.1 as 14 M$_\odot$, the density, n_{H_2}, would be 1.1×10^5 cm^{-3}.

The critical densities, n_{crit}, of ^{12}CO (2-1), ^{13}CO (2-1), C^{18}O (2-1) and CH_3OH $v_t = 1$ ($6_{1,5}$-$7_{2,6}$) where obtained by taking their Einstein A-coefficients, A_{ij}, and dividing them with the collision coefficients, C_{ij}, between CO and H_2. The coefficients were obtained from the Leiden Atomic and Molecular data base and are presented in Table 4.2.

Comparing the density, n_{H_2}, of G22.357+0.066 with the critical densities, n_{crit}, of the CO (2-1) transitions, the gas located on the dust continuum (MM1) is denser. As for G9.62+0.19E the density of the gas, n_{H_2}, is much more dense than the critical density, n_{crit}, for the ^{12}CO (2-1) transition. This might explain why so little CO emission is observed on the dust continuum of G22.357+0.066 and G9.62+0.19E. However since the gas density of outflows are lower than the gas density towards the YSO itself (Herbst & van Dishoeck, 2009), it might explain why the CO (2-1) transitions are observed in the bipolar outflows of the sources. In the case of G9.62+0.19E the CH_3OH $v_t = 1$ ($6_{1,5}$-$7_{2,6}$) transition was observed on the dust continuum. Comparing the

TABLE 4.2: Einstein A -coefficients and the collision coefficients for all transitions.

Molecule	A_{ij} (s^{-1})	C_{ij} ($cm^3 \cdot s^{-1}$)	n_{crit} (cm^{-3})
^{12}CO (2-1)[1]	6.910×10^{-7}	6.0×10^{-11}	1.2×10^{4}
^{13}CO (2-1)[1]	6.038×10^{-7}	6.0×10^{-11}	1.0×10^{4}
C^{18}O (2-1)[1]	6.011×10^{-7}	6.0×10^{-11}	1.0×10^{4}
CH_3OH (6-7)[2]	4.368×10^{-5}	1.0×10^{-13}	4.4×10^{8}

[1] Yang et al. (2010), [2] Rabli & Flower (2010).

critical density, n_{crit}, of CH_3OH (6-7) with the gas density, n_{H_2}, the two densities are of the same order and therefore it might be why the CH_3OH $v_t = 1$ ($6_{1,5}$-$7_{2,6}$) transition is seen on the dust continuum of G9.62+0.19E. Although the gas density, n_{H_2}, of G25.411+0.105 is also denser than the critical densities, n_{crit}, of the CO(2-1) transitions, most of the CO is observed on the dust continuum. However it might also be the case that the CO emission observed on the dust continuum belongs to the bipolar outflow of G25.411+0.105 and due to the orientation of G25.411+0.105 (face-on) the CO emission is located on the dust continuum.

A mass estimate was done for each source in sections 4.2.1.1, 4.2.2.1 and 4.2.3.1 that yielded the following, G22.357+0.066 was estimated to be 4 $M_\odot$, G25.411+0.105 was 14 $M_\odot$ and G9.62+0.19E was 58 $M_\odot$. The estimated mass for G9.62+0.19E is reasonable since it is of the same order as the mass estimate of 74 $M_\odot$ that Liu et al. (2017) determined for G9.62+0.19E. However the mass estimates of G22.357+0.066 and G25.411+0.105 are small. Using data obtained from the APEX Telescope Large Area Survey of the GaLaxy (ATLASGAL) by Contreras et al. (2013), another mass estimate was done for G22.357+0.066 and for G25.411+0.105.

The observations were made at 870 microns, thus κ_ν would be 0.37 cm^2 g^{-1} (Weingartner & Draine, 2001). Contreras et al. (2013) noted a temperature of $\sim$ 22 K for G22.357+0.066 and G25.411+0.105, with their integrated flux densities as 10.14 Jy and 4.17 Jy respectively. Thus using Equation 2.93, the mass estimates were done in the same way for G22.357+0.066 and G25.411+0.105 as they were done in sections 4.2.1.1 and 4.2.2.1. The mass of G22.357+0.066 is then estimated to be $\sim$ 4000 $M_\odot$ and for G25.411+0.105 $\sim$ 6000 $M_\odot$.

The mass estimates with the ATLASGAL data are significantly larger than the mass estimates done with the SMA data for G22.357+0.066 and G25.411+0.105. The difference between these two sets of mass estimates depend on the angular sizes of the sources. For example the angular size of G22.357+0.066 with the single dish is $23'' \times 17''$ and the angular size with the interferometer is $4.''8 \times 2.''5$. Since there is an upper limit to the angular scale detectable with an interferometer, some emission form a significant part of the source might have been missed. The ATLASGAL mass estimate is the mass of the clump while the SMA mass estimate is core mass.

4.4 Molecular line emission channel maps

This section is used to present the three types of CO emission channel maps for G22.357+0.066 and G25.411+0.105 as well as the ^{12}CO and CH_3OH channel maps for G9.62+0.19E. The channel maps are discussed in the results section (section 4.2) of this chapter.

G22.357+0.066

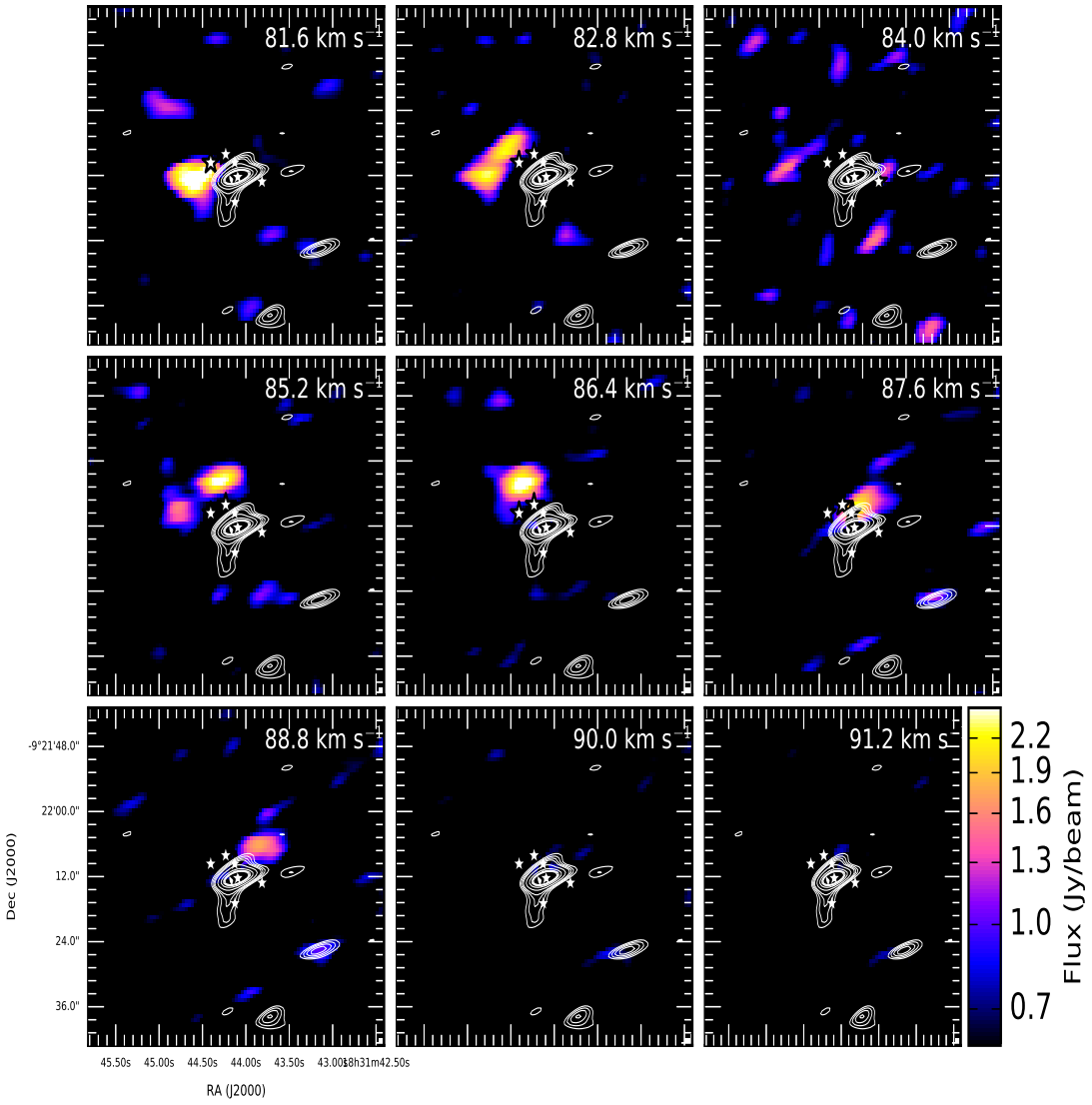

FIGURE 4.22: G22.357+0.066: ^{12}CO line emission velocity channel maps form 81.6 km·s^{-1} to 91.2 km·s^{-1}. The position of the periodic methanol maser is indicated with a circle and the white contours represent the dust continuum. The central velocity of each channel is indicated in the upper right panel. The NIR counterparts obtained from the UKIDSS database are indicated with the star symbol. The color scale for the channel maps is on the right side of the bottom channel map

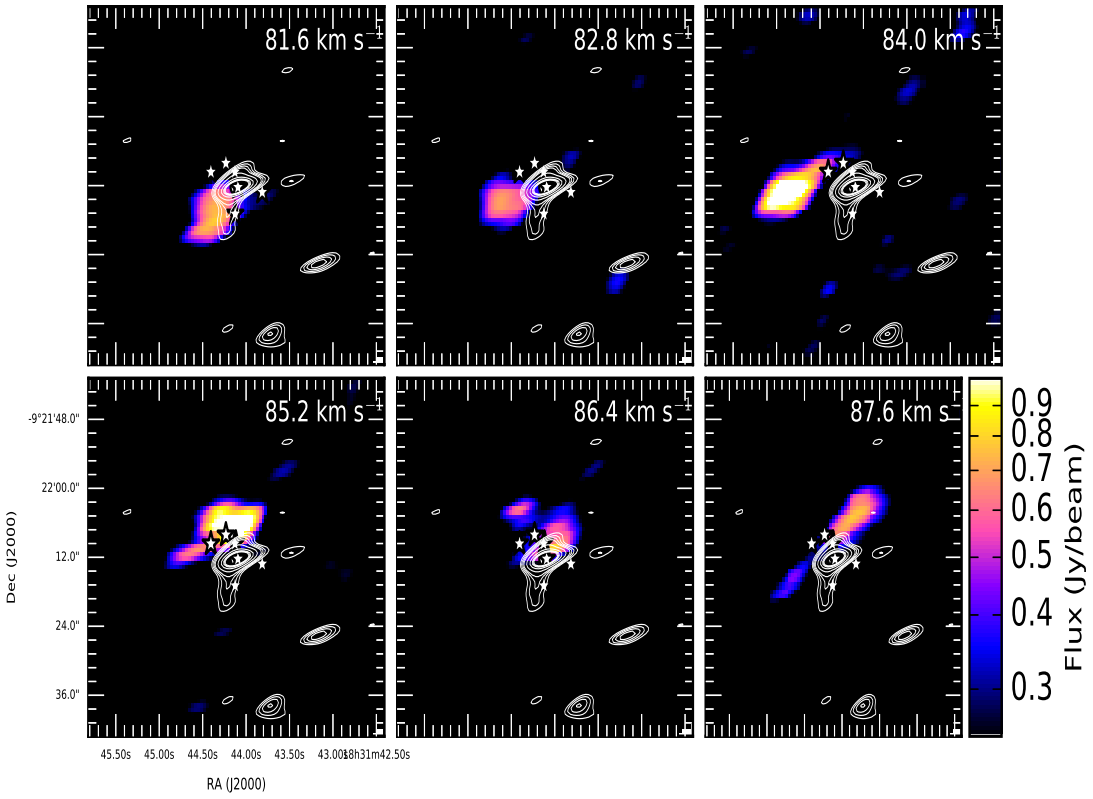

FIGURE 4.23: G22.357+0.066: ^{13}CO line emission velocity channel maps form 81.6 km·s^{-1} to 87.6 km·s^{-1}. The position of the periodic methanol maser is indicated with a circle and the white contours represent the dust continuum. The central velocity of each channel is indicated in the upper right panel. The NIR counterparts obtained from the UKIDSS database are indicated with the star symbol. The color scale for the channel maps is on the right side of the bottom channel map

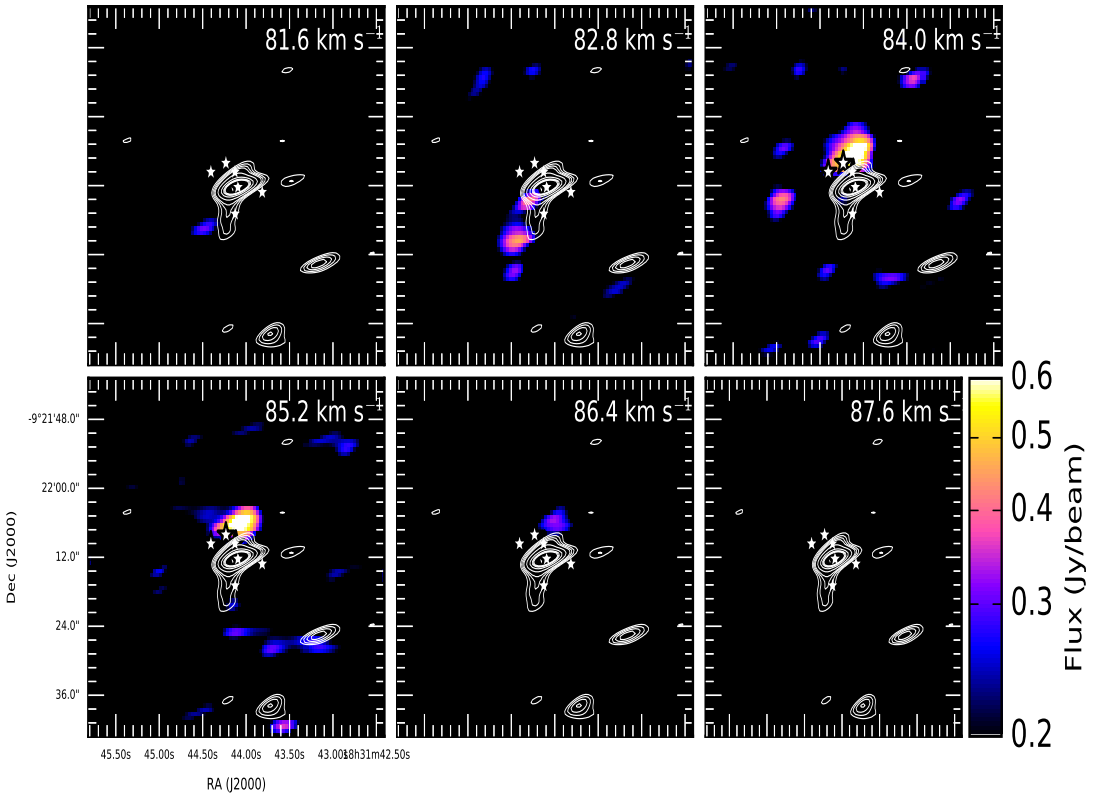

FIGURE 4.24: G22.357+0.066: $C^{18}O$ line emission velocity channel maps form 81.6 km·s^{-1} to 87.6 km·s^{-1}. The position of the periodic methanol maser is indicated with a circle and the white contours represent the dust continuum. The central velocity of each channel is indicated in the upper right panel. The NIR counterparts obtained from the UKIDSS database are indicated with the star symbol. The color scale for the channel maps is on the right side of the bottom channel map

G25.411+0.105

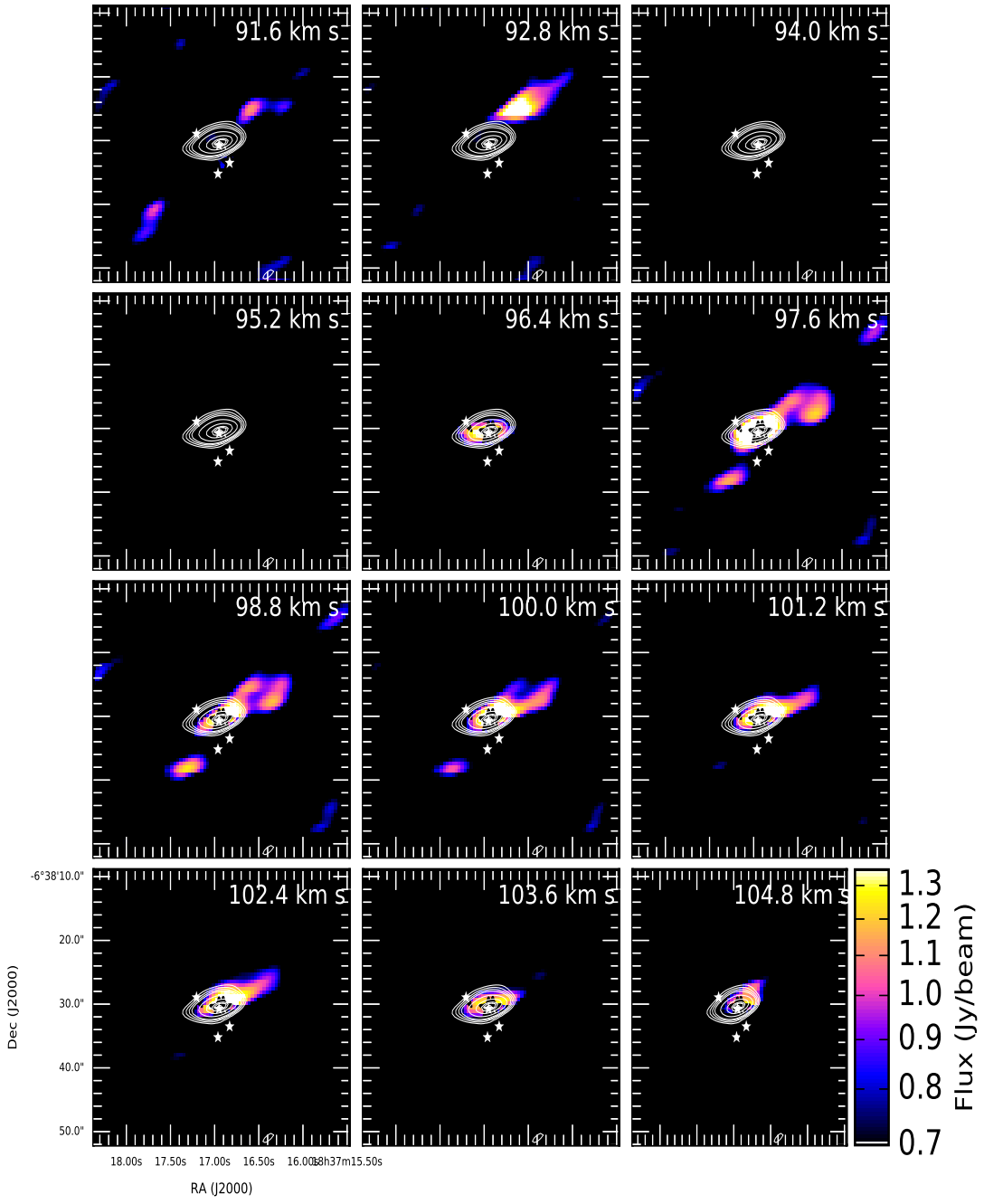

FIGURE 4.25: G25.411+0.105: ^{12}CO line emission velocity channel maps form 91.6 km·s^{-1} to 104.8 km·s^{-1}. The position of the periodic methanol maser is indicated with a circle and the white contours represent the dust continuum. The central velocity of each channel is indicated in the upper right panel. The NIR counterparts obtained from the UKIDSS database are indicated with the star symbol. The color scale for the channel maps is on the right side of the bottom channel map

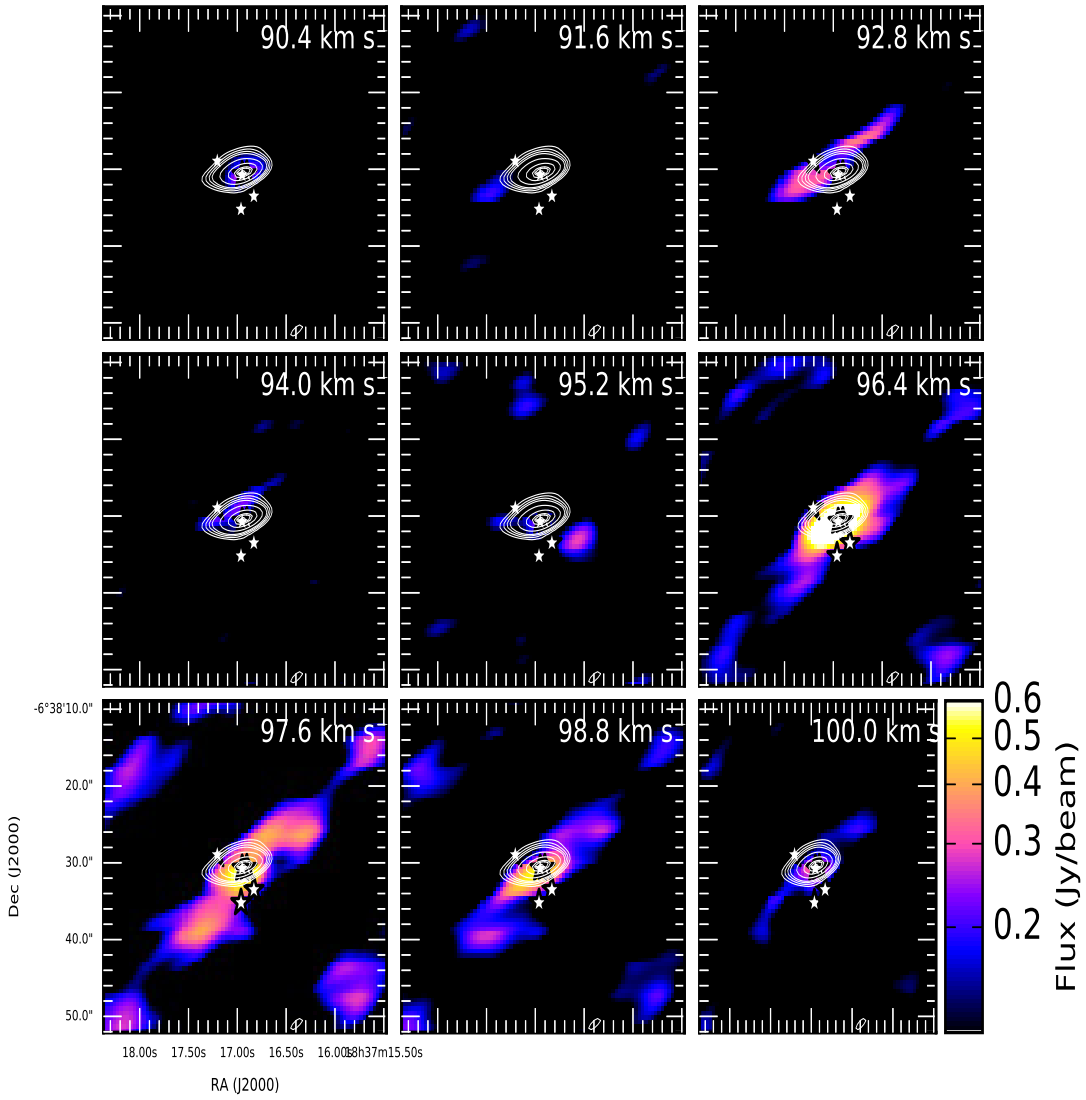

FIGURE 4.26: G25.411+0.105: ^{13}CO line emission velocity channel maps form 90.4 km·s^{-1} to 100.0 km·s^{-1}. The position of the periodic methanol maser is indicated with a circle and the white contours represent the dust continuum. The central velocity of each channel is indicated in the upper right panel. The NIR counterparts obtained from the UKIDSS database are indicated with the star symbol. The color scale for the channel maps is on the right side of the bottom channel map

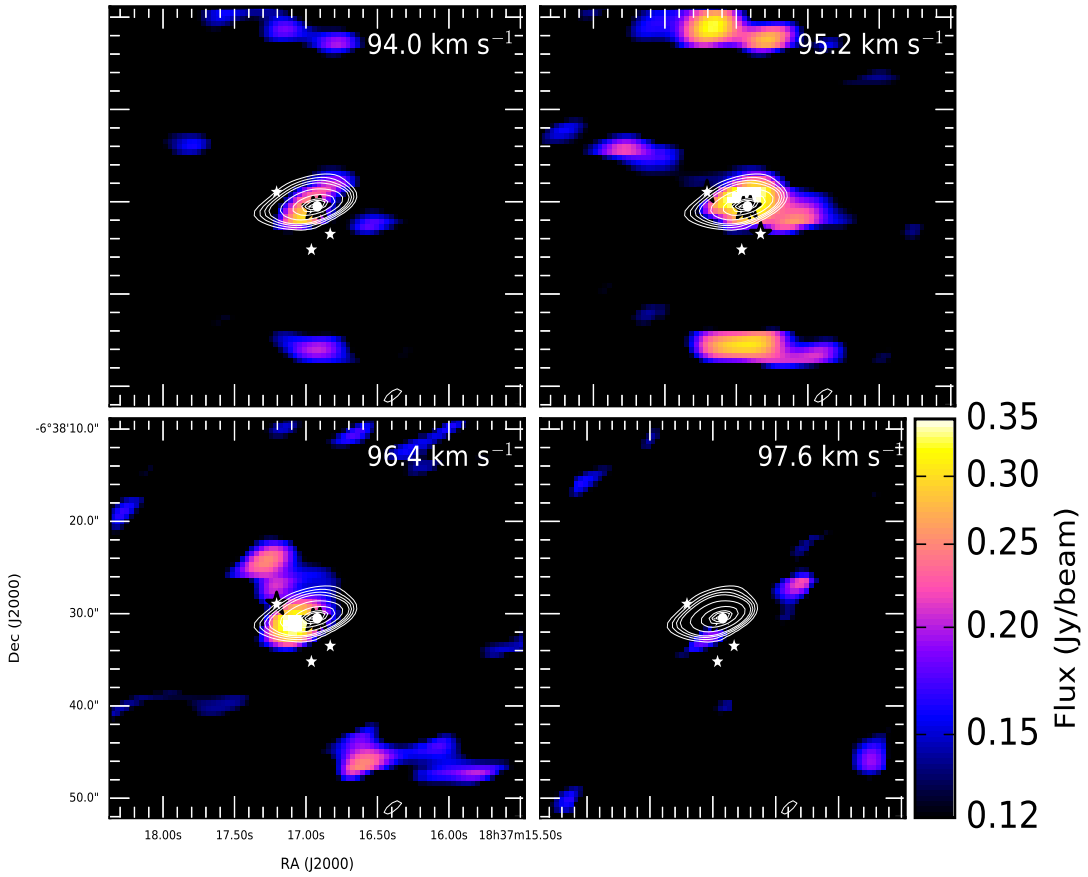

FIGURE 4.27: G25.411+0.105: $C^{18}O$ line emission velocity channel maps form 90.4 km·s^{-1} to 97.6 km·s^{-1}. The position of the periodic methanol maser is indicated with a circle and the white contours represent the dust continuum. The central velocity of each channel is indicated in the upper right panel. The NIR counterparts obtained from the UKIDSS database are indicated with the star symbol. The color scale for the channel maps is on the right side of the bottom channel map

G9.62+0.19E

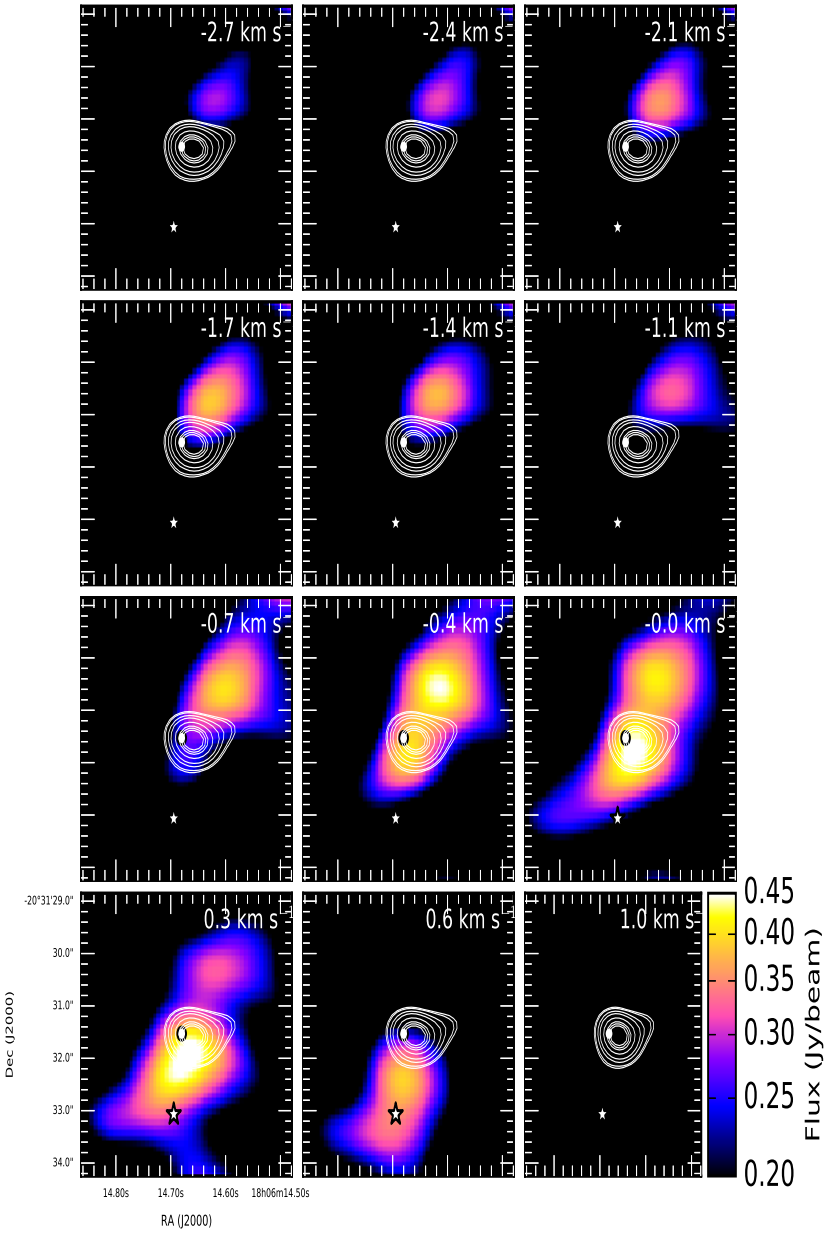

FIGURE 4.28: G9.62+0.19E: ^{12}CO blue-shifted velocity channel maps from -2.7 km s^{-1} to 1.0 km s^{-1}. The position of the periodic methanol maser is indicated with a circle and the white contours represent the dust continuum. The NIR counterpart obtained from the UKIDSS database are indicated with the star symbol. The color scale for the channel maps is on the right side of the bottom channel map

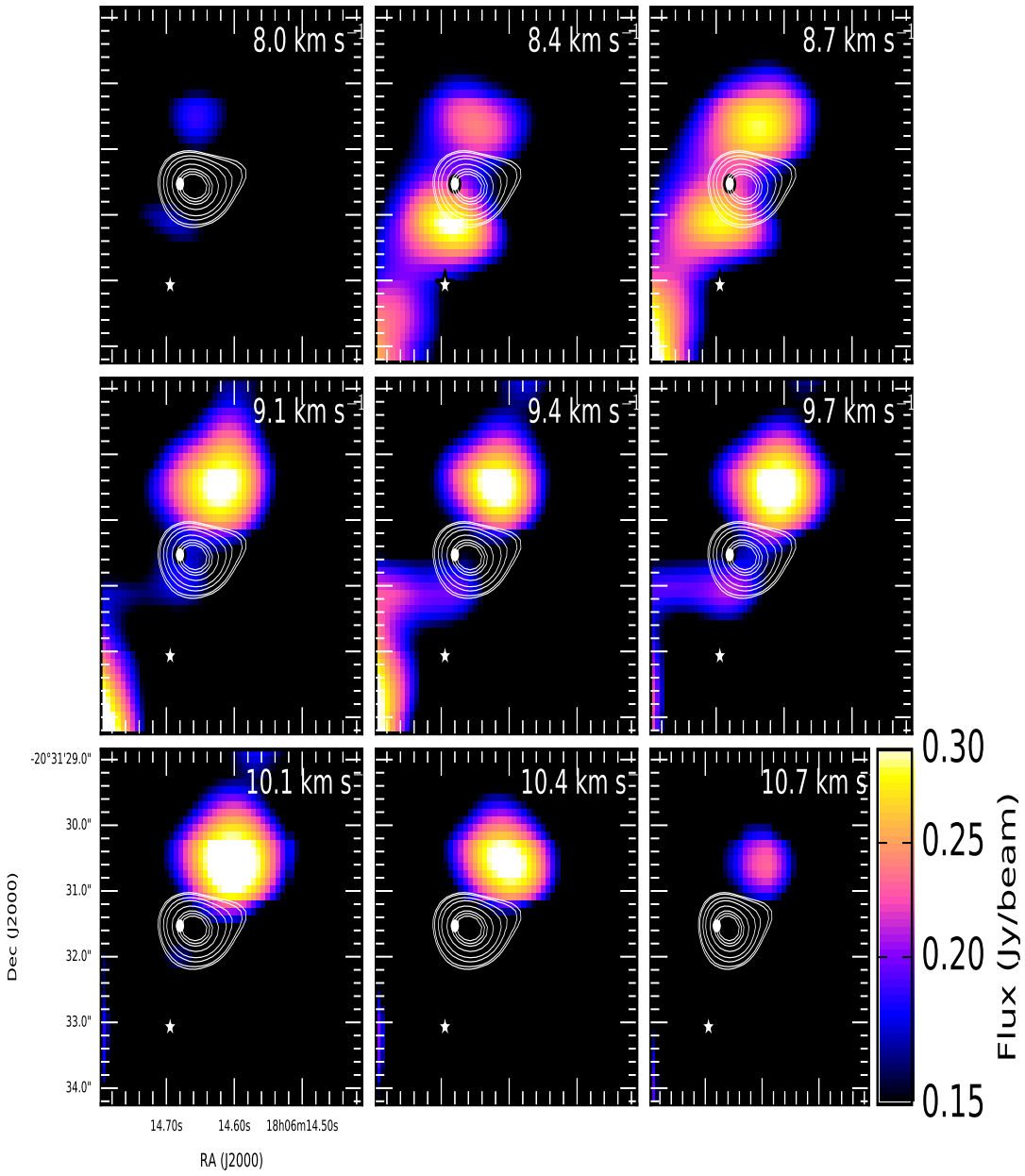

FIGURE 4.29: G9.62+0.19E: ^{12}CO red-shifted velocity channel maps from 8.0 km s^{-1} to 10.7 km s^{-1}. The position of the periodic methanol maser is indicated with a circle and the white contours represent the dust continuum. The NIR counterpart obtained from the UKIDSS database are indicated with the star symbol. The color scale for the channel maps is on the right side of the bottom channel map

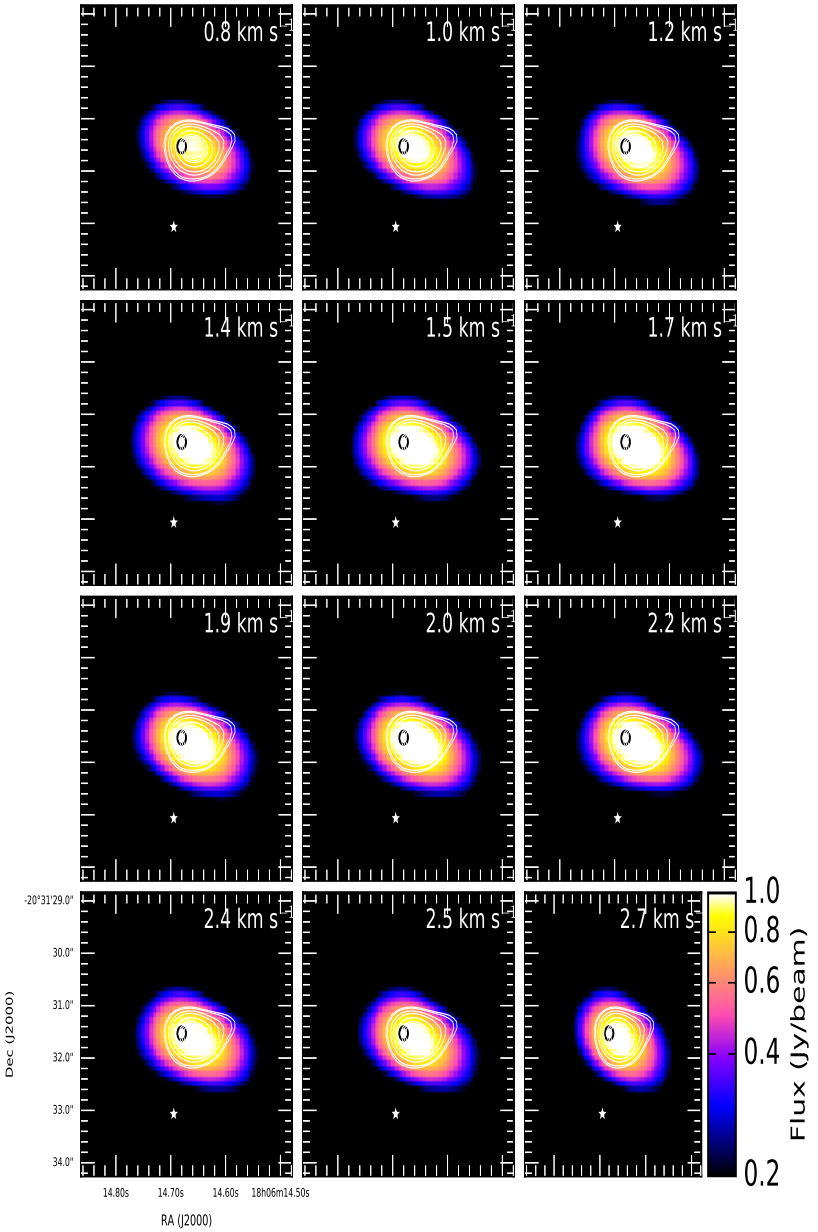

FIGURE 4.30: G9.62+0.19E: CH_3OH ν_t ($6_{1,5}$-$7_{2,6}$) velocity channel maps from 0.8 km s^{-1} to 2.7 km s^{-1}. The position of the periodic methanol maser is indicated with a circle and the white contours represent the dust continuum. The NIR counterpart obtained from the UKIDSS database are indicated with the star symbol. The color scale for the channel maps is on the right side of the bottom channel map

Chapter 5

SUMMARY AND CONCLUSION

The purpose of this study was to find any differences or similarities between high-mass star forming regions for which the periodic methanol masers have different light curves. Since it is well documented that maser light curves are studied in order to understand the driving mechanism behind the different types of light curves, this study takes a different approach, namely, using millimetre continuum and line properties of the periodic maser sources to investigate the cause of the variations in the light curve shapes.

Initially four sources were chosen from the two well defined types of lights curves. Unfortunately the data for G358.460−0.391 was not usable. Thus three sources remained, G9.62+0.19E and G22.357+0.066 which have light curves that show a sharp rise in maser flux density, followed by a slow decay and G25.411+0.105 which has a light curve that resembles an absolute cosine function (Bunny hop). A number of studies have already been done on G9.62+0.19E, but there is only a small amount of literature information on G22.357+0.066 and G25.411+0.105.

Before the data was analysed, background knowledge on interferometers was needed and quite some time was spent to correctly calibrate and image the data to insure that the results were reliable. This chapter contains a brief summary on the work that has been done in this study, followed by concluding remarks and recommendations for future work.

5.1 Summary

The sources G22.357+0.066 and G25.411+0.105 were observed with the SMA in a compact configurations. The dust continuum and the spectra lines ^{12}CO (2-1), ^{13}CO (2-1) and C^{18}O (2-1), with a channel spacing of 1.1 km s $^{-1}$, were covered. The full data calibration and imaging were done in CASA. For the source G9.62+0.19E ALMA archival data was used and the overview on the data was taken form Liu et al. (2017). The molecular lines that were of interest to this study were ^{12}CO (2-1) and CH_3OH ν_t ($6_{1,5}$-$7_{2,6}$). The data also included the dust continuum of G9.62+0.19E.

5.1.1 Dust continuum

The dust continuum of G22.357+0.066 showed six continuum cores, however the one of interest to this study was MM1. For G25.411+0.105 and G9.62+0.19E only one dust continuum core for each source was observed. The masses of G22.357+0.066, G25.411+0.105 and G9.62+0.19E were estimated to be 4 $M_{\odot}$, 14 $M_{\odot}$ and 58 $M_{\odot}$, respectively.

5.1.2 CO emission of G22.357+0.066

- The CO emission of the channel maps showed a clockwise shift in the emission around the dust continuum.
- In the integrated intensity maps most of the CO emission does not seem to be associated with the dust continuum.
- The CO emission showed a south-east - north-west symmetry with regard to the dust continuum.
- Evidence of bipolar outflow was found in the channel maps.

5.1.3 CO emission of G25.411+0.105

- Almost all the CO emission, in the channel maps and the integrated intensity maps, are projected on the dust continuum.
- At 94.0 km s $^{-1}$ and 95.2 km s $^{-1}$ no ^{12}CO emission was observed and also very little emission at these velocities were seen in the ^{13}CO.
- The ^{12}CO integrated intensity map has two cores, one located on the dust continuum and the other north-west of the dust continuum.
- The C^{18}O integrated intensity map also has two smaller cores, south on the dust continuum and west of the dust continuum.
- The ^{13}CO line spectrum showed wing channels that points to the presence of a bipolar outflow.
- The ^{12}CO line spectrum showed a double peak profile. Thus the ^{12}CO line spectrum could be showing a P Cygni profile or the emission could be originating from two cores.

5.1.4 Molecular line emission of G9.62+0.19E

- Most of the CO emission in the channel maps and integrated intensity map are found either north-west of the dust continuum or south-east, very little emission is seen on the continuum.
- The ^{12}CO channel maps show evidence of multiple outflows.
- The ^{12}CO line spectrum, shows a very complex P Cygni profile.
- A north-west - south-east symmetry with regard to the dust continuum is seen in the CO emission.

- The detection of the CH_3OH ν_t ($6_{1,5}$-$7_{2,6}$) line, indicates that G9.62+0.19E could be a hot core.
- The CH_3OH ν_t ($6_{1,5}$-$7_{2,6}$) channel maps and integrated intensity map show compact emission located on the dust continuum.
- The CH_3OH ν_t ($6_{1,5}$-$7_{2,6}$) showed evidence of rotational motion.

5.2 Conclusion

The data obtained for this study contains a substantial amount of information and there are quite a few things, for example the column densities and outflow mass, that were not done or discussed in this study. The reason for this was that doing all the above mentioned requires a large amount of time. Since most of the time in this study was spent on obtaining experience in CASA and how to calibrate and image the SMA data, it was decided to stay with the scope of the study, which was to search for similarities and differences in these regions.

Analysis of the SMA data of G22.357+0.066 and G25.411+0.105 as well as of the ALMA data on G9.62+0.19E suggest clear geometric difference. For G22.357+0.066 and G25.411+0.105 it was possible to extract blue-shifted and red-shifted outflows. This was possible because the SMA data does not have the angular resolution or sensitivity that the ALMA data has for G9.62+0.19E, which made separation between the blue-shifted and red-shifted outflows difficult and thus it was not done. In the cases of G9.62+0.19E and G22.357+0.066, which have the same type of light curve, bipolar outflows almost in the plane of the sky were identified. For G25.411+0.105, which has a different type of light curve than G9.62+0.19E and G22.357+0.066, a bipolar outflow almost perpendicular to the plane of the sky was identified. G22.357+0.066 and G9.62+0.19E showed very little CO emission on the dust continuum, most of the CO emission was associated with the outflows. Whereas for G25.411+0.105 most of the CO emission was located on the dust continuum. Density calculations suggest that the gas around the YSOs might be too dense to observe the CO(2-1) transition. Thus it could be that the CO emission observed on the dust continuum of G25.411+0.105 is also associated with the outflows rather than the YSO itself and that, due to the orientation of G25.411+0.105, the CO emission is only projected onto the dust continuum.

The presence of outflows also imply the existence of disks. This would mean that G22.357+0.066 and G9.62+0.19E, with similar types of periodic methanol maser light curves and similar orientations, would have disks that are viewed edge-on. G25.411+0.105 on the other hand has a different type of periodic methanol maser light curve and a different orientation than G22.357+0.066 and G9.62+0.19E, then the disk of G25.411+0.105 would be viewed face-on. Thus it could be that the difference in the shape of the periodic methanol maser light curve is a viewing angle effect. In order to confirm this observation of a larger number of sources, of both types of light curves, would be needed.

5.3 Recommendations for future work

For future work on this data, the physical properties of the outflows, such as mass estimates, orientation impact and determining the column densities, can be done. The ^{12}CO line spectrum of G25.411+0.105, the complex P Cygni profile in the ^{12}CO of G9.62+0.19E and the multiple outflows observed in the ^{12}CO channel maps of G9.62+0.19E, were not discussed. These should be investigated in more detail in future work.

Bibliography

Araya, E. D., Hofner, P., Goss, W. M., et al. 2010, ApJ, 717, L133

Arce, H. G., Shepherd, D., Gueth, F., et al. 2007, Protostars and Planets V, 245

Bachiller, R. 1996a, ARA&A, 34, 111

Bachiller, R. 1996b, in Molecules in Astrophysics: Probes & Processes

Ball, J. A., Gottlieb, C. A., Lilley, A. E., & Radford, H. E. 1970, ApJ, 162, L203

Bally, J. 1986, Science, 232, 185

Bartkiewicz, A., Szymczak, M., Pihlström, Y. M., et al. 2011, A&A, 525, A120

Bartkiewicz, A., Szymczak, M., van Langevelde, H. J., Richards, A. M. S., & Pihlström, Y. M. 2009, A&A, 502, 155

Bergin, E. A., Goldsmith, P. F., Snell, R. L., & Langer, W. D. 1997, ApJ, 482, 285

Beuther, H. 2007, in IAU Symposium, Vol. 237, Triggered Star Formation in a Turbulent ISM, ed. B. G. Elmegreen & J. Palous, 148–154

Blitz, L. 1990, in Astronomical Society of the Pacific Conference Series, Vol. 12, The Evolution of the Interstellar Medium, ed. L. Blitz, 273–289

Blitz, L. 1993, in Protostars and Planets III, ed. E. H. Levy & J. I. Lunine, 125–161

Blitz, L. & Williams, J. P. 1999, ArXiv 9903382

Bonnell, I. A., Bate, M. R., Clarke, C. J., & Pringle, J. E. 2001, MNRAS, 323, 785

Breen, S. L., Fuller, G. A., Caswell, J. L., et al. 2015, MNRAS, 450, 4109

Carroll, B. & Ostlie, D. 2017, An Introduction to Modern Astrophysics (Cambridge University Press)

Caswell, J. L., Vaile, R. A., & Forster, J. R. 1995, MNRAS, 277, 210

Cesaroni, R., Galli, D., Lodato, G., Walmsley, C. M., & Zhang, Q. 2007, Protostars and Planets V, 197

Chabrier, G. 2003, PASP, 115, 763

Churchwell, E. 2002a, in Astronomical Society of the Pacific Conference Series, Vol. 267, Hot Star Workshop III: The Earliest Phases of Massive Star Birth, ed. P. Crowther, 3

Churchwell, E. 2002b, ARA&A, 40, 27

Contreras, Y., Schuller, F., Urquhart, J. S., et al. 2013, A&A, 549, A45

Elitzur, M., ed. 1992, Astrophysics and Space Science Library, Vol. 170, Astronomical masers

Ellingsen, S. P. 2006, ApJ, 638, 241

Elmegreen, B. G. 1990, in Astronomical Society of the Pacific Conference Series, Vol. 12, The Evolution of the Interstellar Medium, ed. L. Blitz, 247–271

Emerson, D. 1996, Interpreting Astronomical Spectra (Wiley)

Evans, II, N. J. 1999, ARA&A, 37, 311

Garay, G., Rodriguez, L. F., Moran, J. M., & Churchwell, E. 1993, ApJ, 418, 368

Goedhart, S., Gaylard, M. J., & van der Walt, D. J. 2003, MNRAS, 339, L33

Goedhart, S., Gaylard, M. J., & van der Walt, D. J. 2004, MNRAS, 355, 553

Goedhart, S., Langa, M. C., Gaylard, M. J., & Van Der Walt, D. J. 2009, MNRAS, 398, 995

Goedhart, S., Maswanganye, J. P., Gaylard, M. J., & van der Walt, D. J. 2014, MNRAS, 437, 1808

Green, J. A., Caswell, J. L., Fuller, G. A., et al. 2009, MNRAS, 392, 783

Herbst, E. & van Dishoeck, E. F. 2009, ARA&A, 47, 427

Herzberg, G. 1950, Molecular spectra and molecular structure. Vol.1: Spectra of diatomic molecules

Hildebrand, R. H. 1983, QJRAS, 24, 267

Hirota, T., Machida, M. N., Matsushita, Y., et al. 2017, Nature Astronomy, 1, 0146

Hofner, P., Kurtz, S., Churchwell, E., Walmsley, C. M., & Cesaroni, R. 1996, ApJ, 460, 359

Houde, M., Hull, C. L. H., Plambeck, R. L., Vaillancourt, J. E., & Hildebrand, R. H. 2016, ApJ, 820, 38

Humphreys, E. 2011, ArXiv 1104.2306

Ilee, J. D., Cyganowski, C. J., Brogan, C. L., et al. 2018, ApJ, 869, L24

Inayoshi, K., Sugiyama, K., Hosokawa, T., Motogi, K., & Tanaka, K. E. I. 2013, ApJ, 769, L20

Kroupa, P. 2002, Science, 295, 82

Kruegel, E. 2003, The physics of interstellar dust

Kurtz, S. 2002, in Astronomical Society of the Pacific Conference Series, Vol. 267, Hot Star Workshop III: The Earliest Phases of Massive Star Birth, ed. P. Crowther, 81

Kwok, S. 2007, Physics and Chemistry of the Interstellar Medium (University Science Books)

Lada, C. J. 2005, Progress of Theoretical Physics Supplement, 158, 1

Larson, R. B. 1994, in Lecture Notes in Physics, Berlin Springer Verlag, Vol. 439, The Structure and Content of Molecular Clouds, ed. T. L. Wilson & K. J. Johnston, 13

Larson, R. B. 2003, Reports on Progress in Physics, 66, 1651

Liu, T., Lacy, J., Li, P. S., et al. 2017, ArXiv 1705.04907

Liu, T., Wu, Y., Liu, S.-Y., et al. 2011, ApJ, 730, 102

Mahmoud, K. A. E. 2006, PhD thesis, University of Manchester

Maswanganye, J. P., Gaylard, M. J., Goedhart, S., Walt, D. J. v. d., & Booth, R. S. 2015, MNRAS, 446, 2730

McKee, C. F. & Ostriker, E. C. 2007, ARA&A, 45, 565

Menten, K. M. 1991, ApJ, 380, L75

Mihalas, D. & Binney, J. 1981, Galactic astronomy: Structure and kinematics /2nd edition/

Motte, F., Bontemps, S., & Louvet, F. 2017, ArXiv e-prints

Parfenov, S. Y. & Sobolev, A. M. 2014, MNRAS, 444, 620

Rabli, D. & Flower, D. R. 2010, MNRAS, 406, 95

Reid, M. J., Menten, K. M., Zheng, X. W., et al. 2009, ApJ, 700, 137

Robinson, K. 2007, Spectroscopy: The Key to the Stars

Rybicki, G. B. & Lightman, A. P. 1986, Radiative Processes in Astrophysics, 400

Salpeter, E. E. 1955, ApJ, 121, 161

Sanna, A., Menten, K. M., Carrasco-González, C., et al. 2015, ApJ, 804, L2

Sanna, A., Reid, M. J., Moscadelli, L., et al. 2009, ApJ, 706, 464

Shepherd, D. S. & Churchwell, E. 1996, ApJ, 472, 225

Shepherd, D. S., Yu, K. C., Bally, J., & Testi, L. 2000, ApJ, 535, 833

Stahler, S. W. & Palla, F. 2005, The Formation of Stars, 865

Szymczak, M., Bartkiewicz, A., & Richards, A. M. S. 2007, A&A, 468, 617

Szymczak, M., Wolak, P., & Bartkiewicz, A. 2015, MNRAS, 448, 2284

Szymczak, M., Wolak, P., Bartkiewicz, A., & van Langevelde, H. J. 2011, A&A, 531, L3

Tayler, R. J. 1994, The Stars, Their Structure and Evolution

Testi, L., Hofner, P., Kurtz, S., & Rupen, M. 2000, A&A, 359, L5

Thompson, A. R., Moran, J. M., & Swenson, Jr., G. W. 2017, Interferometry and Synthesis in Radio Astronomy, 3rd Edition

UKIDSS Consortium. 2012, VizieR Online Data Catalog, 2316

van der Walt, D. J. 2011, AJ, 141, 152

van der Walt, D. J., Goedhart, S., & Gaylard, M. J. 2009, MNRAS, 398, 961

van der Walt, D. J., Maswanganye, J. P., Etoka, S., Goedhart, S., & van den Heever, S. P. 2016, A&A, 588, A47

Ward-Thompson, D. & Whitworth, A. P. 2011, An Introduction to Star Formation

Weingartner, J. C. & Draine, B. T. 2001, ApJ, 548, 296

Williams, J. P., Blitz, L., & McKee, C. F. 2000, Protostars and Planets IV, 97

Wilson, T. L., Rohlfs, K., & Hüttemeister, S. 2013, Tools of Radio Astronomy

Yang, B., Stancil, P. C., Balakrishnan, N., & Forrey, R. C. 2010, ApJ, 718, 1062

Yen, H.-W., Koch, P. M., Takakuwa, S., et al. 2017, ApJ, 834, 178

Yorke, H. W. & Sonnhalter, C. 2002, ApJ, 569, 846

Zhang, Q., Hunter, T. R., Brand, J., et al. 2001, ApJ, 552, L167

Zinnecker, H. & Yorke, H. W. 2007, ARA&A, 45, 481

Appendix A

Derivations and Calculations

A.1 Derivation for the Virial theorem (Tayler, 1994)

Tayler (1994) uses the equation of Hydrostatic support as an initial condition to derive the Virial theorem:

$$\frac{dP_r}{dr} = -\frac{GM_r\rho_r}{r^2} \tag{A.1}$$

where P_r is the pressure, M_r the mass and ρ_r the density, all are functions of the radius r of a spherical molecular cloud.

Tayler (1994) also gives an expression for the change in mass M with radius r in a spherical molecular cloud:

$$\frac{dM}{dr} = 4\pi r^2\rho \tag{A.2}$$

Combining the above expressions, A.1 and A.2, the following is obtained:

$$4\pi r^3 dP = -4\pi r M\rho = -\frac{GM}{r} \tag{A.3}$$

Integrating equation A.3 from the center to the surface of the spherical molecular cloud of volume $V = \frac{3}{4}\pi r^3$:

$$3\int_{P_c}^{P_s} V dP = -G\int_{M_s}^{0} \frac{M}{r} dM \tag{A.4}$$

The left hand side of A.4 gives:

$$3\int_{P_c}^{P_s} V dP = 3[PV]_c^s - 3\int_0^{V_s} P dV \tag{A.5}$$

$V_c = 0$ at the lower limit of integration, thus the integrated part vanishes.

The right hand side of A.4 is the negative gravitational potential energy W of the molecular cloud. Using the relation $dM = \rho dV$ A.4 can be rewritten as:

$$4\pi r_s^3 P_s = 3\int \frac{P}{\rho} dM + W \tag{A.6}$$

The surface pressure of the spherical molecular cloud would be zero if it is surrounded by a vacuum and the left hand side of A.6 would be zero:

$$3\int \frac{P}{\rho} dM + W = 0 \tag{A.7}$$

which is a simplified version of the ***Virial theorem***.

A.2 Derivation for gravitational potential energy W (Carroll & Ostlie, 2017)

Assuming a spherical GMC with a constant density the gravitational potential can be derived as follow (Carroll & Ostlie, 2017):

For a system of two particles the gravitational potential energy W is given by:

$$W = G\frac{Mm}{r} \tag{A.8}$$

The masses of the two particles, separated by a distance r, is give by M and m respectively.

For a system of particle the gravitational force on a point of mass dM, located outside a spherical symmetric mass M_r is given by:

$$F_{g,i} = G\frac{M_r dM}{r^2} \tag{A.9}$$

directed toward the center of the sphere.

The gravitational potential energy is therefore given by:

$$W_{g,i} = -G\frac{M_r dM}{r} \tag{A.10}$$

The point masses are uniformly distributed inside a shell with thickness dr. The volume of the shell is $V = 4\pi r^2 dr$, therefore:

$$dM = 4\pi r^2 \rho dr \tag{A.11}$$

where ρ is the mass density.

Thus equation A.10 can be rewritten as:

$$dW_g = -G\frac{4\pi M_r r^2 \rho}{r} dr \tag{A.12}$$

$$\Rightarrow dW_g = -4\pi G M_r r \rho dr \tag{A.13}$$

The total gravitational potential energy is given by integrating over the entire spherical mass with radius R:

$$W_g = -4\pi G \int_0^R M_r r \rho dr \tag{A.14}$$

The spherical symmetric mass M_r is given by:

$$M_r = \frac{4}{3}\pi r^3 \rho \tag{A.15}$$

where $\frac{4}{3}\pi r^3$ is the volume of the sphere.

Thus

$$W_g = -\frac{(4\pi)^2 G}{3}\int_0^R r^4 \rho^2 dr \tag{A.16}$$

$$\Rightarrow W_g = -\frac{(4\pi)^2 G}{3\cdot 5}\rho^2 R^5 \tag{A.17}$$

Assume the density is constant and equal to it's average value:

$$\rho \sim \frac{3M_r}{4\pi R^3} \tag{A.18}$$

then equation A.17 becomes:

$$W_g \sim -\frac{(4\pi)^2 G}{3\cdot 5}[\frac{3M_r}{4\pi R^3}]^2 R^5 \tag{A.19}$$

$$\Rightarrow W_g \sim \frac{3GM_r^2}{5R} \tag{A.20}$$

which is the ***gravitational potential energy*** in GMC (Carroll & Ostlie, 2017).

A.3 Derivation for the free-fall timescale (Carroll & Ostlie, 2017)

Consider a spherical molecular cloud with a radius r and a mass M_r. The local acceleration of gravity is given by:

$$m_i \mathbf{a} = \Sigma F = \frac{GMM_i}{r^2} \tag{A.21}$$

$$\mathbf{a} = \frac{d^2 r}{dt^2} = \frac{dv}{dr}\frac{dr}{dt} = v\frac{dv}{dr} = -\frac{GM_r}{r^2} \tag{A.22}$$

The behaviour of the surface of the spherical cloud can be described by integrating equation A.22:

$$\int v\, dv = -G\int_R^r \frac{M_r}{r^2}\, dr \tag{A.23}$$

$$\Rightarrow \frac{v^2}{2} = \frac{GM_r}{r}\Big|_R^r + C \tag{A.24}$$

The integration constant can be evaluated by requiring that the infall velocity v is zero at the beginning of the cloud collapse (Carroll & Ostlie, 2017) ($v = 0$ when $r = R$), thus:

$$C = -\frac{GM_r}{r} \tag{A.25}$$

Solving equation A.24 for the velocity at the surface, gives:

$$\frac{v^2}{2} = GM_r\left[\frac{1}{r} - \frac{1}{R}\right]^{\frac{1}{2}} \tag{A.26}$$

$$\Rightarrow v = \sqrt{\frac{2GM_r}{R}} \left[\frac{R}{r} - 1\right]^{\frac{1}{2}} \tag{A.27}$$

To obtain an expression for the position of the spherical molecular cloud surface as function of time, the following substitutions are done:

Let $r = Rsin\theta$ with the boundary conditions $\theta = 0 \Rightarrow r = 0$ and $\theta = \frac{\pi}{2} \Rightarrow r = R$, thus

$$\frac{dr}{dt} = \frac{d}{dt}\Big[Rsin\theta\Big] = 2Rsin\theta cos\theta \; d\theta \tag{A.28}$$

Substituting the above expression into equation A.27, gives:

$$2R\theta cos\theta \; d\theta = \sqrt{\frac{2GM_r}{R}} \left[\frac{1 - sin^2\theta}{sin^2\theta}\right]^{\frac{1}{2}} dt \tag{A.29}$$

$$\Rightarrow sin^2\theta \; d\theta = \sqrt{\frac{GM_r}{2R^3}} \; dt \tag{A.30}$$

Using the identity $sin^2\theta = \frac{1}{2}[1 - cos2\theta]$ and integrating with respect to time using the free-fall timescale definition as boundary conditions. The free-fall timescale can be defined as the time taken by a cloud in free-fall to collapse from $r = R$ at $t = 0$ to $r = 0$ at $t = t_{ff}$ (Carroll & Ostlie, 2017). Equation A.30 can be rewritten as:

$$\frac{1}{2}\int_0^{\frac{\pi}{2}} [1 - cos2\theta] \; d\theta = \int_0^{t_{ff}} \sqrt{\frac{GM_r}{2R^3}} \; dt \tag{A.31}$$

$$\Rightarrow \frac{\pi}{4} = \sqrt{\frac{GM_r}{2R^3}} \; t_{ff} \tag{A.32}$$

$$t_{ff} = \sqrt{\frac{\pi R^3}{8GM_r}} \tag{A.33}$$

where t_{ff} is the ***free-fall timescale***.

The density of the cloud is defined by $\rho = \frac{3M_r}{4\pi R^3}$. The free-fall timescale can be rewritten in terms of the density:

$$t_{ff} = \sqrt{\frac{3\pi}{32G\rho}} \tag{A.34}$$